Magnetic And Transport Properties In Correlated Topological Materials: A First-Principles Study

A Thesis submitted for the degree of

Doctor of Philosophy (Science)

in

Physics (Theoretical)

by

JYOTIRMOY SAU

Department of Physics

University of Calcutta

2024

Dedicated to my Parents ...

Acknowledgements

I want to start by expressing my gratitude to Professor Manoranjan Kumar, my adviser, for his outstanding support of my study during the last five years. I particularly enjoyed the stimulating discussions on research that Manoranjan and I had virtually every day in the lab. His profound knowledge and genuine approach to physics made the conversations fun and something I won't soon forget. The chats are always entertaining because of his boundless energy and abundance of ideas. Manoranjan was also very helpful to me in honing my skills in summarizing physics and in writing and presenting scientific findings. He always gets right to the point, and our intellectual interchange has helped me grasp physics much better by pointing out areas for improvement and filling in gaps. I've been able to explore a lot of initiatives and implement my ideas because of Manoranjan's generosity and openness. My ability to generate original ideas and become an independent researcher has greatly benefited from these experiences. Throughout the five years I spent pursuing my PhD, he taught me a lot, and I am particularly appreciative of how he helped me progress from not knowing much about physics when I first started the lab to being able to conduct research on my own. He is consistently kind, vivacious, impartial, and supportive. I am really grateful to have had such a wonderful PhD adviser.

The conversations I had at the S.N. Bose National Centre for Basic Sciences (SNBNCBS) with graduate students, postdoctoral fellows, and guests also taught me a lot. In these five years, I feel fortunate to have made a lot of new friends as well. My life would be far less enjoyable without the folks I spend time with on the weekends, so I would want to thank them all.

Lastly, I want to express my gratitude to my parents for their unwavering support during my graduate studies.

I am grateful for financing assistance from the University Grants Commission.

List of publications

Included in the thesis

1. Topological properties and anomalous transport in van der Waals ferromagnets Fe_nGeTe_2: a comparative study.
   J.Sau, S. R. Hassan, N. Kumar and M. Kumar, Phys. Scr. 98 125916 (2023)

2. Hydrostatic Pressure-Induced Anomalous Hall Effect in Co_2FeSi Semimetal.
   J. Sau, D. Sa, and M. Kumar, Electron. Struct. 6 015008 (2024)

3. Anomalous Hall effect in topological Weyl and nodal-line semimetal Heusler compound Co_2VAl.
   S. Chatterjee, J. Sau*, S. Ghosh, S. Samanta, B. Ghosh, M. Kumar and K. Mandal, J. Phys.: Condens. Matter,35035601 (2023). (*The first two authors made equal contributions.)

4. Nodal-line and triple point fermion induced anomalous Hall effect in the topological Heusler compound Co_2CrGa.
   S. Chatterjee, J. Sau*, S. Samanta, B. Ghosh, N. Kumar, M. Kumar, and K. Mandal, Phys. Rev. B 107, 125138 (2023) (*The first two authors made equal contributions.)

5. Flat band separation with robust spin Hall Effect with nontrivial band topology in bilayer kagome metals.
   J. Sau, H. Banerjee, S.Saha, N. Kumar and M. Kumar

6. Emergence of anomalous transverse conductivity in ferromagnetic topological double perovskite Ba_2CoWO_6 due to intrinsic spin-orbit coupling within the multi-orbital Hubbard model and ab initio method
   J.Sau, S.Chakraborty, S.saha, A. Mukherjee, K. Pradhan and M. Kumar

Other works

1. Spin-gapless semiconducting characteristics and related band topology of quaternary Heusler alloy CoFeMnSn.
   S. Gupta, J. Sau*, M. Kumar and C. Mazumdar, J. Mater. Chem. C,12, 706-716 (2024) (*The first two authors made equal contributions.)

2. Anomalous Hall effect from gapped nodal line in the Co_2FeGe Heusler compound.
   G. K. Shukla, J. Sau*, N. Shahi, A. K. Singh, M. Kumar, and S. Singh, Phys. Rev. B 104,195108 (2021). (*First author from the theory group.)

3. Band splitting induced Berry flux and intrinsic anomalous Hall conductivity in the NiCoMnGa quaternary Heusler compound.
   G. K. Shukla, J. Sau*, V. Kumar, M. Kumar, and S. Singh, Phys. Rev. B 106, 045131 (2022). (*First author from the theory group.)

4. Phonons and Thermal Properties of Ge Nanowires: A Raman Spectroscopy Investigation and Phonon Simulations.
   V. Agarwal, S. Sett, J. Sau*, A. Ghatak, M. Kumar, A. Singha, and A. K. Raychaudhuri, J. Phys. Chem. C 126, 35, 15046–15056 (2022) (*First author from the theory group)

5. Tuning the Anomalous Hall effect from large to zero in the two ferromagnetic states of the layered compound $SmMn_2Ge_2$.
   M. Singh, J. Sau*, A. Panda, B. Rai, M. Kumar, and N. Kumar (*First author from the theory group)(under review)

6. Incipient charge density wave transitions in 1T-VS_2 microflakes.
   S. Pal, P. Majhi, J. Sau*, S. Masanta, P. Pal, M. Kumar, A. Singha, P.D. Babu, B. Ghosh, and A. K. Raychaudhuri (*First author from the theory group) (under review)

7. Pressure induced superconducting state in ideal topological insulator $BiSbTe_3$
   V. Gangwar, S. Kumar, M. Singh, L. Ghosh, J. Sau*, M. Kumar and S. Chatterjee, Phys. Scr. 96 055802 (2021) (*First author from the theory group)

8. Superconductivity in single crystals of a quasi-one dimensional infinite chain cuprate $Sr_xCa_{1-x}CuO_{2+\delta}$ at 82 K and above.

   G. Vaid, N. K. Rajak, D. Tirumalarao, J. Sau*, S. K C, S. Athira,1 G. Prakash, A. Babu, T. Gaikwad, S. Chandradas, A. P. Andrews, A. A., B. Varghese, M. Kumar, M. R. Varma, K. P. Surendran, A. Thamizhavel, S. Ramakrishnan, and D. Jaiswal-Nagar. (*First author from the theory group) (under review)

Contents

List of Figures

List of Tables

Chapter 1

Introduction

> All matter originates and exists only by virtue of a force which brings the particle of an atom to vibration and holds this most minute solar system of the atom together. We must assume behind this force the existence of a conscious and intelligent mind. This mind is the matrix of all matter.— **Max Planck**

One of the main goals of condensed matter physics is to identify phases of matter. Some phases, including magnets and superconductors, are understood through spontaneous breaking of the symmetries. Certain phases of matter cannot be explained in terms of broken symmetry, evidenced in the pattern of entanglement in a quantum ground state. These phases are topological in nature and were introduced to explain the quantum Hall effect[1, 2]. The quantum Hall state does not break any symmetries. Yet, it has key properties, like quantized Hall conductivity and the number of conducting edge modes, which remain stable despite smooth changes in material parameters and it only changes through a regular quantum phase transition. These properties stem from the topological structure of the quantum state.

Although the topological description of the quantum Hall effect is well-established, interest in topological order has surged with the discovery of topological insulators[3–13]. Like conventional insulators, topological insulators contain a bulk energy gap

that separates the highest occupied electronic band and the lowest unoccupied band. However, unlike ordinary insulators, the surface (or edge, in two dimensions) of a topological insulator features gapless electronic states that are protected by time-reversal symmetry. Similar to the integer quantum Hall state, which possesses unique gapless chiral edge states[14], the surface (or edge) states of a topological insulator are topologically protected and display conducting properties distinct from any other known one-dimensional or two-dimensional electronic systems.

The concept of topological order[2] is frequently employed to describe fractional quantum Hall states[15], which necessitate an inherently many-body approach[16] to comprehend. However, topological principles are also relevant to the simpler integer quantum Hall states[1], which can be adequately described using single-particle quantum mechanics. In this sense, topological insulators are akin to the integer quantum Hall effect. Due to the existence of a single-particle energy gap, electron-electron interactions do not fundamentally alter the state. The behavior of topological insulators can be understood within the framework of band theory of solids. It is remarkable that even after more than 90 years, band theory [17]continues to reveal new insights.

1.1 Topology and Band Theory

We'll start by revisiting the fundamental aspects of both topology and band theory. We'll introduce the concept of topological equivalence and elucidate its significance within band theory. Furthermore, we'll explore the profound relationship between bulk topology and the emergence of protected boundary modes. In Section 1.1.4, our focus will shift to the Berry phase, a crucial conceptual tool essential for analyzing topological phenomena.

We start by going over the fundamentals of band theory and topology. We shall define topological equivalency, discuss its significance in band theory, and outline the intricate relationship that exists between protected boundary modes and bulk

topology. The Berry phase, a crucial conceptual tool for the study of topological events, will be covered in Section 1.1.4

1.1.1 Topology

Topology, a field within mathematics, deals with the geometrical attributes of objects that remain unaltered when subjected to smooth deformations. To illustrate, consider closed two-dimensional surfaces within three-dimensional space (see Fig.1.1). For example, a sphere can smoothly transition into various shapes such as the surface of a disk or a bowl. However, a sphere cannot undergo a smooth transformation into the surface of a doughnut. The distinguishing factor between a sphere and a doughnut lies in an integer topological invariant termed the genus, denoted as g, which essentially represents the count of holes. As integers cannot undergo smooth alterations, surfaces with distinct genera cannot be smoothly deformed into one another and are hence termed topologically distinct. Surfaces that can be smoothly transformed into each other are referred to as topologically equivalent. The process of identifying the topological invariants that define a specific object presents an intriguing mathematical problem. For surfaces, a significant theorem, known as the Gauss-Bonnet theorem, asserts that

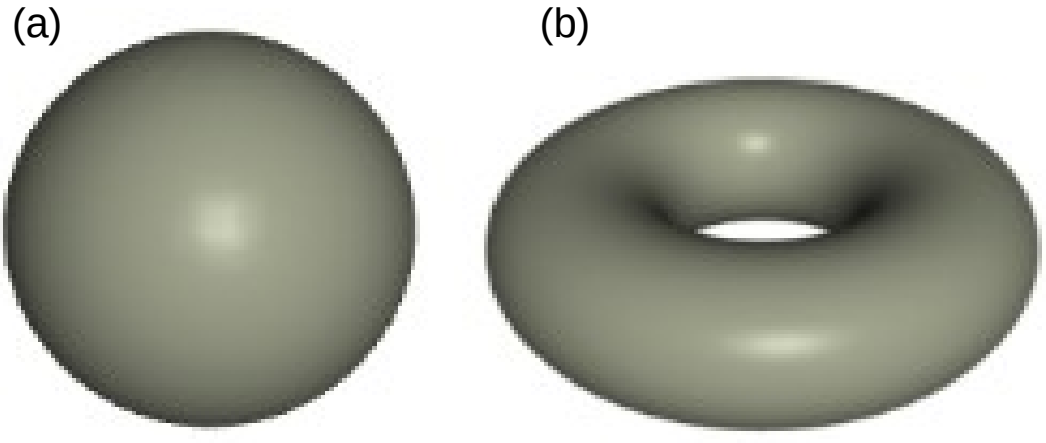

FIGURE 1.1: (color online) Topologically, (a) the surfaces of a sphere (g = 0) and (b) a doughnut (g = 1) are different due to their genus g.

the integral of the Gaussian curvature, represented by K, over a surface establishes an integer topological invariant(χ) identified as the Euler characteristic[18].

$$\chi = \frac{1}{2\pi} \int_S K dA \tag{1.1}$$

The calculation shows that $\chi = 2$ for a sphere with radius R, where $K = \frac{1}{R^2}$. In a broader context, the Euler characteristic is quantized and linked to the genus by $\chi = 2\text{-}2g$. The topological invariants of interest in this chapter follow a similar pattern, although they will describe more abstract entities.

1.1.2 Band Theory

Topology provides a framework for characterizing phases of matter, particularly through the topological classification of insulators. An insulator is a material with an energy gap for electronic excitations, separating the ground state from all excited states. This concept allows for defining topological equivalence based on adiabatic continuity. Insulators are deemed equivalent if they can transition into one another through gradual changes in the Hamiltonian, ensuring the system remains in the ground state throughout. Such a transition is feasible when there's an energy gap E_G, which sets the pace for the adiabatic process. Hence, insulators are topologically equivalent if there exists a continuous path connecting them wherein the energy gap remains finite. Consequently, linking topologically distinct insulators necessitates a phase transition, during which the energy gap collapses.

The task of topologically classifying general gapped many-body states poses a significant challenge that has not been entirely resolved. However, a notable simplification arises when focusing on a subset of states that can be described using the band theory of solids. These band insulators can be effectively understood within the framework of the independent electron approximation, where the many-body ground state is represented as a Slater determinant of single-particle states. This approach does not entail neglecting electron interactions. The presence of an energy gap ensures that the many-body state remains topologically equivalent even

when finite-strength interactions are considered. Consequently, we assume that the state in question can be smoothly transitioned into noninteracting electrons, allowing for the topological classification of band structures. It is then essential to investigate whether the topological distinctions identified within band theory persist when interactions are introduced.

In order to utilise translation symmetry, we will also assume that the material is crystalline. Translation symmetry permits the single particle states to be labeled by their crystal momentum $\mathbf{k}$. The Bloch Hamiltonian can be expressed as follows using Bloch's theorem: $|\psi(\mathbf{k})\rangle = e^{i\mathbf{k}\cdot\mathbf{r}}|u(\mathbf{k})\rangle$, where $|u(\mathbf{k})\rangle$ is a cell periodic eigenstate.

$$H(k) = e^{i\mathbf{k}\cdot\mathbf{r}} H e^{-i\mathbf{k}\cdot\mathbf{r}} \tag{1.2}$$

The band structure is defined by $H(\mathbf{k})$, or equivalently by its eigenvalues $E_n(\mathbf{k})$ and eigenvectors $|u_n(\mathbf{k})\rangle$. There is an energy gap between the lowest empty band and the highest conduction band in an insulating band structure. Lattice translation symmetry requires $H(\mathbf{k} + \mathbf{G}) = H(\mathbf{k})$ for reciprocal lattice vectors $\mathbf{G}$. With $\mathbf{k} \equiv \mathbf{k} + \mathbf{G}$, the periodic Brillouin zone which has the topology of a torus T^d in d dimensions—is where the crystal momentum is thus specified. An insulating band structure can therefore be understood as a mapping from the space of Bloch Hamiltonians with an energy gap to the Brillouin zone torus.

1.1.3 Topological Band Theory and the Bulk-Boundary Correspondence

Topological band theory aims to classify Hamiltonians $H(\mathbf{k})$ that are topologically distinct, thereby categorizing various electronic phases. An essential outcome of this classification arises when encountering a spatial interface between two topologically distinct phases. Visualize an interface where a crystal gradually transitions between these phases as a function of distance y. At some point in this transition, the energy gap must converge to zero; otherwise, equivalence between the two

phases would persist. Consequently, low-energy electronic states become confined to the region where the energy gap passes through zero.

Another goal of topological band theory is to characterize these gapless states. We will observe that they too can undergo topological classification. Moreover, there exists a profound principle known as the bulk-boundary correspondence, establishing a relationship between the boundary topological invariants and the discrepancy in the bulk topological invariants. This interaction between topology and gapless modes is a widespread phenomenon in physics, manifesting across numerous contexts[19–23].

1.1.4 Berry phase and Berry curvature

The Berry phase is important in topological band theory [24]. A quantum mechanical wavefunction's intrinsic phase ambiguity gives rise to the Berry phase. The transition does not affect the Bloch states.

$$|u(\mathbf{k})\rangle \to e^{i\phi(\mathbf{k})}|u(\mathbf{k})\rangle \tag{1.3}$$

This change invites the definition of the Berry connection and is similar to an electromagnetic gauge transformation.

$$\mathbf{A} = -i\langle u(\mathbf{k})|\nabla_{\mathbf{k}}|u(\mathbf{k})\rangle \tag{1.4}$$

The electromagnetic vector potential and $\mathbf{A}$ are comparable. It changes as $\mathbf{A} \to \mathbf{A} + \nabla_{\mathbf{k}}\phi(\mathbf{k})$ under (1.4). The magnetic flux analogue is gauge invariant, even though $\mathbf{A}$ is not. The Berry phase of any closed loop C in k space can be defined as follows:

$$\gamma_C = \oint_C \mathbf{A} \cdot d\mathbf{k} = \int_S F\, d^2\mathbf{k} \tag{1.5}$$

where the Berry curvature is defined by $F = \nabla \times \mathbf{A}$. Here, we'll assume that $\mathbf{k}$ is two dimensional for the sake of notational simplicity. It is simple to generalise to higher dimensions.

The phase gained under an adiabatic cycle is described by the Berry phase, which has numerous uses in physics. It will be helpful for categorising loops in momentum space in the current scenario.

1.2 Topological Phase Determinants

Topological phases of matter emerge within a system featuring spin-orbit coupling, leading to a band inversion when symmetry is either protected or broken. Additionally, topological invariances play a crucial role in defining phase transitions under the adiabatic deformation of the system. Hence, it becomes evident that the primary determinants of topological phases in quantum materials include spin-orbit coupling, band inversion, and symmetry-protected or symmetry-breaking topological invariance. Many of these topological or quantum phases have been identified through the quantum analogs of various Hall measurements.

The preceding section provided a brief overview of symmetry concepts, while the subsequent section will delve into different Hall effects observed in topological/quantum materials. This section will explicitly examine additional important elements impacting topological phases, such as spin-orbit coupling and band inversion.

1.2.1 Spin-orbit coupling

Quantum Hall insulators represent the pioneering quantum phases requiring an external magnetic field for their demonstration. With the application of an external magnetic field, the system's time-reversal symmetry is disrupted, leading to the emergence of chiral edge states devoid of backscattering, attributed to the cyclotron motion of electrons. The realization of topological states of matter

occurred through substituting the external magnetic field with the spin-orbit coupling (SOC) field, now safeguarded under time-reversal symmetry and providing Kramers degeneracy. Hence, spin-orbit coupling serves as the primary framework for developing topological materials, fostering the creation of Kramers degenerate edge states alongside band inversion and enabling the existence of relativistic fermions.

SOC denotes a quantum magnetic field within an atom of a Kramers' system, featuring spin-orbit interactions that induce a transverse magnetic force on an orbiting electron within the external electric field generated by the nucleus' charge[25, 26]. This relativistic quantum mechanical effect results from the charged particle's momentum-dependent motion within the atom's electric field. The intrinsic magnetic field of the atom can be determined from the Thomas-term[27].

$$H_{soc} = \frac{-1}{2m_0^2c^2}\mathbf{S}\cdot\mathbf{L}\times(\nabla V) = \frac{-\hbar}{4m_0^2c^2}\sigma\cdot p\times(\nabla V) \tag{1.6}$$

where p is the momentum vector, V is the Coulomb potential, σ is Pauli's spin matrix, S and L are spin and orbital angular momentum, respectively, and m_0 is the electron mass. As seen in Fig.1.2, SOC offers band splitting and band inversion

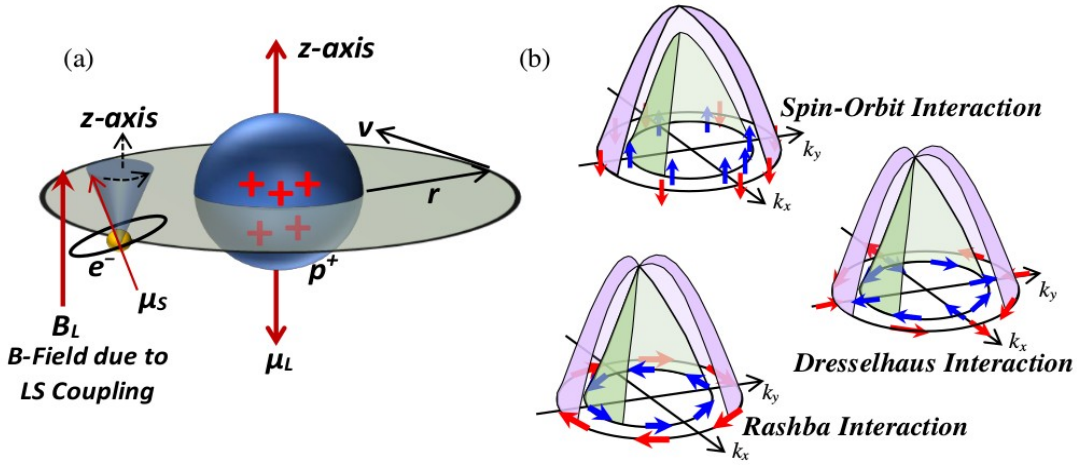

FIGURE 1.2: Illustration of (a) an electron's spin and orbital angular rotations around the nucleus, demonstrating the spin-orbit or LS coupling phenomenon. (b) three distinct spin-orbit relativistic interactions: spin-orbit interaction, Dresselhaus interaction, and Rashba interaction (derived from 29).

in the energy band, often referred to as LS coupling, in the atomic world. From the first-order perturbation theory, the energy eigenvalues resulting from the spin-orbit interaction can be written as[28],

$$E_{\mathrm{SOC}} \approx 2Z\mu_B^2\langle\frac{1}{r^3}\rangle\langle\mathbf{L}\cdot\mathbf{S}\rangle \approx \frac{1}{2}a\hbar^2[J(J+1)-L(L+1)-S(S+1)] \tag{1.7}$$

In this case, a is the spin-orbit coupling constant, which is proportional to Z^4, and Z is the atomic number. A molecule can also experience another kind of energy band splitting that is proportional to Z and is referred to as an electrostatic effect caused by e-e repulsion. Thus, in systems with light atoms, the electrostatic effect is dominating, whereas in systems with heavier atoms, spin-orbit coupling is dominant. Additionally, for each J energy level, the spin-orbit coupling yields a (2J+1) degeneracy. Any crystal can have SOC, an interaction that is independent of symmetry. However, there exists a symmetry dependent SOC, exclusive to crystals lacking inversion symmetry. The terms "Dresselhaus interaction" and "Rashba interaction" refer to these SOCs. The band structure and spin orientations[29] of the three different types of SOCs found in the material systems are shown in Fig.1.2.

1.2.2 Band Inversion

Band inversion is a key feature of inversion symmetric topological insulators. An electron-like band with a positive effective mass is inverted to a hole-like band with a negative effective mass under the phenomenon of band inversion. The lowest conduction band in a typical non-topological system has even parity, while the highest valence band has odd parity. Odd parity bands are replaced by even parity bands in narrow band-gap semiconductors with heavier atoms and high spin-orbit interaction, eventually introducing topological phases into the material. Band inversion is an important approach for detecting topological phases in materials, but the materials must also match the topological invariance criteria. Topological insulators often have an odd number of band inversions between opposing parity

bands. PbSnTe_2 is topologically trivial since the number of band inversion is even and happens at both Γ and three X points. However, Dirac cone[30, 31] and even band inversion are also possible in topological crystalline insulators. Many sorts of band inversions are seen in topological materials: At the Γ point, band inversion occurs between the s and p bands, as well as between two p^z orbitals of opposite parity[32, 33]; and band inversion between d and p bands at Γ point[34]. Without involving SOC interaction, band inversion can also be achieved via lattice strain.

1.3 Hall effects and topological phases of matter

The disintegration of time-reversal symmetry in the presence of SOC has been linked to the Hall effect since its discovery. Two currents—longitudinal and transverse currents—exist in typical Hall effects when there are mutually perpendicular electric and magnetic fields. While the longitudinal current breaks time-reversal symmetry by dissipating heat in accordance with the second rule of thermodynamics, the dissipationless transverse current does so immediately. Since the topological or quantum phases were first detected in Hall measurements and identified from the Hall resistance, Hall measurements are therefore regarded as an essential fingerprint of those phases. Different topological phases are determined on the basis of distinct Hall observations. The various forms of Hall families that map to various topological classes are the main topic of this section. The graphic illustrates the quantization of the Hall resistance, which is comparable to the quantum resistance of $\frac{h}{e^2}$, where e is the elementary charge and h is Planck's constant, respectively. It does this by showing generalised longitudinal and transverse Hall resistivity for all Hall families.

1.3.1 Anomalous Hall effect: Hall effect with band structure Berry curvature

Edwin Hall noticed that magnetic metals, such as nickel and iron, exhibit an unusual transverse voltage. Magnetization and anomalous transverse voltage with a magnetic field exhibit a similar qualitative trend. The anomalous Hall voltage and magnetization are related empirically in the following way:

$$H_e = H_0 + 4\pi M\alpha R_H = R_0(H_0 + 4\pi M\alpha) \tag{1.8}$$

where the magnetic field (H) and magnetization (M) are the respective values. When Karplus and Luttinger returned to the issue in 1954[35], they found that anomalous Hall conductivity and spin-orbit coupling were directly correlated, which was consistent with experimental findings.

$$R_{AHE} \sim \frac{B_{s.o}}{m^*} R_{xx}^2 \tag{1.9}$$

The second part in Eq.1.10 describes how the electrons acquire an anomalous velocity perpendicular to the electric field. Over occupied bands, the anomalous velocity is finite and remains independent of the longitudinal conductivity and, thus, the scattering rate. For this reason, it is called the inherent anomalous Hall effect. The Berry curvature can be explained as an effective magnetic field that results in a Hall conductivity using the TKNN formula:

$$\frac{d\langle r\rangle}{dt} = \frac{\partial E}{\hbar \partial \mathbf{k}} = \frac{e}{\hbar}\mathbf{E} \times (\nabla_k \times A_{ks})_z \tag{1.10}$$

Haldane recently returned to the issue as a "topological Fermi-liquid" property. Haldane solely considered the quasiparticles' adiabatic motion near the Fermi surface [36]in order to account for the accumulated Berry phase. Recently, Nagaosa et al.[37–39] presented a comprehensive theoretical framework that takes into account both the intrinsic and extrinsic anomalous Hall effects. The intrinsic anomalous

Hall conductivity is related to the Berry curvature and is not affected by scattering. Additionally, the anomalous Hall conductivity is quantized using integer quantum conductance values($\frac{e^2}{h}$) via the TKNN formula.

$$\sigma_{xy}^{AHE-int} = -\varepsilon_{ijl}\frac{e^2}{\hbar}\sum_n \int \frac{d\mathbf{k}}{(2\pi)^d} f(\varepsilon_n(\mathbf{k}))(\nabla_k \times A_{ks}) \tag{1.11}$$

where the antisymmetric tensor and the Fermi-Dirac statistics, with summing over all of the full bands, n, are represented by the variables ε_{ijl} and f($\varepsilon_n(\mathbf{k})$. The side jump or skew scattering is usually the cause of the extrinsic anomalous Hall effect. When electrons from the spin-orbit coupling to impurity atoms scatter asymmetrically, it results in an effective TRS breaking of charge carriers, which is known as skew scattering. A side jump (SJ) is the time-integrated velocity

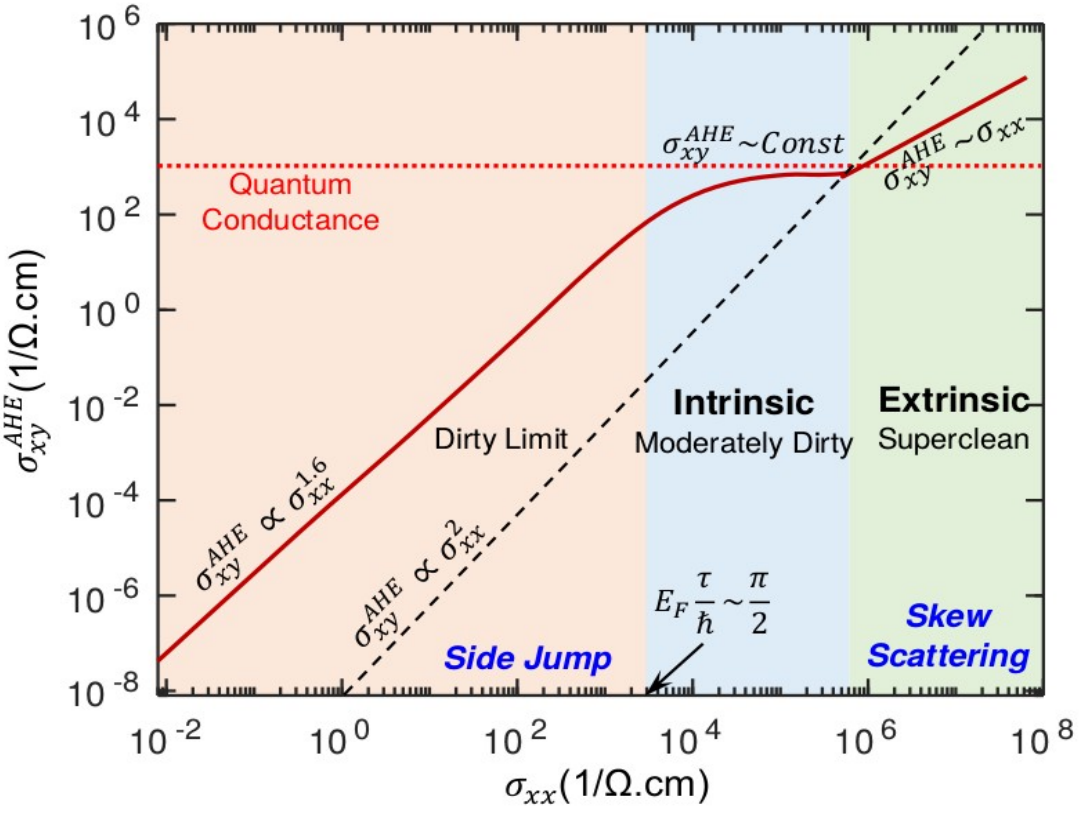

FIGURE 1.3: (color online) anomalous Hall conductivity in relation to longitudinal conductivity. In particular, intrinsic dissipationless topological transport controlled by Berry curvature is highlighted by the insensitivity of Hall conductivity to scattering (longitudinal conductivity; adapted from 37).

deflection of electrons as they engage with an impurity or disorder. The intrinsic and extrinsic components of the anomalous Hall voltage are both present.

$$\sigma_{xy}^{AHE} = \sigma_{xy}^{AHE-int} + \sigma_{xy}^{AHE-skew} + \sigma_{xy}^{AHE-SJ} \tag{1.12}$$

Information regarding the band structure topology is only available in intrinsic AHE. For constant spin-orbit coupling energy ($E_{so} < E_F$)[37], three regimes and two crossovers have been identified: The clean regime (i) is defined as follows: it is characterised by an insignificant scattering rate ($\hbar/\tau \leq u_{imp}E_{so}D$); (ii) the moderately filthy regime ($u_{imp}E_{so}D \leq \hbar/\tau \leq E_F$); (iii) the dirty regime ($E_F \leq \hbar/\tau$). In the clean regime, skew scattering is dominant in the AHE. The relationship between skew scattering and impurity density is inverse. The density of states and the impurity potential are represented by D and u_{imp}. Because of the intrinsic Berry phase contribution[40], Hall conductivity in the moderately unclean regime becomes insensitive to scattering (i.e., longitudinal conductivity, σ_{xx}). In the unclean regime, a power-law scaling of the transverse conductivity with longitudinal conductivity is expected. These three regimes are plotted against longitudinal conductivity and impurity density in Fig.1.3[41].

1.4 Topological Insulators and Semimetals in 2D and 3D

Quantized Hall conductivity, or transverse magneto conductivity, can be used to investigate the unique surface/edge states in momentum space that are dictated by the topology of the bulk band structures in topological insulators and semimetals, two quantum phases. Topological phases are well defined by their associated topological invariants, that is, adiabatic variations of topological phases that remain unchanged under adiabatic deformation, as was discussed in the preceding sections. In 2D and 3D materials, topological phases have already been noted.3D topological phases, such as topological semimetals, are characterised by

four topological invariants (ν_0; ν_1, ν_2, and ν_3), where ν_0 represents strong topological invariant and ν_i's (i=1,2,3) are weak topological invariant. In 2D, quantum phases known as 2D topological insulators (TIs), such as integer quantum Hall (IQH) insulators, fractional quantum Hall (FQH) insulators, and quantum spin Hall (QSH) insulators, are characterised by single-valued topological invariants, notably Z invariance. Even though 2D topological states (IQH, FQH, and QSH) were first observed, it was difficult to physically realise these phases because they needed semiconductor heterostructures with ultraclean interfaces at low temperatures. Topology-protected metallic states[42] could only be observed through the Hall measurement. In contemporary condensed matter research, 3D topological materials have received a lot of attention because of the experimental difficulties in 2D topological states, the ease with which 3D topological phases may be experimentally realised, and their unique topology-protected features. Many novel properties of topological phases may now be shown both theoretically and practically because of tremendous advances in topological material research. To give readers a comprehensive picture of the current research advances on topological materials, this section focuses on presenting the various conspicuous properties of relevant topological phases together with their prospects and obstacles.

1.4.1 Dirac semimetals

The Dirac relativistic equation of electron ($H = c_p\alpha + (mc^2)\beta$ where, c is the speed of light and α, and β are the coefficient matrices) has been known since 1928. It states that in the ultra-relativistic regime (where kinetic energy predominates over mass, $c_p \gg mc^2$)[43], the energy dispersion relation becomes linear. As illustrated in Fig.1.4, the Dirac fermion decouples into two Weyl fermions with specific chirality and helicity in this domain of nearly zero mass and correct chirality. These fermions are then fixed at respective momentum positions[43]. Similar to TIs, Weyl points are only visible when a single point close to the Fermi level is where two non-degenerate bands cross. In graphene[44], sometimes referred to as a 2D Dirac semimetal (DSM), the first Dirac fermion in a solid-state band

structure was detected. In Dirac semimetals, topological surface states usually don't have a bulk energy gap. Discrete lattice symmetry protects TSSs of 2D Dirac semimetals, but additional symmetry protection is needed to realise Dirac semimetals in 3D because $m\sigma_z$, a mass term in the electron Hamiltonian will open an energy gap in the presence of SOC (this mass term is absent in 2D Dirac semimetals). The 3D Dirac semimetal phase typically arises as an intrinsic phase in the presence of extra symmetry protection, primarily from rotational symmetry, or during the phase conversion from normal insulator (NI) to topological insulator (TI). Materials with both TRS and inversion symmetry preserved with additional space group protection can also exhibit 3D Dirac semimetal phases. This finally results in two Weyl points with opposite chirality at a single Dirac point, as illustrated in Fig.1.4, and makes the material four-fold degenerate[45]. As a result, upon breaking either TRS or inversion symmetry, these materials with strong SOC can turn into Weyl semimetals. Dirac nodal line and topological superconductor are examples of further derivative topological phases from DSM (Fig.1.4). Due to the delicate merger of two low energy Weyl nodes under the protection of numerous symmetries, high mobility DSM phases are unstable in stoichiometric single-crystalline systems, which makes the observation of DSM in real materials difficult[46]. Furthermore, because DSM phases arise at the critical point of the NI-TI phase conversion boundary, it is necessary to adjust the chemical composition or strain in the required materials to observe DSM, which frequently leads to systemic illness[46]. Some potential materials have an extra Fermi surface[9] and a bandgap at the Dirac point. However, there are two ways to obtain DSM phases: symmetry-enforced Dirac nodes with or without SOC[45], and band inversion method in which Dirac nodes emerge from the lattice symmetries (mainly rotational symmetry) driven accidental band crossing into an inverted band structure of a topological insulator. Unique quantum features of DSMs are covered in the ensuing subsections.

1.4.1.1 Properties of Dirac Semimetals

Two surface Fermi arcs connecting a pair of Dirac points on the surface, as depicted in Fig.1.4, are the primary characteristic of DSM, which was determined by theoretical calculations and observed in the experiment. The Fermi arc in DSMs is weak, not topologically protected, and is thought to be a composite of two Fermi arcs of Weyl semimetals[45] because of the four-fold degeneracy and zero Chern number of Dirac points. Additionally, the location of the edge states on energy contours[45] determines the characteristics of the Fermi arc of DMSs. A

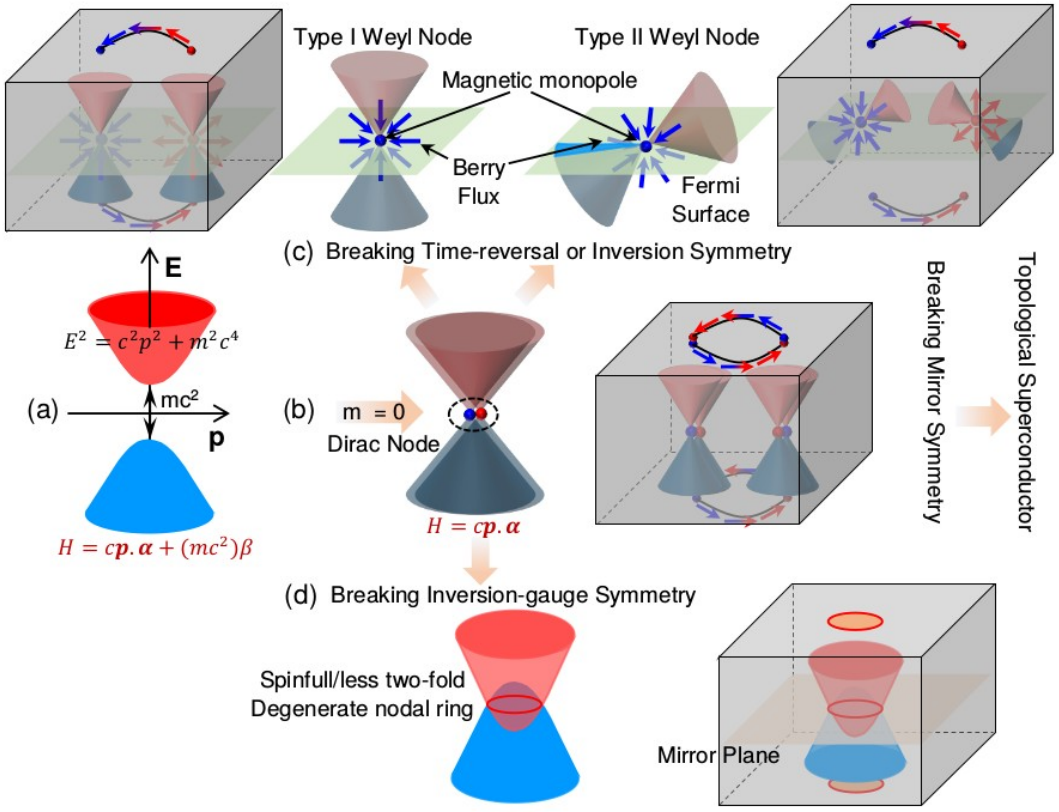

FIGURE 1.4: (color online) (a) Band Structure of a free Dirac Particle with mass-dependent energy gap. (b) One Dirac node generates two (degenerate) Weyl nodes of opposing chirality, demonstrating the relativistic character of the Dirac particle at massless conditions. (c) When TRS or inversion symmetry is broken, the Dirac node can split into two types of Weyl node pairs (type I and type II Weyl nodes), producing Weyl fermions with a distinctive magnetic monopole and Berry flux. (d) Inversion-gause symmetry breaking leads to the formation of the Dirac nodal ring. For every topological phase, bulk and surface states are displayed together with their distinguishing characteristics. A topological superconductor is achieved through the violation of mirror symmetry(adapted from 47 and 50).

chiral anomaly at the Dirac node of DSMs is a subtle topological phenomenon, comparable to the Fermi arc, that results from the coexistence of two opposed chiralities at a similar momentum location that are shielded by reflection or rotational symmetries. DSMs possess remarkable electrical transport properties such as enormous magnetoresistance[47, 48] and ultrahigh mobility in addition to their distinct topological features. Cd_3As_2 was found to have an extremely high mobility of 9×10^6 cm^2/Vs at 5K and a 0.25 mm mean-free path at 6K[48, 49]. DSM's ultrahigh mobility is mostly due to the backscattering-less energy states for carriers at zero magnetic fields, which can provide up to 104 times longer transport lifetime [47] than the quantum lifetime. Weyl semimetals[50], topological insulators, and topological nodal lines can all be driven by DSMs(Fig.1.4), as DSM states need multiple symmetry protection, and breaking one symmetry can lead to the creation of additional topological phases. Additionally, it was revealed that DSM materials might be turned into topological superconducting insulators[45] by applying pressure and doping to support Majorana fermions and produce a superconducting gap in the bulk band structure.

1.4.2 Weyl Semimetals

Hermann Weyl predicted the existence of massless Weyl fermions theoretically in 1929. It was anticipated that they would show up as opposite-chirality pairings. In quantum materials, Weyl fermions are found in Weyl nodes, which function as magnetic monopoles with Berry flux and exhibit a nontrivial topological influence on Berry curvature (Fig.1.4). In 2011[51], Weyl fermions were expected to be realised in Weyl semimetals (WSMs), and in 2015, this was experimentally confirmed[52, 53]. Weyl nodes, or the band contacting point between the valence and conduction bands near the Fermi level with a linear dispersion relation, typically occur in an area of the Brillouin zone that is bounded and shielded by symmetry. As previously noted, the band degeneracy at TRIMs can be obtained from DSMs by violating either TRS symmetry or inversion. Symmetry dictates the amount of Weyl points in WSMs.Since a Weyl point in a TRS WSM and

its time reversal partner have the same chirality, the Fermion doubling theorem requires the existence of two other Weyl points with opposing chirality. Consequently, there are multiples of four Weyl points in WSMs with TRS. Conversely, WSMs protected by inversion symmetry have two Weyl points. WSMs can be categorised into three groups according to how the Weyl cone tilts, due to the Weyl Hamiltonian's effective velocity parameter, v. (i) Large v causes tilting in the Weyl cone, resulting in Type II[54] or structured WSMs with a touching point between electron and hole pockets and open constant energy surfaces (Fig.7.5); (ii) Small v results in Type I WSMs with conventional Weyl points and a point-like Fermi surface, as shown in Fig.7.5. (iii) The quadratic component causes quadratic tilting in the Weyl cone, resulting in Type III WSM with two contacted electron or hole pockets (Fig.7.5). Type II WSMs have track states [45], and Type III WSMs [55] have extended Fermi arcs with multi-fold helicoidal surfaces, all types of WSMs contain surface Fermi arcs. A different kind of WSM phase with a nodal line state on the Fermi surface[56, 57] has been described in the literature as critical-type WSM. Some literature has also reported critical-type WSM as type-III WSM. A critical type typically consists of a dispersive band and a flat band, with the crucial band dispersion falling between Type I and Type II. Since Weyl points typically do not occur along high-symmetry lines and planes, it can occasionally be difficult to determine the number of Weyl points and Weyl nodes in the Brillouin zone. However, this issue can be avoided by getting band structure without the need for SOC[58].

1.4.2.1 Properties of Weyl Semimetals

Among the special characteristics of Weyl fermions is a magnetic monopole. The Berry curvature, which is thought of as an effective magnetic field in the momentum space, is connected to the topology of the Weyl point in the Fermi surface. As magnetic monopoles, Weyl nodes on the Fermi surface serve as both a source and a sink of the Berry curvature. The integral over the Fermi surface surrounding the Weyl node can be used to determine the magnetic charge of the node, which is referred to as chirality[58]. As seen in Fig.1.4, Weyl points on the Fermi surface

also create the Fermi arc connecting the surface projections of two Weyl nodes in WSMs. The monopole property of the Weyl fermions guarantees the existence of Fermi arcs in the Fermi surface of surface states. Bulk Weyl points connect topologically protected Fermi arcs on opposing surfaces. Owing to their distinct transport characteristics, WSMs are gaining more attention across numerous application domains. The terminating ions on the surface often govern the shape and energy dispersion features of Fermi arcs in WSMs, whilst the strength of SOC[58] determines the length of Fermi arcs and the distance between Weyl points. It has been observed that the Kohn anomaly[59] in phonon spectra can represent the electron topology of Weyl nodes. Large magnetoresistance (MR), high mobility, chiral anomaly, and Fermi surface are all determined by strong quantum oscillations, linear dispersion, and nontrivial Berry phase in the band structure, which distinguish WSMs from DSMs in their strong chiral magnetotransport. Reconstructing the Fermi surface usually involves angle-dependent quantum oscillations such as SdH and de Hass-van Alphen (dHvA) oscillations, since the origin of these magnetic field-dependent quantum oscillations is associated with the various kinds of Fermi surface pockets[58]. WSMs exhibit high mobility, similar to DSMs, which is caused by chiral and nearly massless Weyl fermions. The Fermi level and the scattering processes can be altered by sample quality, which in turn affects the carrier mobility in WSMs.Under parallel electric and magnetic fields, a charge current flow between distinct chiral Weyl modes separated in k-space is expected to exist. This process's imbalance in chiral charges results in chiral anomaly, which causes an axial current flow because it prevents electric charges from being conserved. While negative longitudinal magnetic resonance (MR) can still be detected in a system with poorly defined chiral quasiparticles at the Fermi level, a chiral anomaly in WSMs can improve conductivity[60].

1.5 Other Topological Semimetals

The other class of topological semimetals are called topological nodal line semimetals (TNLSMs), which differ from DSMs and WSMs in that they have a line of

band crossing rather than a point-like band crossing (Fig.1.4). The many forms of nodal line semimetal phases are defined by a few crystal symmetries, such as mirror symmetry and glide symmetry, in addition to time-reversal and/or inversion symmetries (Fig.1.4). Z topological invariants are typically used to define screw rotation protected double nodal line semimetals and mirror symmetries protected TNLSMs, while Z_2 invariants[61] are typically used to define time-reversal, inversion, and spin rotation symmetries protected nodal semimetals. By disrupting the protective symmetry of the TNLSM phase, conversion into various topological phases such as topological semimetals, topological insulators, and other TNLSMs[62] can be accomplished. Therefore, by violating various kinds of symmetries, TNLSMs can offer the evolution into new topological phases. One of the main problems with TNLSMs is experimental observation because they typically lack topologically protected border states. The nodal band structure is determined with a low precision using ARPES, and the Fermi surface map and Berry phase[61] are defined using quantum oscillation measurements. Numerical and magneto-optical measurements are also carried out to examine Berry curvature effects[63], surface states, and nontrivial bulk response. A topological insulator with TRS breaking and a tunable superlattice of the normal insulator make up the theoretically and experimentally realised material system for TNLSMs. The quantized π Berry phase ensures the nodal ring's[64] stability even in cases when it is challenging to observe in Dirac NLSMs. Dirac NLSMs show parity anomaly, which can result in a little inversion breaking that induces an abnormal transverse current when exposed to an electrical field.

1.6 Topological Semimetal Material Families

Prediction and experimental realisation of three-dimensional materials having Weyl or Dirac fermions in the bulk states have been interesting areas, motivated by graphene. There are areas where the valence and conduction bands of a Weyl semimetal touch in its band gap. If we ignore the spin degeneracy, then these band contacting sites are nondegenerate because they break either the inversion

symmetry or the time-reversal symmetry. These contact sites remain stable even in the presence of tiny perturbations and are frequently referred to as Weyl nodes. Weyl nodes appear in pairs in their closed proximity with opposite Chern numbers. Weyl nodes can be combined into pairs and produce Chern number 0 at the merged locations by adjusting the Hamiltonian parameters. Since they lack topological protection, these points are not stable; however, they can be made stable by adding an extra group symmetry. These stable points are then referred to as Dirac points. Thinking of these materials as properly-tuned topological insulators with the bulk gap closed is an alternate interpretation of them. A multilayer topological insulator structure was postulated in 2011 as a Weyl semimetal[65] realisation. Two Weyl nodes can arise in the BZ by sandwiching thin films of magnetic doped topological insulators between layers of ordinary insulators. For the material consideration, the TaAs family, which includes TaAs, TaP, NbAs, and NbP[58, 66, 67], is representative of Type I Weyl semimetals.Typical Type II Weyl[58] semimetals are WTe_2, $MoTe_2$, WP_2, and MoP_2. As previously mentioned, the Dirac cone is skewed within the BZ. Large transverse magnetoresistance and high conductivity are also noted. It was also reported that sputtered WTex was a Weyl semimetal. The magnetic Weyl semimetals, also known as Weyl semimetals that break time-reversal symmetry, are commonly found in $Co_3Sn_2S_2$, $YbMnBi_2$, GdPtBi, $Y_2Ir_2O_7$, and $HgCr_2Se_4$[68, 69]. Weyl nodes can be realised utilising an external magnetic field. Weyl semimetals that break inversion symmetry have minimal Weyl nodes of four, while magnetic semimetals have the potential to have two minimal Weyl nodes. As a result, the magnetic Weyl semimetals provide a more straightforward framework for researching the chiral anomaly and Fermi arc.

1.7 Topological Phase Conversion in Device Applications

As previously indicated, regulated and dependable topological phase switching in a device structure is necessary to incorporate the topological phases into real-world

applications. Topological phase conversion techniques are therefore important in terms of technology. The unique topological properties are thought to present great opportunities for numerous current and next device uses. Topological materials have many appealing properties, yet they are still behind in device applications because of a few significant obstacles. Prior to their technological application, a number of factors need to be taken into account, including the topological material's compatibility with current devices, their ease of fabrication and batch processing, their compatibility with topological or quantum behaviour under external stimuli, their working temperature range, their cost-effectiveness, their practical structure, and their ease of use[70]. Condensed matter research has put a lot of effort into overcoming the challenges posed by topological materials for use in devices. This section provides an overview of a number of cutting-edge application sectors where topological properties show promise. The physical device structures for the various applications are shown in Fig.1.5. Topological phase conversion finds widespread use in electronics when switches are used as logic devices. Building field-effect transistors (FETs) that operate based on the topological phase transition is thus the subject of numerous investigations. Because there is no backscattering, the great carrier mobility of topological transistors allows for dissipationless operation at extremely high speeds. A topological transistor typically consists of the topological channel, a substrate, and one or two high-k dielectric gate layers. To produce switching behaviour, a topological insulator to normal insulator phase conversion with E-field tuning is typically used. Additionally, a topological transition with dual TI layers shielded by multiple symmetrys is disclosed, in which the spin texture of TSS retained by one symmetry[71] can be altered by breaking another. In addition to TIs, topological crystal insulators, or TCIs, may offer an additional stage in the realisation of transistor activity since they possess topological states that are protected by crystal symmetry[72] as opposed to time-reversal symmetry. In contrast to bulk semiconductor transistors, topological surface states enable carrier transport at the topological layer's surfaces.

Quantum bits, or qubits, are a novel application of topological materials in quantum computing. The endeavor to construct quantum computers presents multiple

approaches to conceptually create a quantum equivalent of a classical computer. Two significant obstacles to the effectiveness of quantum computers are noise and qubit decoherence, which can be uniquely suppressed by topological states[73]. In order to realise qubits, the non-abelian statistical state of matter can function as a physical system[74]. Non-abelian anyons, as this form of matter is commonly called, are collective composite particles that live in a quantum system with a bandgap between the excited and ground states. Additionally, chiral Majorana fermions have the potential to function as qubits[75]. The physical realisation of the qubit system remains a hurdle in the field of quantum computing. Researchers still haven't fully grasped their intricate principles and workings. As a result, there is a lot of activity in this area of topological study, and it has a bright future.

In the ongoing search for high-performance materials for solid-state energy conversion[76–78] from thermal to electrical or vice versa, thermoelectricity is another important field of study. Overcoming the fermionic restriction on the intercoupled thermoelectric material properties[79] is the main task facing thermoelectric research today. People have also looked into the contributions from magnons and para magnons as new avenues for a high thermoelectric power factor[80–82] to obtain a non-fermionic improvement in thermoelectric performance. Since heavy atoms are present in a large number of thermoelectric materials and topological systems, several topological materials can also be excellent candidates for thermoelectric applications[83–86]. Since heavy atoms are present in a large number of thermoelectric materials and topological systems, several topological materials can also be excellent candidates for thermoelectric applications. However, because of the significant bipolar contributions in thermopower and thermal conductivity, additional materials engineering and optimisation are needed for topological thermoelectric materials to reach their maximum performance. It is possible for bipolar effects to drastically lower thermoelectric performance[79]. Thermal switches are an additional thermal device application for topological materials that regulate the entropy flow through the surface and bulk states in response to external stimuli, in addition to thermoelectric devices.

Topological materials exhibit unusual optical properties, such as Kerr and Faraday rotation, ultrahigh bulk refractive index, unusual electromagnetic scattering, near-infrared frequency transparency, and ultra-broadband surface plasmon resonances[87], in addition to their electronic and spin properties. These remarkable optical properties point to the potential use of topological materials in novel optoelectronic applications, such as broadband photodetectors, ultrathin holograms, plasmonic and Fresnel lenses, Veselago lenses, scanning tunneling microscope tips, nanoscale waveguides[87, 88]. Conversely, backscattering-less topological states have the potential to enable next-generation photonics applications, including optical signal processing[89, 90], light source, and transmission devices. Optoelectronic and condensed matter societies are very interested in employing topological materials in laser applications because of the significance of laser devices in a variety of application fields[91, 92]. However, similar to other applications, obstacles related to the quality of the structural interface, effective and dependable control, and thorough comprehension of the topological optical properties also affect topological optoelectronic or photonic device structures.

The advent of spintronics in device applications offers the special benefits of the rapid operation and almost negligible Joule heating. Topological materials are

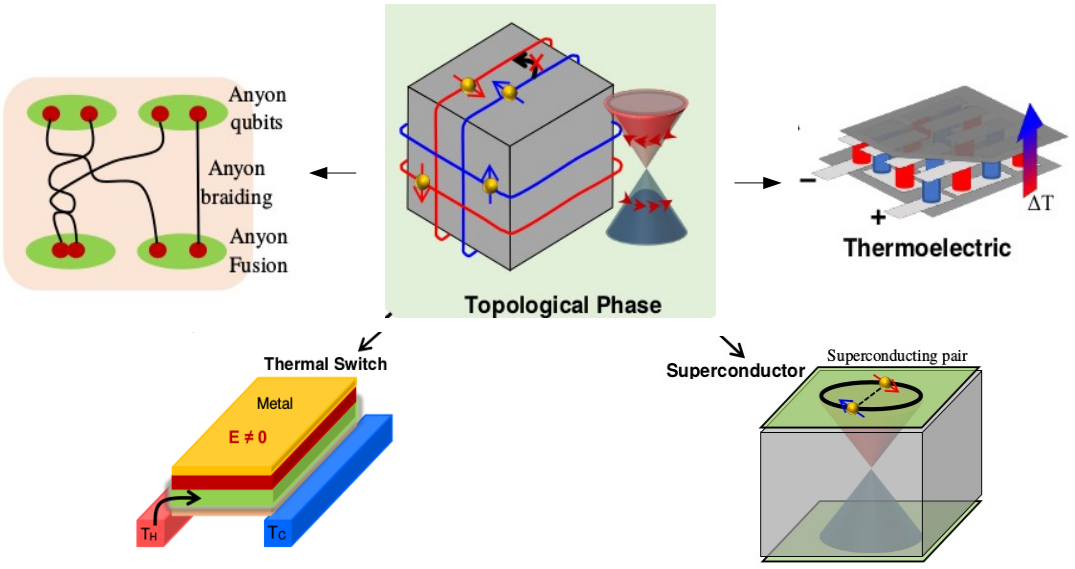

FIGURE 1.5: (color online) A wide range of device application domains for both the physical and topological phases of matter are available (adapted from 70).

suitable for spintronics applications[93] because of several spin properties of topologically protected robust surface states, such as strong spin-momentum locking, high charge current to spin current conversion efficiency, long spin diffusion length, strong magnetoresistance, and high spin filtering efficiency. Potential candidates for future energy-efficient spintronic devices include semimetals and topological insulators. Spin-filter transistors, Weyl semimetals[94], and topological insulators can be used to create spin-torque transistors, memory devices, and other common topological spintronic device applications.

Superconductor research is an additional fascinating area of study. The Bose-Einstein condensed Cooper pairs[95] are present in simple superconducting materials. But unlike Cooper pairs, the topological phase in superconductors is different. In addition to having non-zero topological invariants[95], topological superconductors typically feature a fully open gap between the ground and excited states. In addition to having non-Abelian Majorana zero mode originating from the spinless pairing of the time-reversal breaking s-, p-, or d-waves with spin-orbit coupling[96], topological superconducting states also possess parity-hole symmetry. In topological superconductors, a Majorana fermion has special characteristics. It is a quasiparticle that can arise from the superposition of an electron with a hole that has the same direction or spin[97, 98]. It is also its own antiparticle. Superconducting states in 1D or 2D topological surface states are typically demonstrated by topological insulators in 2D and 3D, respectively. However, superconducting states[95] can also be seen in Dirac and Weyl semimetals, topological crystalline insulators, and semimetals. Topological superconductors display a variety of distinctive characteristics, including odd-frequency Cooper pairs, quantized thermal Hall conductivity, nematicity, anomalous Josephson effects, and zero-bias conductance peak. For quantum computing, Majorana superconducting mode physical qubits can also be used. Even with the advancements in topological superconductors, further research is still needed to fully comprehend the physics underpinning the other superconducting states. More experimental research is required for topological superconducting materials because the real environment differs from theoretical predictions.

In addition to the applications listed above, there are further uses, including various sensor kinds, lab environments with black holes, and on-chip high-performance micro-ultrasonic devices[88, 99, 100]. Topological materials are shown to be appropriate for a variety of sensing applications, including strain sensors[101], gas sensors[100], magnetic sensors[102], and wireless sensors[103].

In order to assess the topological phases' performances in nano-devices[104], a number of studies have been conducted recently on their nanostructuring. Nonetheless, there are particular difficulties in the characterisation[104] and production of nano-structured topological phases. More exciting device applications may arise from ongoing research into topological materials, phases of matter, and phase conversion mechanisms. A more theoretical and experimental study is needed to understand the underlying physics, fabrication methodologies, control mechanisms, and appropriate material systems in order to properly implement the topological/quantum phases of matter into device applications.

1.8 Overview of present thesis

It is clear from the numerous examples given in the earlier sections that different types of systems display a range of characteristics that are not fully understood at the microscopic scale. Therefore, principles computations on these materials have been the most evident choice for making precise forecasts at the microscopic level. It is very obvious that notable enhancements in computational methods and resources have made reaching this stage easier. First principles computations help in grasping the structure and several fascinating and intriguing characteristics of these materials, which at first sight appear to be highly complex with a broad range of degrees of freedom. This comprehension at the microscopic scale creates new opportunities for designing innovative functional materials. A deeper understanding of the interaction between different orders such as magnetic, charge, and orbital degrees of freedom could lead to the discovery of materials with desirable functional characteristics. Additionally, first principles computations can

create more accurate links between actual systems and simplified models to understand the fundamental physics of the materials, leading to conceptual progress and stronger interaction between theory and experiment.

In this thesis, six different compounds have been studied. Therefore, the thesis can be considered to be divided into two parts: the first part deals with novel properties arising from the phenomena of gapped nodal lines and Weyl points in semimetallic compounds, and the second part focuses on the model Hamiltonian with non-trivial band topology.

First-principles calculations based on advanced Density Functional Theory techniques and model Hamiltonian approaches have been performed on these materials to understand the exciting properties they exhibit from a microscopic point of view. The contents of the various chapters discussed in this thesis are organized as follows:

1.8.1 Chapter2

In this chapter, we discuss the theoretical methodology of our calculations. This includes both the theoretical background of Density Functional Theory (DFT) and its practical application for solving a many-electron Hamiltonian. Additionally, we cover the different basis sets considered during our calculations, depending on the properties studied. We also discuss the construction of low-energy model Hamiltonians for such complex materials, starting from first-principles calculations.

1.8.2 Chapter3

Firstly, we have studied magnetic topological semimetals (TSMs) with broken time-reversal symmetry. Among various magnetic TSMs, Co_2-based full Heusler compounds are of current interest, as some of these materials exhibit Weyl and nodal fermions in their topological band structure. In this work, we report a comprehensive study of the anomalous Hall effect (AHE) in the ferromagnetic

full Heusler compound Co_2VAl. First-principles calculations reveal that the Berry curvature originating from a gapped nodal line and symmetry-protected Weyl nodes near the Fermi level (E_F) is the primary source of AHE in this compound. Thus, this investigation of Co_2VAl discloses that it is a ferromagnetic Weyl and nodal-line topological semimetal. The theoretically calculated anomalous Hall conductivity (AHC) is in good agreement with the experimentally obtained AHC.

Secondly, we present a systematic investigation of the anomalous Hall effect (AHE) in a ferromagnetic Heusler compound Co_2CrGa using theoretical studies. First-principles calculations suggest that the Berry curvature, which originates from a gapped nodal line as well as Weyl nodes generated from the triple point near the E_F in the presence of spin-orbit coupling, is responsible for the observed large AHC in this compound.

1.8.3 Chapter4

In this chapter, we study the topological properties of the electronic band structure of a half-metallic ferromagnet Co_2FeSi employing the ab initio DFT method and show that it is a strongly correlated material. The experimentally observed magnetic properties can be explained in terms of the Slater-Pauling (SP) rule and our calculations are consistent with it. We also investigate the band topology of Co_2FeSi and find that there are three topological nodal lines at 380 meV above E_F. The degeneracy of these nodal lines is perturbed upon introducing spin-orbit coupling with magnetization along [001] direction. However, some points still preserve degeneracy and are identified as Weyl points, each associated with a specific Chern number. At the ambient pressure, the AHC properties of this material have only extrinsic contribution which is consistent with the experimental results. To make the AHC intrinsic, we tune the position of the nodal line close to the Fermi energy by applying the hydrostatic pressure up to 26 GPa. We also discuss crystal symmetries and their relation with nodal lines and Weyl points.

1.8.4 Chapter5

In this chapter we have studied electronic flat bands in momentum space, arising from the strong localization of electrons in real space, which are an ideal platform to realize strongly correlated phenomena. Flat bands can naturally arise in certain geometrically frustrated lattices, often with nontrivial topology in the presence of spin-orbit coupling. Here, we report the observation of topological flat bands in a frustrated topological ferromagnetic metal $MgMn_6Sn_6$, using DFT+U and DFT+DMFT calculations. Spin-orbit coupling opens a gap of 20 meV at the quadratic touching point between the Dirac and flat bands, endowing a nonzero Z_2 invariant to the flat band. The presence of 3d transition metal Mn in $MgMn_6Sn_6$ favour non-trivial topological features and novel quantum phases, including the saddle points, nodal lines, Weyl/Dirac fermions, and anomalous Hall effect. In addition, around the Brillouin zone centre, Z_2 nontrivial topological surface states are also observed due to band inversion mediated by strong spin-orbit coupling. Despite the presence of large incoherent scattering due to electronic interactions, these band crossings and flat band features persist at finite temperatures.

1.8.5 Chapter6

In this chapter, we have studied recently synthesized topological van der Waals (vdW) Fe_nGeTe_2 (n=3,4, and 5) series of compounds that have drawn a lot of research interest due to their interesting magnetic properties and anomalous transport behavior. However, understanding the topological aspect of these materials' electronic band structure is either scant or absent in the literature. In this work, we perform a comparative study of the electronic structure of all three materials to understand their topological properties and their effect on transport properties using the first-principles calculations and to derive the effective tight-binding model for these systems. All three systems exhibit ferromagnetic behavior, and the contribution of various Fe d-orbitals are also studied. Spin-orbit coupling (SOC) causes the degeneracy to be lifted and results in a finite Berry curvature

(BC). Finite BC contributes to the intrinsic anomalous Hall conductivity (AHC) and Nernst conductivity (ANC) of these systems. We show that Fe_3GeTe_2 and Fe_5GeTe_2 have similar nodal line formations, while Fe_4GeTe_2 exhibits nodal points close to Fermi energy E_F. We calculate AHC (σ_{xy}) at zero temperature and ANC (α_{xy}) at room temperature for n=3,4, and 5 and find that our values are consistent with transport and magnetic measurement.

1.8.6 Chapter7

In this chapter we have studied the combining ab initio and model Hamiltonian approaches, we delve into the electronic, magnetic, topological, and transport characteristics of the ferromagnetic double-perovskite system Ba_2CoWO_6. The itinerant carrier driven half-metallic ferromagnetism is attributed to a multi-orbital Hubbard-Kanamori Hamiltonian for the two transition metal (Co, W) elements. A higher value of electron density at t_{2g} orbitals of the Co site ($\langle n \rangle \sim 1.5$) leads to a lower magnetic moment which gets highly influenced by thermal and quantum fluctuations. Also, the incorporation of the W atom in the model Hamiltonian, albeit with its negligible charge density, is important to model the low enough Curie temperature (T_C) of this material. Notably, finite spin-orbit coupling (SOC) at the Co site induces nontrivial band topology near the conducting channel, particularly influencing the electronic structure close to the Fermi level. Along with DFT calculations, the intrinsic SOC effect within our model Hamiltonian describes anomalous Hall conductivity due to spin canting preserving the ferromagnetic order.

Chapter 2

Theoretical Frameworks

> Trying to understand the way nature works involves a most terrible test of human reasoning ability. It involves subtle trickery, beautiful tightropes of logic on which one has to walk in order not to make a mistake in predicting what will happen. The quantum mechanical and the relativity ideas are examples of this.— **Richard P.Feynman**

We will go over the theoretical underpinnings and ideas needed to analyse the electronic structures of diverse systems in this chapter. Density Functional Theory (DFT)[105] and model Hamiltonian are two distinct approaches have been applied in our work for electronic structure calculations, depending on the constraints of the topic under research. To comprehend the characteristics of the system's ground state and other excited states, we solve the Hamiltonian in both approaches. To lower the system's degrees of freedom, we must take into account a few logical assumptions as the complexity of the problem rises with the number of protons and electrons in the system. This aids in keeping the issue manageable given our computational constraints. So, I've begun by outlining how the many body Hamiltonian forms, and after that, we'll show the various assumptions and methods that are applied in order to solve it.

2.1 Many body Hamiltonian

The fundamental building block of all materials, regardless of their configuration, is the atom, which is composed of charge-less neutrons, negatively charged electrons, and positively charged protons. The electronic structure and various properties found in different materials are caused by the electrostatic Coulomb interactions between these charged particles that are present in the atoms. The non-relativistic time-independent many body Schrödinger equation, $\mathrm{H}\Psi = \mathrm{E}\Psi$, where H is the many body Hamiltonian, Ψ is the set of energy eigenstates, and E is the set of energy eigenvalues, can be used to describe this problem of interacting charged particles in a quantum mechanical framework.

The many body Hamiltonian can now be expressed as

$$H = -\frac{\hbar^2}{2M_I}\sum_I \nabla_I^2 - \frac{\hbar^2}{2m_e}\sum_i \nabla_i^2 + \frac{1}{2}\sum_{I,J(I\neq J)} \frac{Z_I Z_J e^2}{|\mathbf{R}_I - \mathbf{R}_J|} + \frac{1}{2}\sum_{i,j(i\neq j)} \frac{e^2}{|\mathbf{r}_i - \mathbf{r}_j|} - \sum_{i,I} \frac{Z_I e^2}{|\mathbf{R}_I - \mathbf{r}_i|} \tag{2.1}$$

In this Hamiltonian, r_i indicates the positions of the i^{th} electron, whereas M_I and R_I stand for the mass and location of the I^{th} nucleus, respectively. m_e and e stand for the electron's mass and charge, respectively. $\mathrm{Z}_I\mathrm{e}$ is the I^{th} nuclei's charge. ∇_i^2 and ∇_I^2 are the Laplacian operators that hold second-order derivatives concerning the electronic coordinates and the nuclei, respectively. The reduced Plank's constant is denoted by $\hbar$. The kinetic energy of the nuclei and electrons, respectively, are represented by the first two terms in the Hamiltonian. The third term to the repulsive Coulomb interaction between the nuclei and the fourth term relates to the Coulomb repulsion between the electrons. The potential energy resulting from the attractive Coulomb interaction between the electrons and nuclei is shown by the last term in the Hamiltonian.

At this point, the compact version of the Hamiltonian of equation 2.1 is expressed as

$$H = T_N(\mathbf{R}) + T_e(\mathbf{r}) + V_{NN}(\mathbf{R}) + V_{ee}(\mathbf{r}) + V_{eN}(\mathbf{r},\mathbf{R}) \tag{2.2}$$

The many body Schrödinger equation can be solved to find all of the material's properties. However, because of the enormous number of linked coordinates involved, this problem is extremely difficult to solve within a full quantum-mechanical framework. A full analytical solution is accessible for only a few cases, and the numerical solutions are limited to a relatively small number of particles. Thus, in order to solve this coupled many-body Hamiltonian, two basic approaches are taken into consideration:

a) The many body wave function is decoupled and therefore solvable in our computational limits by using techniques like Hartree[106], Hartree-Fock [**?**], Density Functional Theory (DFT)[105, 107], etc. In light of the debut of some reasonable approximations like the Born-Oppenheimer Approximation[108], Independent electron approximation, etc.

b) Utilization of a model Hamiltonian that only includes the dominating interactions and the important single particle orbitals that are crucial in identifying the particular attribute under study for the electronic portion of the whole many-body Hamiltonian. These models, which are solved using numerical approaches like the exact diagonalization (ED) method, include the Tight Binding Model, Hubbard Model, Heisenberg Model, Configuration Interaction (CI) Methods, etc.

The Born-Oppenheimer Approximation will be further discussed in the upcoming sections, along with the many strategies and tactics I employed in my thesis work to solve the many body Schrödinger equation.

2.2 Born-Oppenheimer Approximation

One of the most popular mathematical approximations in quantum physics, the Born-Oppenheimer (BO) Approximation[108] is named after J. Robert Oppenheimer and Max Born. This assumption stems from the fact that nucleons are assumed to be significantly slower than electrons because their mass is approximately 1800 times heavier than that of an electron. As a result, with relation

to the electrons' motion, the nucleus may be regarded as stationary. In order to tackle nuclear and electronic issues separately, this enables us to separate the nuclear and electronic degrees of freedom. It is possible to rewrite equation 2.2's many body Hamiltonian as

$$H = H_{\text{nuclear}} + H_{\text{electronic}} = [T_N(\mathbf{R}) + T_e(\mathbf{r}) + V_{NN}(\mathbf{R}) + V_{ee}(\mathbf{r}) + V_{eN}(\mathbf{r},\mathbf{R})] \quad (2.3)$$

Since the nuclei are thought to be fixed in relation to the electron's motion, we now eliminate the kinetic energy term of the nuclei (K_N) within this adiabatic approximation. It is also believed that the potential energy resulting from nuclear-nuclear interaction is a constant. Medelung energy[109] is the name given to this constant nuclear potential energy V_{eN}, and it is estimated classically. As a result, following the Born-Oppenheimer Approximation, the Hamiltonian only includes the electronic component and becomes

$$H^{ele}_{\text{BOA}} = T_e(\mathbf{r}) + V_{NN}(\mathbf{R}) + V_{ee}(\mathbf{r}) + V_{eN}(\mathbf{r},\mathbf{R}) \quad (2.4)$$

The electronic portion of the many-body Schrödinger equation can be solved to yield the electrons' energy eigenstates, which are explicit functions of the electron coordinates and in which the coordinates of the nucleus only appear as parameters.

2.3 Independent Electron Approximation

The many body Hamiltonian is still a many electron Hamiltonian even though the BO approximation separates the electronic and nuclear parts of the Hamiltonian and makes the problem less complex. It is also challenging to solve since the electron-electron interaction term V_{ee} causes the electron degrees of freedom to be coupled. In order to turn the interacting electron problem into a non-interacting electron problem, more assumptions are made. We suppose that an astute selection of the periodic potential V(r) can manage the electron-electron interactions in this Independent Electron Approximation. Here, the interacting electron system is

essentially projected into an independent electron system that is travelling under an effective potential V (r) because of the remaining electrons in the system. Two distinct ways have been proposed to accomplish this: i) A wave function-based strategy that includes the Hartree[106] and Hartree Fock methods[110]; and ii) Density functional theory [105, 107].

Density Functional Theory is preferred because it is computationally tractable even for complex and extended systems, whereas wave function-based approaches have the drawback of being computationally expensive even for small system sizes and losing that tractability as system sizes increase. The Density Functional Theory, which is employed in my thesis work and is implemented within the Vienna ab initio simulation program (VASP)[111–113] to explore the electronic structure of the materials, will be illustrated in the next part.

2.4 Density Functional Theory (DFT)

The Thomas-Fermi (TF) theory was first proposed by Thomas and Fermi in 1927 and provides a method for determining the electronic structure based on electron density[113]. Unfortunately, this theory could not support the bound states because of significant errors in the exchange energy and estimates made for the electron's kinetic energy. Ultimately, a correct formalism based on electron density was introduced by Hohenberg and Kohn in 1964 to solve the N-electron Hamiltonian and provide a good description of the system's ground state features. The density functional theory (DFT) was the name given to this formalism[105].In this theory, the variable electron density is included to lower the number of degrees of freedom and the complexity of the problem. It estimates the probability of finding an electron near an atom or molecule in a specific area. This physical quantity is experimentally measurable using the X-ray diffraction method[114]. The main idea behind this theory was to use the electron density $\rho(r)$(just a function of 3 spatial variables), which is a function of only three spatial variables, as a fundamental variable in place of the N-electron wave function $\Psi(\mathbf{r}_1, \ldots, \mathbf{r}_N)$, which

is a function of 3N number of variables. The normalised N-electron wave function yields the non-spin single-particle density for an N-electron system, which is expressed as

$$\rho(r_i) = N \int \Psi^*(\mathbf{r}_1, \ldots, \mathbf{r}_i, \ldots, \mathbf{r}_N)\Psi(\mathbf{r}_1, \ldots, \mathbf{r}_i, \ldots, \mathbf{r}_N)\, \mathrm{d}\mathbf{r}_1\, \mathrm{d}\mathbf{r}_2 \ldots \mathrm{d}\mathbf{r}_{(i-1)}\, \mathrm{d}\mathbf{r}_{(i+1)} \ldots \mathrm{d}\mathbf{r}_N \tag{2.5}$$

The single particle density integrates with the total number of electrons in the system and is only dependent on 3 spatial variables, i.e.

$$\int \rho(\mathbf{r}_i)\, \mathrm{d}\mathbf{r}_i = N \tag{2.6}$$

In the same way, two-particle densities can be defined as

$$\rho(\mathbf{r}_i, \mathbf{r}_j) = N(N-1) \int \Psi^*(\mathbf{r}_1, \ldots, \mathbf{r}_i, \ldots, \mathbf{r}_j, \ldots, \mathbf{r}_N)\Psi(\mathbf{r}_1, \ldots, \mathbf{r}_i, \ldots, \mathbf{r}_j, \ldots, \mathbf{r}_N) \\ \mathrm{d}\mathbf{r}_1\, \mathrm{d}\mathbf{r}_2 \ldots \mathrm{d}\mathbf{r}_{(i-1)}\, \mathrm{d}\mathbf{r}_{(i+1)} \ldots \mathrm{d}\mathbf{r}_{(j-1)}\, \mathrm{d}\mathbf{r}_{(j+1)} \ldots \mathrm{d}\mathbf{r}_N \tag{2.7}$$

The probability that an electron will be located at position $\mathbf{r}_i$ in the presence of another electron at position $\mathbf{r}_j$ is the definition of this two-particle density. If there is no correlation at all between the two electrons in the system, $\rho(\mathbf{r}_i, \mathbf{r}_j)$ can be obtained by multiplying the two single-particle densities:

$$\rho(\mathbf{r}_i, \mathbf{r}_j) = \rho(\mathbf{r}_i)\rho(\mathbf{r}_j) \tag{2.8}$$

However, because electrons in real physical systems are correlated, this two-particle density is given as

$$\rho(\mathbf{r}_i, \mathbf{r}_j) = \rho(\mathbf{r}_i)\rho(\mathbf{r}_j)\Delta\rho(\mathbf{r}_i, \mathbf{r}_j) \tag{2.9}$$

where the correlation term, $\Delta\rho(\mathbf{r}_i, \mathbf{r}_j)$, is an extremely important term in the density functional theory. These electron densities now contain an enormous amount of system-related information. More specifically, every one of the many-electron

system's ground state characteristics might be represented as a function of its ground state electron density distribution.

Hohenberg and Kohn's two mathematical theorems[115] served as the two main tenets of this density functional theory and a collection of formulas produced by Sham and Kohn[116].

2.4.1 The Hohenberg-Kohn Theorems

Theorem I Statement: The ground state electron density $\rho(\mathbf{r})$ uniquely specifies the potential $\mathrm{V}_{ext}(\mathbf{r})$ for any system of interacting or non-interacting electrons in any external potential $\mathrm{V}_{ext}(\mathbf{r})$[115, 117].

Proof: According to this theorem, the ground state electron density $\rho(\mathbf{r})$ of the system and the external potential $\mathrm{V}_{ext}(\mathbf{r})$ always correspond one to one. The system's electronic Hamiltonian can now be expressed as $\mathrm{H}_{ele} = \mathrm{K}_e + \mathrm{V}_{ee} + \mathrm{V}_{ext}$ using equation 2.4, where K_e and V_{ee} stand for the kinetic energy and electron-electron interaction energy, respectively. Assume that there is a difference greater than an additive constant between our two external potentials, $\mathrm{V}_A(\mathrm{r})$ and $\mathrm{V}_B(\mathrm{r})$. Let Ψ_A and Ψ_B be the respective ground state wavefunctions, and let H_A and H_B be the corresponding Hamiltonians. Therefore, $H_A\Psi_A = E_A\Psi_A$ and $H_B\Psi_B = E_B\Psi_B$, where E_A and E_B stand for the respective energies of the system, are two possible ways to write the Schrödinger equations.

Let us now assume that the ground state electron density $\rho(\mathbf{r})$ is produced by these two external potentials, $\mathrm{V}_A(\mathbf{r})$ and $\mathrm{V}_B(\mathbf{r})$. Now, the energies can be stated as

$$E_A = \langle \Psi_A | H_A | \Psi_A \rangle \tag{2.10}$$

$$E_B = \langle \Psi_B | H_B | \Psi_B \rangle \tag{2.11}$$

we can also write

$$\langle \Psi_B | H_B | \Psi_B \rangle = \langle \Psi_B | H_B | \Psi_B \rangle + \langle \Psi_B | [H_A - H_B] | \Psi_B \rangle \tag{2.12}$$

Now, we may always express the inequality since the wave function Ψ_B does not belong to the ground state of H_A.

$$E_A > \langle \Psi_B | H_A | \Psi_B \rangle \tag{2.13}$$

$$i.e. E_A > \langle \Psi_B | H_B | \Psi_B \rangle + \langle \Psi_B | [H_A - H_B] | \Psi_B \rangle \tag{2.14}$$

$$i.e. E_A > E_B + \langle \Psi_B | [H_A - H_B] | \Psi_B \rangle \tag{2.15}$$

$$i.e. E_A > E_B + \langle \Psi_B | [V_A(\mathbf{r}) - V_B(\mathbf{r})] | \Psi_B \rangle \tag{2.16}$$

Likewise, we can obtain an expression for E_B.

$$E_B > E_A + \langle \Psi_A | [V_B(\mathbf{r}) - V_A(\mathbf{r})] | \Psi_B \rangle \tag{2.17}$$

Adding equation 2.16 and equation 2.17 we get

$$E_A + E_B > E_B + E_A + \langle \Psi_B | [V_A(\mathbf{r}) - V_B(\mathbf{r})] | \Psi_B \rangle + \langle \Psi_A | [V_B(\mathbf{r}) - V_A(\mathbf{r})] | \Psi_A \rangle \tag{2.18}$$

$$E_A + E_B > E_B + E_A + \langle \Psi_B | [V_A(r) - V_B(r)] | \Psi_B \rangle - \langle \Psi_A | [V_A(r) - V_B(r)] | \Psi_A \rangle \tag{2.19}$$

Given that both $V_A(\mathbf{r})$ and $V_B(\mathbf{r})$ lead to the same ground state electron density $\rho(\mathbf{r})$, the equation above can be expressed as

$$E_A + E_B > E_B + E_A + \int \rho(\mathbf{r})[V_A(\mathbf{r}) - V_B(\mathbf{r})] \, \mathrm{d}^3 r - \int \rho(\mathbf{r})[V_A(\mathbf{r}) - V_B(\mathbf{r})] \, \mathrm{d}^3 r \tag{2.20}$$

which leads to

$$E_A + E_B > E_B + E_A \tag{2.21}$$

This discrepancy disproves our original theory that the same ground state density can arise from two distinct external potentials. This suggests that the external potential (apart from an additive constant) is uniquely determined by the ground state density.

Theorem II

Statement: A multi-electron system's energy can be expressed as E[$\rho(\mathbf{r})$], the universal functional form of the charge density. The global minimum of this functional, which is determined by the variational principle, is the system's ground state energy. The ground state charge density is the charge density that relates to the lowest energy.

The total energy functional for a system of N electrons, represented by the Hamiltonian $H = T_e + V_{ee} + V_{ext}$, can be expressed as a function of density $\rho(\mathbf{r})$:

$$E[\rho(\mathbf{r})] = \langle \Psi | H | \Psi \rangle \tag{2.22}$$

$$E[\rho(\mathbf{r})] = \int \rho(\mathbf{r})[T_e + V_{ee} + V_{ext}](\mathbf{r})\, d^3r \tag{2.23}$$

$$E[\rho(\mathbf{r})] = T[\rho(\mathbf{r})] + E_{ee}[\rho(\mathbf{r})] + \int \rho(\mathbf{r}) V_{ext}(\mathbf{r})\, d^3r \tag{2.24}$$

The kinetic energy term in this case is T[$\rho(\mathbf{r})$], and the electron-electron interaction term is E_{ee} [$\rho(r\mathbf{r})$]. The combination of these two terms is known as the Hohenberg-Kohn functional F[$\rho(\mathbf{r})$], i.e.

$$F[\rho(\mathbf{r})] = T[\rho(\mathbf{r})] + E_{ee}[\rho(\mathbf{r})] \tag{2.25}$$

Consequently, the equation above has the form

$$E[\rho(\mathbf{r})] = F[\rho(\mathbf{r})] + \int \rho(\mathbf{r}) V_{\mathrm{ext}}(\mathbf{r})\, d^3r \tag{2.26}$$

It is now possible to uniquely calculate the ground state energy $E_0[\rho(\mathbf{r})]$ of the many-electron system by computing the global minimum of this energy functional $E[\rho(\mathbf{r})]$, which corresponds to a unique V_{ext}. The ground state charge density ($\rho_0(\mathbf{r})$) of the system is defined as the electron density that corresponds to the least energy ($E[\rho(\mathbf{r})]$). Thus, we can state that the following inequality holds for any other electron density $\rho_0'(\mathbf{r})$.

$$E[\rho'(\mathbf{r})] \geq E[\rho(\mathbf{r})] \tag{2.27}$$

2.4.2 Kohn-Sham Formulation

Since the Hohenberg-Kohn functional's form is unknown, determining the ground state energy of any interacting N-electron system is challenging. A formalism that provides a good approximation of the Hohenberg-Kohn functional $F[\rho(\mathbf{r})]$ was proposed by Kohn and Sham[116] in 1965.

Initially, the energy functional's electron-electron term is expressed as follows:

$$E_{ee}[\rho(\mathbf{r})] = \frac{e^2}{2} \int \int \frac{\rho(\mathbf{r}_i, \mathbf{r}_j)}{|\mathbf{r}_i - \mathbf{r}_j|} \, d\mathbf{r}_i \, d\mathbf{r}_j \tag{2.28}$$

where the two-particle density, denoted by $\rho(\mathbf{r}_i, \mathbf{r}_j)$, takes the following form (from equation 2.9) for an interacting electron system:

$$\rho(\mathbf{r}_i, \mathbf{r}_j) = \rho(\mathbf{r}_i)\rho(\mathbf{r}_j)\Delta\rho(\mathbf{r}_i, \mathbf{r}_j) \tag{2.29}$$

With the use of the decomposition, the equation above may be expressed as

$$\rho(\mathbf{r}_i, \mathbf{r}_j) = \rho(\mathbf{r}_i)\rho(\mathbf{r}_j)[1 - f(\mathbf{r}_i, \mathbf{r}_j)] \tag{2.30}$$

where $\Delta\rho(\mathbf{r}_i, \mathbf{r}_j) = [1 - f(\mathbf{r}_i, \mathbf{r}_j)]$ and $f(\mathbf{r}_i, \mathbf{r}_j)$ s the correlation function. Therefore, equation 2.28 can be rewritten as:

$$E_{ee}[\rho(\mathbf{r})] = \frac{e^2}{2} \int\int \frac{\rho(\mathbf{r}_i)\rho(\mathbf{r}_j)}{|\mathbf{r}_i - \mathbf{r}_j|}\, d\mathbf{r}_i\, d\mathbf{r}_j + \frac{e^2}{2} \int\int \frac{\rho(\mathbf{r}_i)\rho(\mathbf{r}_j) f(\mathbf{r}_i, \mathbf{r}_j)}{|\mathbf{r}_i - \mathbf{r}_j|}\, d\mathbf{r}_i\, d\mathbf{r}_j \quad (2.31)$$

which, in a concise form, may be expressed as:

$$E_{ee}[\rho(\mathbf{r})] = E_H[\rho(\mathbf{r})] + \Delta E_{ee} \quad (2.32)$$

where

$$E_H[\rho(r)] = \frac{e^2}{2} \int\int \frac{\rho(\mathbf{r}_i)\rho(\mathbf{r}_j)}{|\mathbf{r}_i - \mathbf{r}_j|}\, d\mathbf{r}_i\, d\mathbf{r}_j \quad (2.33)$$

and

$$\Delta E_{ee} = \frac{e^2}{2} \int\int \frac{\rho(\mathbf{r}_i)\rho(\mathbf{r}_j) f(\mathbf{r}_i, \mathbf{r}_j)}{|\mathbf{r}_i - \mathbf{r}_j|}\, d\mathbf{r}_i\, d\mathbf{r}_j \quad (2.34)$$

The Hartee energy, or classical electron-electron Coulomb interaction term, is denoted as $\mathrm{E}_H[\rho(\mathbf{r})]$ in this context. The correlation term between electrons is denoted by ΔE_{ee}.

Now, the existence of the Laplacian operator (derivative term) renders addressing the kinetic energy component T $[\rho(\mathbf{r})]$ in the energy functional exceedingly challenging. The charge density of the N-electron interacting system was substituted, for the sake of simplification, with the charge density of the N-electron hypothetical non-interacting system, which is given by

$$\rho(\mathbf{r}) = 2 \sum_{i=1}^{N} \phi_i^*(\mathbf{r})\phi_i(\mathbf{r}) \quad (2.35)$$

where ϕ_i, also known as the Kohn-Sham orbitals, is the non-interacting single electron wave function. The reason for the multiplication factor of 2 is that spin degrees of freedom have been included in this. Using these Kohn-Sham orbitals,

the kinetic energy of this non-interacting N-electron system can be expressed as

$$T_0[\rho(\mathbf{r})] = \sum_{i=1}^{N} \langle \phi_i(\mathbf{r})| - \frac{\hbar^2}{2m_e} \sum_{i=1}^{N} \nabla^2 |\phi_i(\mathbf{r})\rangle \tag{2.36}$$

The kinetic energy of the real system is not provided by the Kohn-Sham orbitals, which are entirely mathematical. Thus, the actual system's kinetic energy can be written as

$$T[\rho(\mathbf{r})] = T_0[\rho(\mathbf{r})] + \Delta T_{ee} \tag{2.37}$$

where the electron-electron correlation gives rise to the kinetic energy term, ΔT_{ee}. Now, substituting E_{ee} $[\rho(\mathbf{r})]$ from equation 2.32 and T ($[\rho(\mathbf{r})]$ from equation 2.37 in equation 2.25 we get

$$F[\rho(\mathbf{r})] = T_0[\rho(\mathbf{r})] + \Delta T_{ee} + E_H[\rho(\mathbf{r})] + \Delta E_{ee} \tag{2.38}$$

In the equation mentioned earlier, the terms ΔT_{ee} and ΔE_{ee} originate from electron-electron correlation and are combined into a single quantity, $E_{XC}[\rho(\mathbf{r})]$, i.e.

$$E_{XC}[\rho(\mathbf{r})] = \Delta T_{ee} + \Delta E_{ee} \tag{2.39}$$

Thus, equation 2.38 is transformed into

$$F[\rho(\mathbf{r})] = T_0[\rho(\mathbf{r})] + E_H[\rho(\mathbf{r})] + E_{XC}[\rho(\mathbf{r})] \tag{2.40}$$

Now, the global minimum of the energy functional $\mathrm{E}[\rho(\mathbf{r})]$ given in equation 2.26 can be used to determine the ground state energy of the system. The Euler equation is obtained by subjecting this minimization to the constraint that the total number of electrons N is conserved (i.e.,$\int \rho(\rho(\mathbf{r}))\, dr = N$).

$$\frac{\delta}{\delta\rho(\rho(\mathbf{r}))}[F[\rho(\mathbf{r})] + \int \rho(\mathbf{r}) V_{\text{ext}}(\mathbf{r})\, d^3r - \mu_L(\int \rho(\mathbf{r})\, d^3r - N)] = 0 \tag{2.41}$$

where the Lagrange Multiplier connected to the restriction of conserved total electron number is denoted by μ_L. The formula above comes down to

$$\mu_L = \frac{\delta F[\rho(\mathbf{r})]}{\delta \rho(\mathbf{r})} + V_{\text{ext}}(\mathbf{r}) \tag{2.42}$$

In the equation above, substituting F[n(**r**)] from equation 2.40 yields

$$\mu_L = \frac{\delta \left(T_0[\rho(\mathbf{r})] + E_H[\rho(\mathbf{r})] + E_{XC}[\rho(\mathbf{r})] \right)}{\delta n(\mathbf{r})} + V_{\text{ext}}(\mathbf{r}) \tag{2.43}$$

$$= \frac{\delta T_0[\rho(\mathbf{r})]}{\delta \rho(\mathbf{r})} + \frac{\delta E_H[n(\mathbf{r})]}{\delta \rho(\mathbf{r})} + \frac{\delta E_{XC}[\rho(\mathbf{r})]}{\delta n(\mathbf{r})} + V_{\text{ext}}(\mathbf{r}) \tag{2.44}$$

The above equation can be rewritten as

$$\mu_L = \frac{\delta T_0[\rho(\mathbf{r})]}{\delta \rho(\mathbf{r})} + + V_H(\mathbf{r}) + V_{XC}(\mathbf{r}) + V_{\text{ext}}(\mathbf{r}) \tag{2.45}$$

where $V_H(r) = \frac{\delta E_H(\mathbf{r})}{\delta \rho(\mathbf{r})}$ and $V_{XC}(\mathbf{r}) = \frac{\delta E_{XC}(\mathbf{r})}{\delta \rho(\mathbf{r})}$. Returning to equation 2.41, the self-consistent Kohn-Sham equation is as follows once the total energy functional is minimised using the variational principle:

$$\left[-\frac{\hbar^2}{2m} \nabla^2 + V_H(\mathbf{r}) + V_{XC}(\mathbf{r}) + V_{\text{ext}}(\mathbf{r}) \right] \phi_i(\mathbf{r}) = \epsilon_i \phi_i(\mathbf{r}) \tag{2.46}$$

The form of $V_{XC}(\mathbf{r})$ in the equation above is unknown. The Kohn Sham potential $V_{KS}(\mathbf{r})$ refers to the combination of the three potentials $V_H[\rho(\mathbf{r})]$, $V_{XC}[\rho(\mathbf{r})]$, and $V_{\text{ext}}[\rho(\mathbf{r})]$. Thus, the Khon-Sham equation has the following form:

$$\left[-\frac{\hbar^2}{2m} \nabla^2 + V_{KS}(\mathbf{r}) \right] \phi_i(\mathbf{r}) = \epsilon_i \phi_i(\mathbf{r}) \tag{2.47}$$

It is crucial to keep in mind that the Kohn-Sham orbitals ($\phi_i(\mathbf{r})$) and energy eigenvalues (ξ_i) are not actual electron wave functions or electron energies; rather,

they are entirely mathematical constructs with no physical significance. The only ground state electron density that is an exact match is the one that can be calculated by solving the Kohn-Sham equations for the single electron. The Kohn-Sham Hamiltonian's dependence on density, which in turn depends on the same Hamiltonian's eigenfunction, is another crucial point. As a result, we are having trouble being consistent here. Thus, the following procedures are used to solve the Kohn-Sham equation iteratively[118]:

Step 1 : To start with, choose a trial electron density,$\rho(\mathbf{r})$

Step 2 : Compute the Kohn-Sham potential($V_{KS}[\rho(\mathbf{r})]$ using this starting electron density.Next, to determine the single particle wave functionsϕ_i, solve the Kohn-Sham equations with the proper boundary conditions.

Step 3 : Determine the electron density $\rho_{\mathrm{KS}}(\mathbf{r}) = 2\sum_{i=1}\phi_i^{\star}(\mathbf{r})\phi_i(\mathbf{r})$ by using the single particle wave function that was acquired in the preceding step.

Step 4 : Examine the electron density that was determined in the previous step,$\rho_{\mathrm{KS}}(\mathbf{r})$ with the initial trial electron density,$\rho(\mathbf{r})$. This converged electron density is the ground state electron density if the two electron densities are consistent and meet certain predetermined convergence requirements. If not, we update the density of electrons $\rho_{\mathrm{KS}}(\mathbf{r})$ ln in some manner, return to step 2 and repeat the following procedures.

Figure 2.1 provides a visual representation of how the Kohn-Sham equation is solved.

2.4.3 Approximations For Exchange Correlation Functional

Local Density Approximation(LDA):

Hohenberg and Kohn introduced the Local Density Approximation (LDA) in their DFT work[105] in 1965. As the name suggests, this is the most basic approximation in which the exchange-correlation energy per particle solely depends on the local density. Here, the exchange correlation energy Homogeneous Electron Gas (HEG), which corresponds to the electron density at that specific place in space, approximates the genuine exchange-correlation energy at any given point in space. For this homogeneous electron gas, the exchange-correlation energy can be exactly determined, and the total exchange-correlation energy of the system, under the

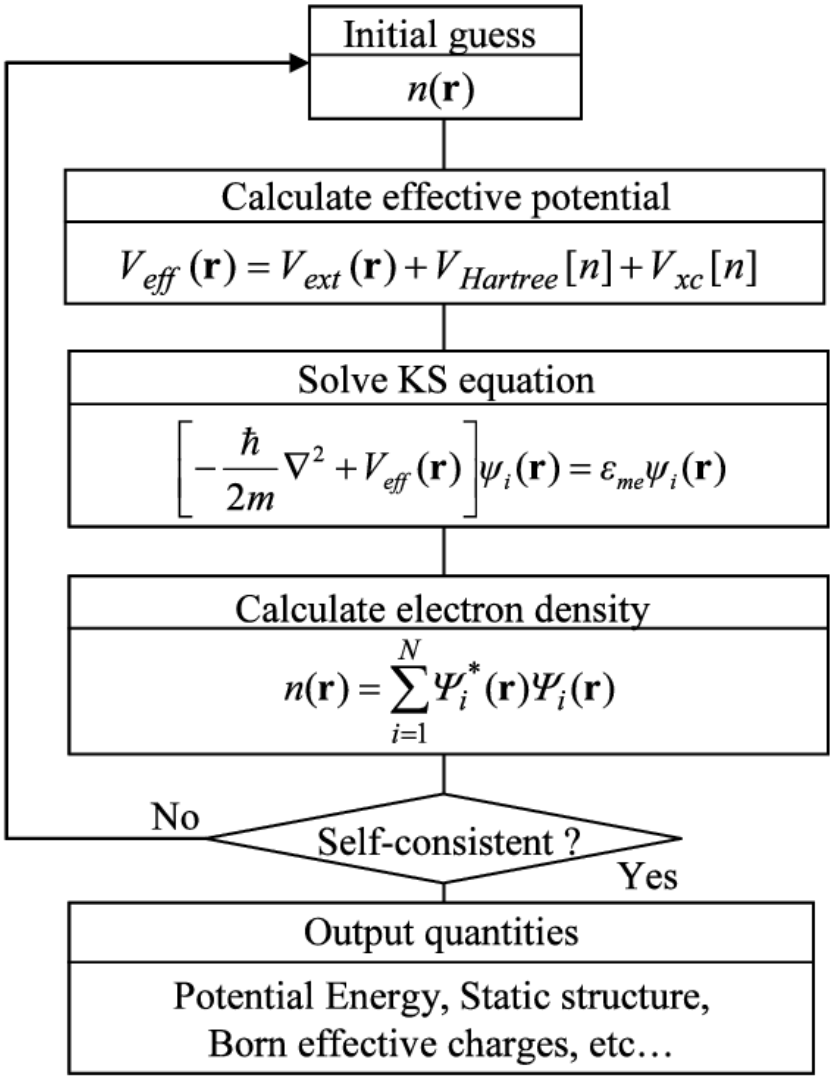

FIGURE 2.1: Flowchart of DFT

local density approximation, has the following form

$$E_{XC}^{LDA}[\rho(\mathbf{r})] = \int \rho(\mathbf{r})\varepsilon_{XC}^{HEG}[\rho(\mathbf{r})d^3r \tag{2.48}$$

In a homogeneous electron gas, $\epsilon_{XC}^{HEG}[\rho(\mathbf{r})]$ represents the exchange-correlation energy per electron, which corresponds to the electron density $\rho(\mathbf{r})$.It is possible to divide this $\epsilon_{XC}^{HEG}[\rho(\mathbf{r})]$ into independent exchange and correlation components.

$$\epsilon_{XC}^{HEG}[\rho(\mathbf{r})] = \epsilon_{X}^{HEG}[\rho(\mathbf{r})] + \epsilon_{C}^{HEG}[\rho(\mathbf{r})] \tag{2.49}$$

In the above equation, the exchange energy per electron, or $\epsilon_{XC}^{HEG}[\rho(\mathbf{r})]$, was analytically determined for HEG by Dirac [20] and bears the following form.

$$\epsilon_{X}^{HEG}[\rho(\mathbf{r})] = -\frac{3e^2}{4}\sqrt[3]{\frac{3\rho(\mathbf{r})}{\pi}} \tag{2.50}$$

and For the HEG, the correlation energy per electron is denoted by $\epsilon_{C}^{HEG}[\rho(\mathbf{r})]$. Only in the cases of low density[119] and high density[120, 121], which correspond to the limit of infinitely weak or indefinitely strong correlation, can this be derived analytically. For each density, the analytical HEG form of $\epsilon_{C}^{HEG}[\rho(\mathbf{r})]$ is provided as follows:

$$\epsilon_{C}^{\text{low}}[\rho(\mathbf{r})] = \frac{1}{2}[\frac{a_1}{r_s} + \frac{a_2}{r_s^{\frac{3}{2}}} + ...] \tag{2.51}$$

$$\epsilon_{C}^{\text{high}}[\rho(\mathbf{r})] = A_1 + A_2 r_s + (A_3 + A_4 r_s)\ln(r_s) \tag{2.52}$$

The Wigner-Seitz cell's radius, r_s, depends on the electron density in this case as

$$\frac{4}{3}\pi r_s^3 = \frac{1}{\rho(\mathbf{r})} \tag{2.53}$$

Quantum Monte Carlo (QMC) calculation can be used to calculate the correlation energy density value $\epsilon_{C}^{HEG}[\rho(\mathbf{r})]$ for intermediate electron density. Popular techniques like Vosko-Wilk-Nusair (VWN)[122], Perdew-Zunnger (PZ81)[123], Cole-Perdew (CP)[124], Perdew-Wang (PW92)[125], etc. are included in this framework

and use various functional forms of the correlation energy in the LDA correlation potential. Nonetheless, as the correlation and exchange energy densities solely rely on the local density, LDA is appropriate for gradually changing densities. Additionally, it is discovered that LDA tends to overestimate cohesive and binding energies while underestimating the lattice parameter and solids' band gaps.

Generalized Gradient Approximation (GGA) :

Since LDA cannot adequately explain real systems in which the production of spatially directed connections causes electron density to change non-uniformly, it is not a very plausible approximation. It was required to improve the approximation of the exchange correlation functional in order to account for the inhomogeneity of the charge density. As a result, the Generalised Gradient Approximation (GGA) was proposed, in which the local density and the gradient of the electron density both influence the exchange-correlation energy density. The exchange correlation energy is stated as under this approximation:

$$E_{XC}^{GGA}[\rho(\mathbf{r})] = \int \rho(\mathbf{r})\epsilon_{XC}^{\mathrm{HEG}}[\rho(\mathbf{r}), |\nabla\rho(\mathbf{r})|]\, d^3r \tag{2.54}$$

Currently, there are several GGA functionals, including Perdew and Wang [27], Becke-Lee-Yang-Parr (BLYP)[126], and Perdew, Burke and Ernzerhof (PBE)[127], depending on the functional form of $\epsilon_{XC}[\rho(\mathbf{r}), |\nabla\rho(\mathbf{r})|]$ that is selected. Even though GGA provides a more accurate representation of total energies, structural energy difference, and atomization energies[127], it occasionally overcorrects the LDA approximation. In general, GGA outperforms LDA for systems with significant correlations.

Hybrid Functionals :

Another often used approximation for the exchange-correlation functional is the hybrid functional. It includes the remainder of the exchange-correlation energy from other ab initio potentials (LDA or GGA functionals) plus a portion of the exchange correlation energy from Hartree-Fock theory. Heyd-Scuseria-Ernzerhof

(HSE)[111], PBE0[127], "Becke, 3-parameter, Lee-Yang-Parr" (B3LYP)[128], and other hybrid functionals are a few that are frequently employed.

The most well-known hybrid functional, called after J. Heyd, G. E. Scuseria, and M. Ernzerhof, is the HSE hybrid functional[111]. This considers the impact of the exchange functional on the screened Coulomb potential. The HSE hybrid functional has the following form:

$$E_{XC}^{HSE} = \alpha E_X^{HF,SR} + (1-\alpha)E_X^{PBE,SR}(w) + E_X^{PBE,LR}(w) + E_C^{PBE} \tag{2.55}$$

where α is the mixing parameter. The short-range Hartree Fock exchange potential is denoted by $E_{XC}^{HF,SR}$, whereas the short-range and long-range PBE exchange potentials are represented by $E_X^{PBE,SR}$ and $E_X^{PBE,LR}$, respectively, and the PBE correlation energy is represented by E_C^{PBE}. The hybrid functional's Hartee-Fock exchange (HF) is now non-local in nature. Understanding the value of the Kohn-Sham orbitals ϕ_i at every location in space is necessary to determine its value at any given position. The hybrid functionals are computationally costly as a result. Despite this, their popularity originates from their propensity to outperform LDA or GGA in highly correlated systems.

2.5 Numerical Approximations for DFT Calculations

The Kohn-Sham equations are numerically solved in an iterative fashion to obtain the ground state electron density, which is necessary in order to accurately evaluate the electronic structure and other physical aspects of any many-electron system. Since the exchange-correlation potential's precise functional form is unknown, several numerical approximations have been proposed in an attempt to determine its appropriate form. For instance, infinite sums are trimmed to finite ones, integrations are performed with a finite number of grid points, etc. As a result, it introduced some inaccuracy into the computations, and the converged

solution that DFT provides is not the precise solution but rather one that is quite near to it. Some of these numerical assumptions used in the DFT computation will be covered in this section.

2.5.1 Plane Wave Basis and Cut-off Energy

We must choose a suitable set of basis functions in order to solve the single electron Kohn-Sham equation computationally. Because of the periodic arrangement of atoms, electrons in crystalline materials move in a periodic potential. potential can be increased in term of periodic Blöch states[129] represented as the single particle wave functions for non-interacting electrons (Kohn-Sham orbitals) in such periodic potential as

$$\phi_i(\mathbf{r}) = e^{i\mathbf{k}\cdot\mathbf{r}} u_i(\mathbf{r}) \tag{2.56}$$

In this case, the function $u_i(\mathbf{r})$ has the translational periodicity of the Bravais lattice, that is, $u_i(\mathbf{r}+\mathbf{T}) = u_i(\mathbf{r})$, where T is the real-space translation vector, denoted as $T = n_1\mathbf{a_1} + n_2\mathbf{a_2} + n_3\mathbf{a_3}$, where $\mathbf{a_1}$, $\mathbf{a_2}$, and $\mathbf{a_3}$ are the lattice vectors in real space and n_1, n_2, and n_3 are integers. Now, using the Bloch theorem, we may extend $u_i(\mathbf{r})$ in terms of plane waves (Fourier Expansion), which is given as

$$u_i(\mathbf{r}) = \sum_{\mathbf{G}} C_G e^{i\mathbf{G}\cdot\mathbf{r}} \tag{2.57}$$

he reciprocal lattice vector, $\mathbf{G}$, is defined in terms of reciprocal space unit vectors as $\mathbf{G} = m_1\mathbf{a_1} + m_2\mathbf{a_2} + m_3\mathbf{a_3}$. where b_1, b_2, and b_3 are the lattice vectors in reciprocal space and m_1, m_2, and m_3 are integers. Equation 2.56 can therefore be expressed as follows:

$$\phi_i(r) = \sum_{\mathbf{G}} C_{\mathbf{G}+\mathbf{k}} e^{i(\mathbf{G}+\mathbf{k})\cdot\mathbf{r}} \tag{2.58}$$

The infinite sum of plane waves with kinetic energy E $=\frac{\hbar^2}{2m}|k+G|^2$ 2m is involved in the right side of the equation above. It is therefore not possible to work numerically with this. For this reason, this infinite sum must be truncated to a finite one, for

which the cut off energy E$_c ut$ which is defined as:

$$E_{cut} = \frac{\hbar^2}{2m} G_{cut}^2 \tag{2.59}$$

The basic set includes all plane waves whose kinetic energy is smaller than E$_c ut$ alone. Elevating the value of E$_c ut$ can help decrease the mistake in the calculation caused by the truncation of plane waves. Following a certain threshold, increasing E$_c ut$ does not significantly alter the system's total energy per atom. To calculate the electrical structure and obtain a convergent result, this E$_c ut$ value is employed in practice.

2.5.2 K-Space Integrations

A significant amount of effort is spent in density functional theory calculations evaluating k-space integrals of different functions in the Brillouin zone using the form

$$f = \frac{V}{2\pi^3} \int_{BZ} f(\mathbf{K}) d\mathbf{K} \tag{2.60}$$

where V denotes the solid crystal's unit cell volume. By adding up the value of the function f(k) at a finite collection of k-points with the appropriate weight, the integrals are computed numerically. The computations become more accurate as the sample size grows, and for a sufficiently high number of k-points, they may converge to the precise integral value. Therefore, in order to assess such integrals effectively, one must select the collection of k-points. Γ-centered k-mesh and Monkhorst-Pack k-mesh are the most often utilised k-meshes for taking equally spaced points in the Brillouin zone into consideration.The method known as the N × N × N k-mesh calculation is used to sample the Brillouin zone when N number of k-points are taken along the direction of each reciprocal lattice vector. In order to assess the convergence in the k-mesh, one must increase N until the total energy changes insignificantly with each additional N change.

2.5.3 Pseudopotential and Frozen core approximation

It is commonly known that there are two sorts of electrical states that exist in any atom: (i) Delocalized valence electron states, which actively contribute to shaping the electronic characteristics of the material; (ii) localised core electron states, which are closely connected to the nucleus. The related wave functions oscillate very quickly on a very short length scale due to the core electrons' tight bond to the nucleus, and their kinetic energies are significantly higher than those of the valence electrons. As a result, setting a very high cut off energy for the plane wave basis set is necessary to provide a meaningful description of these core states, which raises the computing costs.Therefore, certain appropriate estimates must be made in order to deal with the core electrons. This suggests that the pseudopotential theory be presented. The material's electrical and physical properties are preserved because the pseudopotential is designed to accurately replicate the valence electron states. Another name for this approximation is the frozen core approximation.Using $|\psi_c\rangle$ and $|\psi_v\rangle$, respectively, let us symbolise the wave functions that correspond to the valence and core electrons. The following Schrödinger equation is satisfied by them:

$$H|\psi^c\rangle = \epsilon^c|\psi^c\rangle \tag{2.61}$$

$$H|\psi^v\rangle = \epsilon^v|\psi^v\rangle \tag{2.62}$$

where ϵ^c and ϵ^v are the eigenvalues that correspond to the core and valence electron states, respectively, and H is the single-electron Hamiltonian. The electron density of the core electrons is now replaced by a smoothed function in the pseudopotential approximation. To accomplish this, we create a fresh collection of valence states $|\phi_v\rangle$ for single particles.

$$|\phi_v\rangle = |\psi_v\rangle + \sum_c \alpha_c \psi^c(\mathbf{r}) \tag{2.63}$$

The requirement that $|\psi^c\rangle$ and $|\psi^v\rangle$ are orthogonal to one another, i.e., $\langle\psi^c|\psi^v\rangle$=0, allows us to calculate the value of α^c in this case, which equals $\langle\psi^c|\phi^v\rangle$. Now that α^c has been determined, equation 2.63 can be rewritten as

$$|\phi^v\rangle = |\psi^v\rangle + \sum_c |\psi^c\rangle \langle\psi^c|\phi^v\rangle \tag{2.64}$$

Using the equation above, we can now write $|\psi^v\rangle$ as

$$|\psi^v\rangle = |\phi^v\rangle - \sum_c |\psi^c\rangle \langle\psi^c|\phi^v\rangle \tag{2.65}$$

This value of $|\psi^v\rangle$, when entered into equation 2.61, yields

$$H[|\phi^v\rangle - \sum_c |\psi^c\rangle \langle\psi^c|\phi^v\rangle] = \epsilon^c[|\phi^v\rangle - \sum_c |\psi^c\rangle \langle\psi^c|\phi^v\rangle] \tag{2.66}$$

which one could rewrite as

$$[H + \sum_c (\epsilon_v - \epsilon_c)|\psi_c\rangle\langle\psi_c]|\psi_v\rangle = \epsilon^c\psi_v\rangle \tag{2.67}$$

Thus, using a modified potential that replicates the identical eigenvalues v corresponding to the original valence states $|\psi_v\rangle$, the new valence electron states $|\phi_v\rangle$ follow the above single particle equation.

This new Hamiltonian is referred to as a pseudo Hamiltonian and is given as

$$H^{PH} = [H + \sum_c (\epsilon^v - \epsilon^c)|\psi^c\rangle\langle\psi^c] \tag{2.68}$$

and the corresponding modified nuclear potential is known as the pseudo-potential, which is expressed as

$$V^{PS} = V + \sum_c (\epsilon^v - \epsilon^c)|\psi^c\rangle\langle\psi^c] \tag{2.69}$$

where V is the attractive nuclear potential in H and the second component is the correction term, which tends to drive the corresponding states $|\phi_v\rangle$ from the core area because it is strictly repulsive in nature because $\epsilon_v > \epsilon_c$. The attractive nuclear potential that is protected close to the nucleus at the core area is felt by the new valence electron states as a result of the existence of this second term.

Consequently, the effective pseudo potential smoothes out significantly and loses its $\frac{1}{r}$ singularity for the nucleus at the centre. Thus, in the core region, the associated wave functions become substantially smoother. The pseudo potential technique is schematically shown in Fig.2.2. This figure illustrates the cut-off radius (r_c) beyond which the pseudo-wavefunction and pseudo-potential are the same as the original electron wavefunction and potential, respectively. On the other hand, the new valence states suffer a weaker potential in the core area, or within r_c.

Strange to this idea, a number of formalisms are put up to obtain more precise yet smoother pseudo potentials. Using norm-conserving pseudo potentials is one such widely used technique, which was first proposed by Hamann, Schlüter, and Chiang [33]. In this method, the all electron wave function is replaced by an effective pseudo wave function within the core radius (r_c), subject to the constraint that the norm of these two wave functions has the same value within r_c and that the wave functions are identical beyond r_c.Setting the core radius around the outermost maximum of the all electron wave function is necessary to achieve good

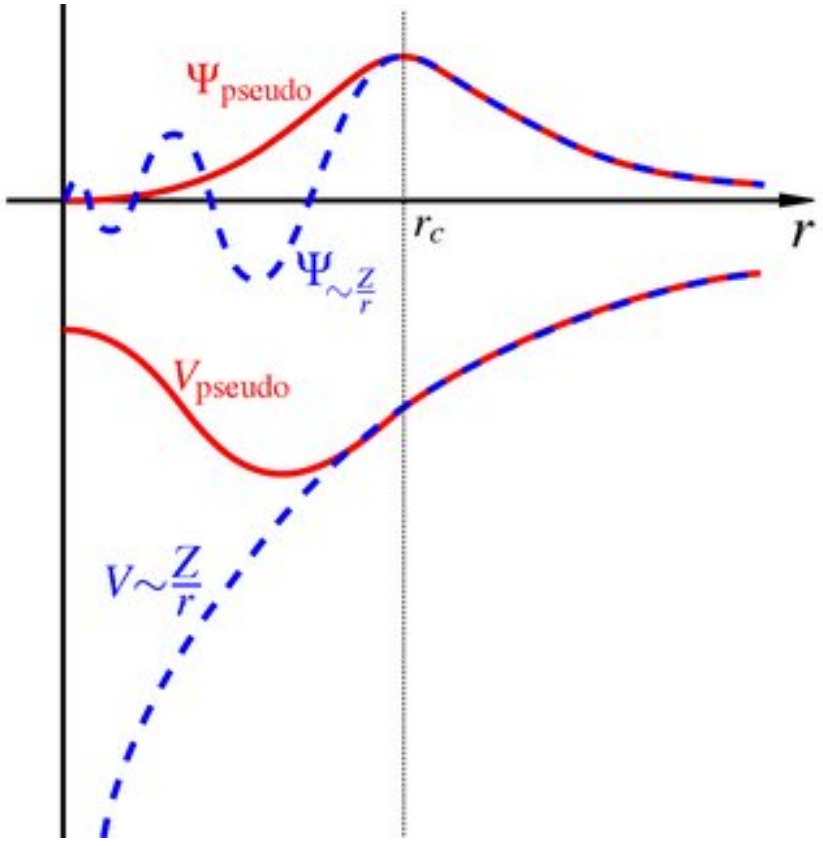

FIGURE 2.2: Schematic diagram of the Pseudopotential V^{PS}

transferability (i.e., performance in different chemical environments) of the wave function. This ensures that the pseudo wave function replicates the charge distribution and moment of the all electron wave function. Consequently, in order to explain the pseudo potential for elements with strongly localised orbitals, like rare earth and 3d elements, a large plane wave basis set is needed. In order to address this issue, the transferability of the wave function is adversely impeded if the core radius is selected beyond the outermost maximum of the all electron wave function. Additionally, there are issues with elements in the periodic table's first row that lack a core electron. A method for creating ultrasoftpseudopotentials (USPP) when the norm-conserving requirement is removed was proposed by Vanderbilt in 1990. Consequently, this method reduces the size of the basis set, increasing its computational efficiency. The lost information of wavefunctions close to nuclei, which can lead to misconceptions about certain material properties depending on the core electrons, is one drawback of the pseudo potential method. The Projector Augmented Wave (PAW) Method is another pseudo potential technique that was created to get over this drawback.

2.5.4 Projector Augmented-Wave(PAW) Method

In 1994, Blöchl presented the Projector Augmented Wave (PAW) Method[130]. This approach was modified for plane wave calculations by Kresse and Joubert[130]. Using this method, an all-electron wave function is created, allowing for the computation of all integrals as a sum of localised muffin-tin orbital contributions and integrals of smooth functions stretched over space[131]. Thus, the pseudo valence state wave function $\tilde{\psi}_i^v(r)$ and a linear transformation function that converts $\tilde{\psi}_i^v(r)$ into the all electron wave function $\tilde{\psi}_i^v(r)$ are combined to create the all electron wave function.

$$(\psi_j^v(r) = \tilde{\psi}_j^v(r) + \sum_i \left(|\phi_i\rangle - |\tilde{\phi}_i\rangle\right) \langle\phi_i|\hat{p}_i|\tilde{\phi}_i\rangle \tag{2.70}$$

In this case, the atomic site **R** is represented by index i, and the projector functions for pseudo partial waves ($\tilde{\phi}_i$) are represented by $\tilde{\rho}(\mathbf{r})$ which satisfies the orthogonality requirement $\langle \hat{P}_i | \tilde{\phi}_j \rangle = \delta_{i,j}$

The all-electron charge density can be expressed using the equation above as

$$\rho(\mathbf{r}) = \tilde{\rho}(\mathbf{r}) + \rho^1(\mathbf{r}) - \tilde{\rho}^1(\mathbf{r}) \tag{2.71}$$

where

$$\tilde{\rho}(\mathbf{r}) = \sum_i f_i \left| \tilde{\psi}_i(\mathbf{r}) \right|^2 \tag{2.72}$$

$$\rho^1(\mathbf{r}) = \sum_i f_i \sum_{j,k} \langle \tilde{\psi}_i | \tilde{p}_j | \phi_j(\mathbf{r}) \phi_k(\mathbf{r}) \rangle \langle \phi_k | \tilde{p}_k^\dagger | \tilde{\psi}_i \rangle \tag{2.73}$$

$$\tilde{\rho}_1(\mathbf{r}) = \sum_i f_i \sum_{j,k} \langle \tilde{\psi}_i | \tilde{p}_j | \tilde{\phi}_j(\mathbf{r}) \tilde{\phi}_k(\mathbf{r}) \rangle \langle \tilde{\phi}_k | \tilde{p}_k^\dagger | \tilde{\psi}_i \rangle \tag{2.74}$$

The occupancies of the eigenstates ($\tilde{\psi}_i^s$) s are indicated by f_i in the equations above. In this case, the pseudo-wavefunctions with plane wave basis are used to calculate the pseudo-charge density ($\tilde{\rho}(\mathbf{r})$). The onsite charge densities localised within the augmented sphere around each atom are denoted by ($\rho^1(\mathbf{r})$) and ($\tilde{\rho}^1(\mathbf{r})$). The system's total energy, which is also divided into three parts, can be calculated using these three charge densities.

2.6 Maximally localised Wannier Functions

A new set of basis functions, known as a superposition of the Bloch orbitals created by a sequence of unitary transformations, was developed by Gregory Wannier in 1937[132]. Wannier functions are the term given to these new orbitals. Atomic orbitals are not the same as these orbitals. Although these functions are local orbitals, there are situations in which the bandwidth is insufficient to make them local. The indeterminacy of the Blöch orbitals does not make these Wannier functions unique. In technical terms, these functions $\psi_R^n(r)$ reflect the wavefunctions in real space and are the Fourier transform of the Blöch wavefunctions Φ_{mk}. The

function's most prevalent form is

$$\psi_R(\mathbf{r}) = \frac{V}{(2\pi)^3} \int_{\mathrm{BZ}} [\sum_i U_{ij}^{\mathbf{K}} \Phi_{ik}(r) e^{-ik\cdot\mathbf{R}}\, d\mathbf{k} \tag{2.75}$$

where n and m are the band index, k is the wavevector, and $\psi_R^j(\mathbf{r})$ is the Wannier function at site R. The unitary matrix $U^(k)$ is responsible for transforming Blöch wavefunctions among themselves at every k points. Every decision made for $U^(k)$ generates a new set of Wannier functions with varying degrees of spatial extension, hence the choices are not unique. The Wannier spread, another name for this spatial extension, is provided as

$$\omega = \sum_j \left(\langle \psi_0^j(\mathbf{r}) | r^2 | \psi_0^j(\mathbf{r}) \rangle - \left| \langle \psi_0^j(\mathbf{r}) | r | \psi_0^j(\mathbf{r}) \rangle \right|^2 \right) \tag{2.76}$$

Typically, $U^(k)$ is selected so as to maximise the localization of the Wannier spread . The first to propose this technique to remove $U^(k)$'s arbitrariness was Marzari and Vanderbilt[133]. The entire Wannier spread can be separated into two terms: ω_I, which is gauge invariant, and $\tilde{\omega}$, which is dependent on the gauge choice $U^(k)$. It is possible to break down the term $\tilde{\omega}$ further into diagonal terms (ω_D) and off-diagonal terms (ω_{OD}).

$$\omega = \omega_I + \tilde{\omega} = \omega_I + \omega_D + \omega_{OD} \tag{2.77}$$

In the foregoing expression, ω_I, ω_D, and ω_{OD} are given as,

$$\omega_I = \sum_j \left(\langle \psi_0^j(\mathbf{r}) | r^2 | \psi_0^j(\mathbf{r}) \rangle - \sum_i \left| \langle \psi_R(\mathbf{r}) | r | \psi_0^j(\mathbf{r}) \rangle \right|^2 \right) \tag{2.78}$$

$$\omega_D = \sum_j \sum_{R\neq 0} \left| \langle \psi_R^i(\mathbf{r}) | r | \psi_0^j(\mathbf{r}) \rangle \right|^2 \tag{2.79}$$

$$\omega_{OD} = \sum_{i\neq j} \left| \langle \psi_R^i(\mathbf{r}) | r | \psi_0^j(\mathbf{r}) \rangle \right|^2 \tag{2.80}$$

While this method works well for calculating Wannier spreads for isolated bands, it

is more challenging to handle entangled bands, particularly in the k point regions where the bands are hybridising. The maximum localised Wannier functions are found by a disentanglement process[134] in order to get around this issue.

Chapter 3

Multifunctional Heusler Materials

3.0.1 Heusler Topological Insulators

The diversity of Heusler compounds (over 1,500 members) allows for optimisation of parameters such as SOC strength and gap size across different compounds. This is important for understanding topological order and phase transitions, as well as designing realistic applications[135]. Heusler compounds, particularly those containing rare earth elements with strongly correlated f electrons, have unique ground-state properties such as magnetism[136], unconventional superconductivity[137–139], and heavy fermion behaviour[140]. Heusler compounds are ideal for achieving novel topological effects (e.g., image monopole effect and axions), new topological phases (e.g., topological superconductors), and diverse applications.

The rare earth Heusler compounds LnPtBi (Ln = Y, La, and Lu) have been presented as a model system with nontrivial TSSs and substantial band inversion[141–143]. The compounds have a non-centrosymmetric lattice (space group $Fm\bar{3}m$, No. 216). LnPtBi has three interpenetrating fcc lattices that create a metallic multilayer along the [111] direction. The rare earth elements platinum and bismuth are represented by successive atomic layers. Inversion of the Γ_8 and Γ_6 bands creates a gapless semimetal with degenerate Γ_8 bands at Fermi energy. LnPtBi is classified as a TI due to its inverted band structure, similar to HgTe.

Despite much research in theory [141–143] and experiment [144–146], the topology of Heusler TIs remained elusive until recently [147, 148]. Comprehensive ARPES measurements and ab initio computations were used to determine Dirac-type surface states in Heusler compounds LuPtBi, YPtBi (120), and LuPtSb[148]. Unlike many TIs, LnPtBi's TSSs are located below the E_F and overlap with the bulk valence bands, similar to HgTe[149–151]. Metallic surface states with large Rashba splitting cross the E_F, making these compounds promising for spintronic applications and potentially mediating topologically nontrivial superconductivity in their superconducting phase.

3.0.2 Heusler Magnetic Weyl Semimetals

Combining band inversion and magnetism in a single Heusler compound allows for the creation of magnetic WSMs. Substituting Ln with most lanthanides produces magnetism due to the f electrons. When Ln = Gd or Nd, GdPtBi and NdPtBi show magnetism from their 4f electrons while maintaining the Γ_8-Γ_6 band inversion. GdPtBi (126, 127) and NdPtBi (128) exhibit antiferromagnetism (AFM) at temperatures lower than their respective transition temperatures (T_N = 9.0 K and 2.1 K). The magnetic structures of GdPtBi and NdPtBi differ. GdPtBi is a type-II antiferromagnet, while NdPtBi is a type I antiferromagnet. This suggests that the magnetic ordering below the Néel temperature has no impact on Weyl physics, as discussed further below. It is important to note that neodymium and gadolinium have different sizes, anisotropy moments, and degeneracy. Experimental studies have revealed that GdPtBi and NdPtBi become WSMs when the exchange splitting of the Γ_8 and Γ_6 bands is sufficient to establish the Weyl points[152, 153].

Other magnetic and nonmagnetic Heusler compounds, including Co-based Heusler materials XCo_2Z (X = V, Zr, Nb, Ti, Hf; Z = Si, Ge, Sn)[154] and strained Heulser TI materials[155], have been identified as potential WSM candidates. The KHgSb honeycomb Heulser materials exhibit weak TIs[156] and nonsymmorphic symmetry-protected topological states[157]. Nonsymmorphic symmetry-protected

DSMs have been observed in the AFM Heusler material CuMnAs[158]. The chiral AFM Heusler compounds Mn_3X (X = Sn, Ge) with significant AHE at room temperature[159, 160] are anticipated to be AFM WSMs[161]. Other Heusler-like ternary compounds, including ZrSiS[162] and LaAlGe[163], have also been identified as topological semimetals. We anticipate further discovery of WSMs and DSMs in the prolific Heusler family and related compounds.

In this chapter, We will discuss two Heusler compounds that exhibit intriguing topological and electronic properties. The first compound, Co_2VAl, demonstrates a gapped nodal line half-metal behavior, and the second, Co_2CrGa, reveals triple point generated Weyl points. Both compounds[1] highlights the rich physics and potential applications of Heusler alloys in spintronics and topological materials.

Co_2VAl is a Heusler compound where cobalt (Co) and vanadium (V) occupy the transition metal sites, and aluminum (Al) occupies the main-group element site.

3.0.3 Nodal-line semimetal Heusler compound Co_2VAl

Since the intrinsic AHE and magnetism are closely related to each other [164], it is essential to identify the magnetic nature of the studied compound. In Fig.3.1(a) we have shown the crystal structure of Co_2VAl and the corresponding high symmetry point in the Brillouin zone. Magnetic moments of Co_2VAl are calculated using the first-principles method and transition metal atoms Co and V atoms have major contributions with magnetic moments $\mu_{Co} = 0.911\ \mu_B$/f.u and $\mu_V = 0.210\ \mu_B$/f.u respectively. Al behaves like a non-magnetic atom and the total magnetic moment per formula unit of this system is 2.02 μ_B/f.u. The two Co and one V atoms contribute 18 and 5 valence electrons, whereas one Al atom contributes 3 valence electrons. Therefore, Co_2VAl is expected to have an effective magnetic moment of approximately 2 μ_B/f.u. Our calculations show that this material is a half

[1]This chapter is based on "Nodal-line and triple point fermion induced anomalous Hall effect in the topological Heusler" compound Co2CrGa - S. Chatterjee, J. Sau*, S. Samanta, B. Ghosh, N. Kumar, M. Kumar, and K. Mandal, Phys. Rev. B 107, 125138 (2023) and "Anomalous Hall effect in topological Weyl and nodal-line semimetal Heusler compound Co2VAl"- S. Chatterjee, J. Sau*, S. Ghosh, S. Samanta, B. Ghosh, M. Kumar and K. Mandal, J. Phys.: Condens. Matter,35035601 (2023)

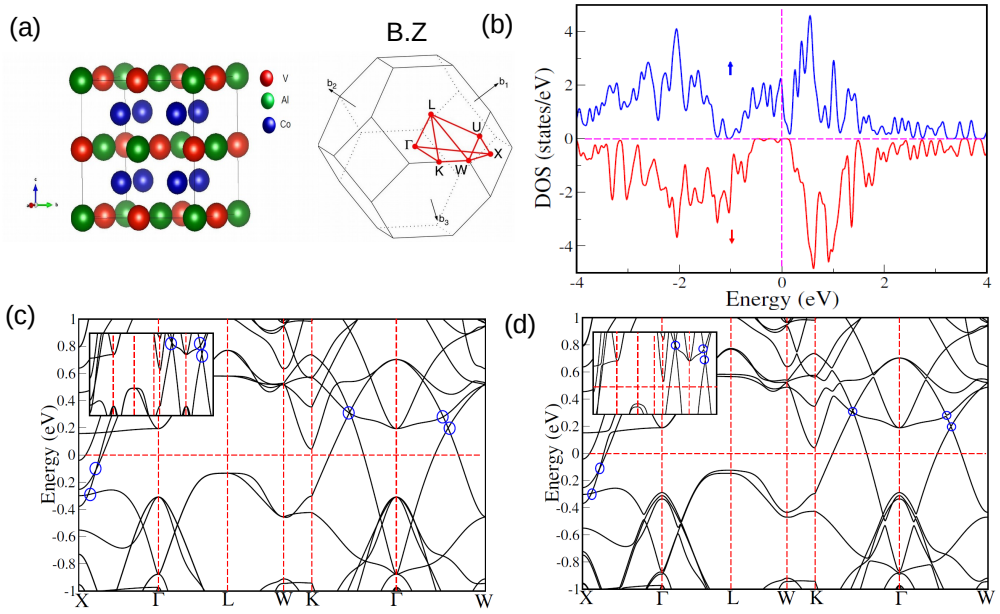

FIGURE 3.1: (a) Crystal structure of Co_2VAl with $Fm\bar{3}m$ space group. Co, Al, and V atoms are shown in blue, green, and red, respectively, and the Brillouin zone (BZ) of the crystal Co_2VAl. (b) The total density of state (DOS) of Co_2VAl. Blue and red curves represent the total DOS for the majority and minority spins. (c) The band structure of Co_2VAl in the absence of SOC (crossing points are marked by blue circles). The inset shows the enlarged view of the crossing points. (d) The band structure of Co_2VAl in the presence of SOC (gapped nodal lines are shown in blue circles). The inset shows the enlarged view of gapped nodal lines.

metallic system and follows the SP rule with magnetic moment 2.02 μ_B/f.u. The observed magnetic behavior is in good correspondence with the literature [165]. The calculated magnetic moment for Co_2VAl is also in good agreement with our experimentally obtained value. In Fig.3.1(b) a spin-resolved density of state (DOS) is shown, and we noticed that the DOS is fully gapped for minority spin, whereas it is metallic for majority spin.

To understand the topological aspects of the compound, the band dispersions are calculated using plane wave-based pseudopotential [166] in the absence and presence of SOC. There are many band crossings from nodal lines in the absence of SOC. In Fig.3.1(c) all the nontrivial crossing points near Fermi energy are marked by a blue circle without SOC along high symmetry points, and the inset shows the enlarged view of the crossing points. However, in the presence of SOC, the nodal lines are gapped out except for a few symmetry-protected Weyl points.

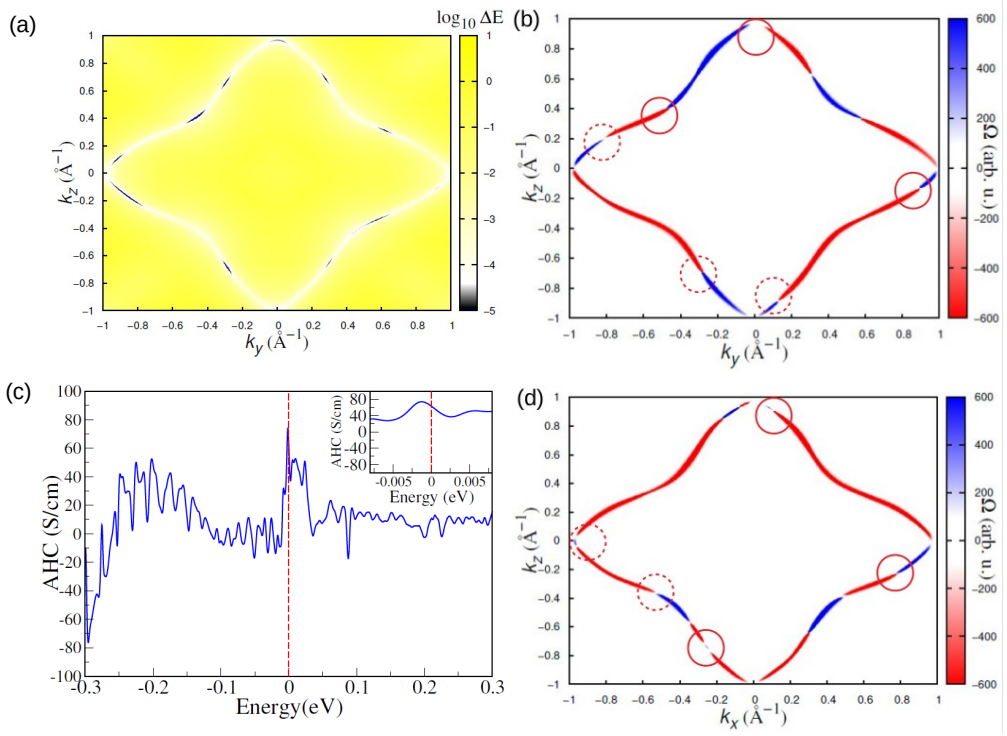

FIGURE 3.2: (a)Energy gap $\Delta E(k_y, k_z)$ is plotted in k_y-k_z plane at $k_x = 0$ with SOC. (b) and (d) Berry curvature distribution in k_y-k_z plane and k_x-k_z plane. (c) Energy $(E - E_F)$ dependence of the AHC. Inset represents the zoomed view of the energy dependence of the AHC close to E_F.

We consider the SOC and direction of magnetic polarization along [001], therefore, the nodal line remains gapless in the $k_z = 0$ plane. The band dispersions in the presence of SOC are shown in Fig.3.1(d) around the Fermi-energy and blue circles along Γ-W and Γ-X symmetry path indicate gapped out band crossings. The inset shows the enlarged view of the gapped nodal lines. The point group crystal symmetry of Co_2VAl is $Fm\bar{3}m$ (space group 225). It has three mirror planes [167], $M_x(k_x{=}0)$, $M_y(k_y{=}0)$, $M_z(k_z{=}0)$ and three C_4 rotation axes in absence of finite magnetization. These mirror planes protect the gapless nodal lines in the band structure in $k_x = 0$, $k_y = 0$, $k_z = 0$ planes.

The presence of SOC along [001] direction only preserves the mirror symmetry $M_z = 0$ and C_{4z} rotational symmetry. Therefore, two nodal lines on the $k_x = 0$, $k_y = 0$ planes are expected to gap out and the nodal line along the $k_z = 0$ plane should be preserved and some of the Weyl points are expected to be present out of $k_z = 0$ plane. We analyzed the electronic band structure of the tight-binding model

TABLE 3.1: The Weyl points' positions, Chern numbers, and the energy relative to the E_F of Co_2VAl.

Weyl points	k_x	k_y	k_z	Chern number	E-E_F
1	-0.52	0.009	-0.36	-1	0.26
2	-0.23	-0.007	-0.76	1	0.04
3	0.78	-0.004	-0.22	1	0.07
4	0.10	0.01	0.91	1	-0.2
5	-0.0006	-0.27	-0.69	-1	0.14
6	-0.009	0.89	-0.12	1	-0.16
7	0.01	0.13	-0.88	-1	-0.15
8	0.0009	-0.46	0.40	1	0.29
9	-0.95	-0.05	0.03	-1	-0.26
10	0.008	-0.81	0.20	-1	-0.03

Hamiltonian calculated using the Wannier90 [168, 169] calculations with the help of Wanniertools [**?**]. In Fig.3.2(a), the color plot of the energy gap between the lowest conduction and the topmost valence band is shown using the logarithmic scale in the presence of SOC at the $k_x = 0$ plane. The gaps smaller than 10^{-4} eV are considered to be gapless, and the oval structure shown in Fig.3.2(b) is mostly gapped except for Weyl points. Due to small gaps at the nodal lines a large berry curvature in $k_x = 0$, and $k_y = 0$ planes are noticed as shown in Fig.3.2(b) and Fig.3.2(d) respectively. Filled and open circles represent the Weyl points with chiral charge +1 and -1 in $k_x = 0$, $k_y = 0$ planes as shown in Fig.3.2(b) and Fig.3.2(d). The location of energy and momentum coordinates of Weyl points are listed in Table 3.1. Wannier charge centers are also calculated to confirm the chirality at Weyl points. The AHC is proportional to the Berry curvature which is a geometrical property of energy bands. The Berry curvature creates a transverse anomalous velocity in the electronic motion and generates a large AHC.

The intrinsic AHC can be evaluated in the linear response theory of Kubo formalism [170] and AHC in the xy plane can be expressed as

$$\sigma_{xy} = -\frac{e^2}{\hbar} \int \frac{d^3k}{(2\pi)^3} \sum_n \Omega_n^z(k) f_n(k) \tag{3.1}$$

Ω_n^z is Berry curvature and it can be written as

$$\Omega_n^z = -2i \sum_{m \neq n} \frac{\langle \psi_{nk} | v_x | \psi_{mk} \rangle \langle \psi_{mk} | v_y | \psi_{nk} \rangle}{[E_m(k) - E_n(k)]^2} \tag{3.2}$$

where $f_n(k)$ represents the Fermi-Dirac distribution function,n is for the occupied bands index,$E_n(k)$ is the eigenvalue of the nth eigenstate $\psi_n(k)$,$v_i = \frac{1}{\hbar}\frac{\partial H(k)}{\partial k_i}$ is the velocity operator along the i (i=x,y,z) direction. To calculate AHC, the spin-orbit coupling is considered along the [001] which is also a direction of magnetic polarization. Nearly degenerate bands near the nodal line in $k_x = 0$, $k_y = 0$ plane have large Berry curvature as shown in Fig.3.2(b), Fig.3.2(d) and contribute to the intrinsic AHC. At the E_F calculated AHC value of Co_2VAl is ~ 64 S/cm which is in good agreement with the experimentally found intrinsic AHC 70 S/cm. The experimentally calculated AHC is comparable to that reported for various Co_2-based ferromagnetic full Heusler compounds and other magnetic materials [171–175]. The energy dependence of AHC for Co_2VAl is also shown in Fig.3.2(c), and the inset illustrates the zoomed view of the energy dependence of AHC near the E_F.

3.0.4 Triple point fermion in Co_2CrGa

Magnetic moments of Co_2CrGa are calculated using the first-principles method and the obtained total magnetic moment is in good agreement with the experimental value[176]. Magnetic moments of Co_2CrGa are calculated using the first-principles method, and transition metal atoms Co and Cr have major contributions to magnetic moments with $\mu_{Co} = 0.706$ μ_B/f.u and $\mu_{Cr} = 1.701$ μ_B/f.u, respectively. Ga behaves like a non-magnetic atom and the total magnetic moment per formula unit of this system is 3.019 μ_B/f.u. The two Co and one Cr atoms contribute 18 and 6 valance electrons, whereas one Ga atom contributes 3 valance electrons. Therefore, Co_2CrGa is expected to have an effective magnetic moment of approximately 3 μ_B/f.u. Our calculation suggests that this compound is a half metallic system and follows the Slater-Pauling (SP) rule with magnetic moment

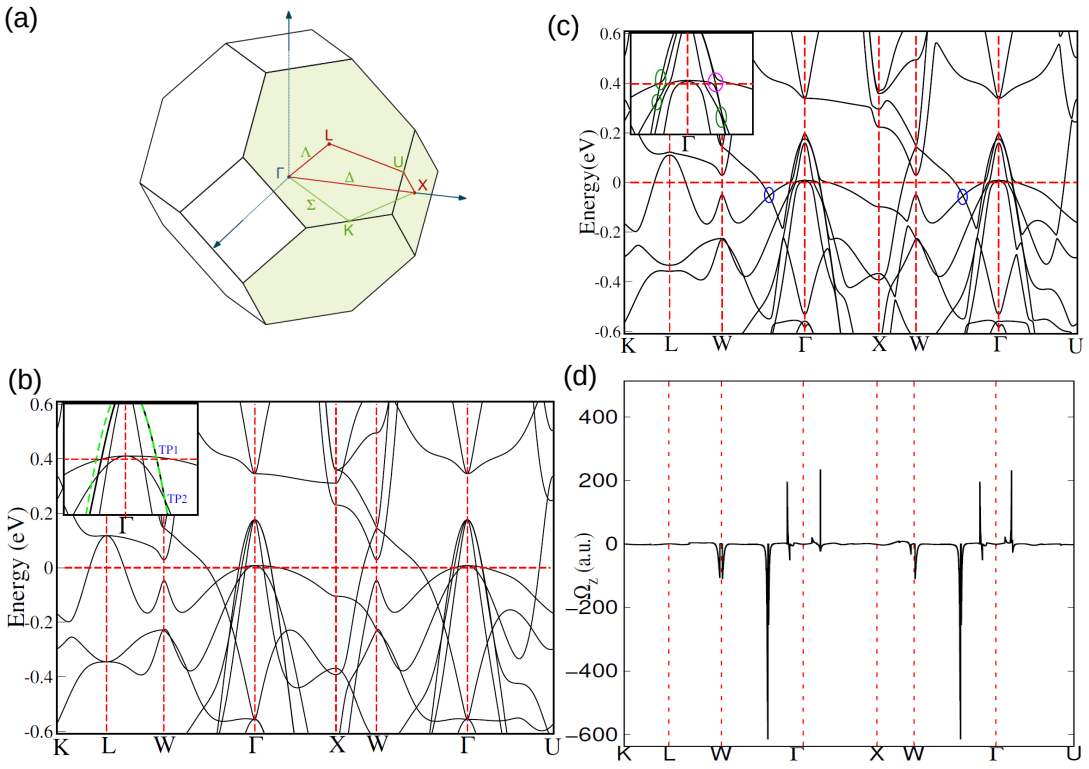

FIGURE 3.3: (a) Brillouin Zone (BZ) of Co_2CrGa. (b) The band structure of Co_2CrGa without SOC. In the inset, we also point out the TPs. (c) The band structure of Co_2CrGa with SOC. The Weyl points and the gapped nodal lines are shown by green and blue circles. (d) The Berry curvature along the high symmetry lines due to the nontrivial crossings.

3.019 μ_B/f.u The calculated magnetic moment for Co_2CrGa is in good agreement with our experimental investigation.

To understand the topological aspects of the compound the band dispersions are calculated using plane wave-based pseudopotential [166] in the absence and presence of SOC. Fig.3.3(b) illustrates several bands crossings that form nodal lines in the absence of SOC. There are also different kinds of topological nontrivial crossings in the presence of SOC encircled by blue, green, and magenta colors as shown in Fig.3.3(c) and corresponding to these nontrivial crossings large BC is observed.

In order to further define the class of these nontrivial crossing points the crystal symmetries are considered. The space group of Co_2CrGa is $Fm\bar{3}m$ (space group no. 225) and the corresponding BZ with marked high symmetry point is shown in Fig.7.5(a). This symmetry group contains three mirror planes [167], $M_x(k_x{=}0)$,

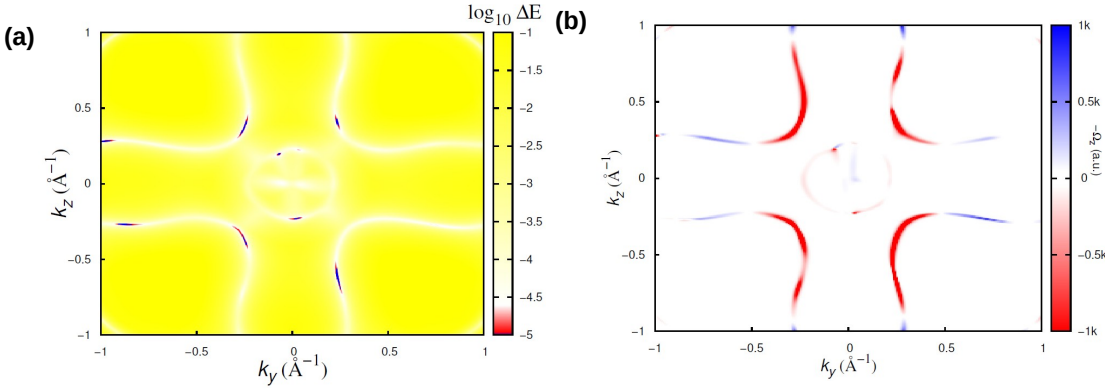

FIGURE 3.4: For Co_2CrGa with SOC (a) Energy gap, between two crossing bands at E = -0.045 eV and white line represent gapped out nodal line. (b) Along the gapped nodal line, the Berry curvature distribution is shown at K_x=0 plane.

$M_y(k_y{=}0)$, $M_z(k_z{=}0)$ and three C_4 rotation axes in the absence of finite magnetization. These mirror planes protect the gapless nodal lines in the band structure in $k_x = 0$, $k_y = 0$, and $k_z = 0$ planes. The presence of SOC along [001] direction only preserves the mirror symmetry $M_z = 0$ and C_{4z} rotational symmetry. Therefore, two nodal lines on the $k_x = 0$, $k_y = 0$ planes are expected to gap out and the nodal line along the $k_z = 0$ plane should be preserved. The band dispersions in the presence of SOC are shown in Fig.3.3(c) around the Fermi-energy and the blue circles along Γ-W high symmetry path indicate gapped-out band crossings. Due to small gaps along the nodal lines, a large berry curvature in the $k_x = 0$ plane is noticed. Fig.3.4(a) and Fig.3.4(b) exhibit the energy gap and the corresponding BC in $k_x = 0$ plane. In Fig.3.3(d) corresponding to gapped nodal lines a large negative BC is observed along the high-symmetry point Γ-W.

TABLE 3.2: The Weyl points' positions, Chern numbers, and the energy relative to the E_F of Co_2CrGa.

Weyl points	k_x	k_y	k_z	Chern number	E-E_F
W_1	1.080	-0.0014	-0.41	-1	-0.10
W_1	-1.080	-0.0077	0.41	1	-0.11
W_2	-0.004	1.0811	0.41	1	-0.06
W_2	0.005	-1.0815	-0.4165	-1	-0.04
W_3	-0.0139	-0.9110	-0.0062	1	-0.01
W_3	-0.0100	0.910	-0.014	-1	-0.02

This crystal structure has also high-symmetry axis of the C_{3v} point group which

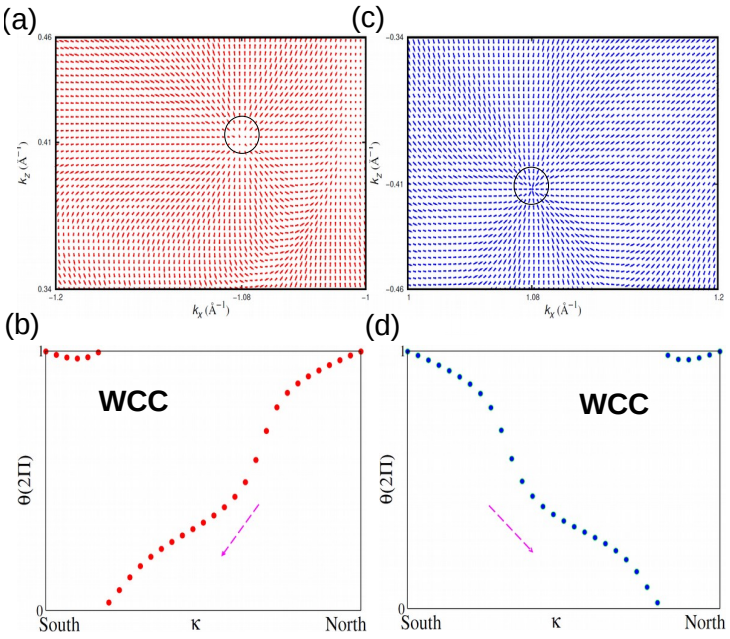

FIGURE 3.5: For Co_2CrGa with SOC normalized Berry curvatures is shown for Weyl point W_1 (a) Source type (W_1+) which is indicated by an outward red arrow from marked black circle (b) Average position of wannier charge centre corresponding to +1 chern number (c) Sink type (W_1-) which is indicated by the inward blue arrow marked black circle (d) Average position of wannier charge centre corresponding to -1 chern number.

has three-fold rotational symmetry (C_3) along the [111] direction. Due to this symmetry, two-fold degenerate bands are noted as shown in the inset of Fig.3.3(b) by thick black and dotted green line. The crossing point of this doubly degenerate band with non-degenerate bands give rise to a pair of triple points [177] in the absence of SOC and these are indicated as TP1 and TP2, shown in the inset of Fig.3.3(b). In the presence of SOC along [001] direction TP1 splits out as shown in the inset of Fig.3.3(c) inside a magenta circle and TP2 splits into a pair of Weyl points which is shown in the inset of Fig.3.3(c) inside green circle (at -0.08 eV). To understand the texture of these Weyl points, we calculate the normalized BCs which indicate the flux at these two opposite chiral Weyl points and their precise position and topological charges are presented in Table 1. W_1+ is the source type where the flux is along an outward direction as shown in Fig.3.5(a) whereas the sink type W_1-, where the flux is along an inward direction is shown in Fig.3.5(c). Moreover, we also investigate the average position of the WCC obtained by the Wilson-loop method applied on a sphere that encloses these two nodes of opposite

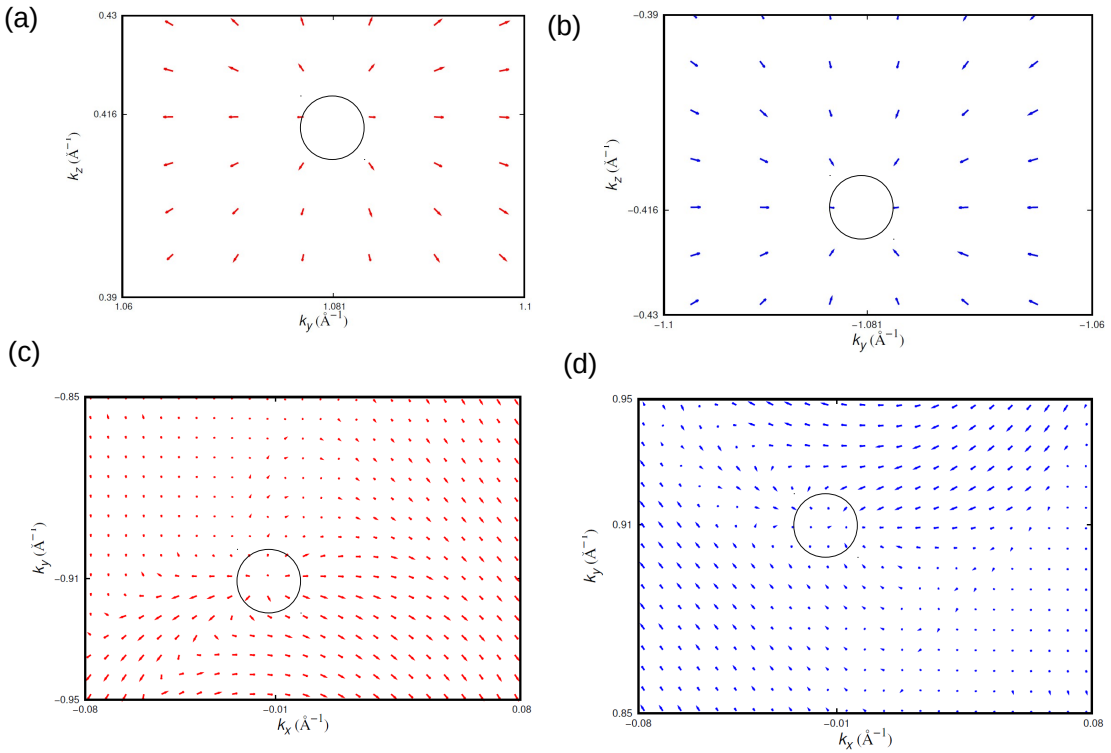

FIGURE 3.6: Normalized Berry curvatures show source and sink type corresponding to Weyls points W_2 and W_3.

chirality. It is observed that the average WCC shifts north to south corresponding to Chern no +1 for W_1 as shown in Fig.3.5(b) while it shifts south to north suggesting the chern number of W_1 is -1 as shown in Fig.3.5(d). We did a similar exercise for other Weyl nodes denoted by green circles along the high-symmetry point Γ-W. (see Fig.3.6), and corresponding to these Weyl points a large BC is noted.

To calculate the AHC the SOC is considered along the direction of magnetic polarization [001]. Nearly-degenerate bands near the nodal line in $k_x = 0$, $k_y = 0$ plane have large BC as shown in Fig.3.4(b) and contribute to the intrinsic AHC. Fig.3.7 illustrates the energy dependence of the AHC. The giant value ($\sim$ 1000 S/cm) of AHC near the gapped nodal line ($\sim$ 0.05 eV below the E_F) is shown in Fig.3.7 inside a red circle. This value of AHC is expected to be large due to the maximum BC value at that point as discussed earlier but at the E_F the AHC value decreases to 504 S/cm due to the positive value of the BC near the Weyl points crossing. The experimentally obtained intrinsic AHC is comparable to that of

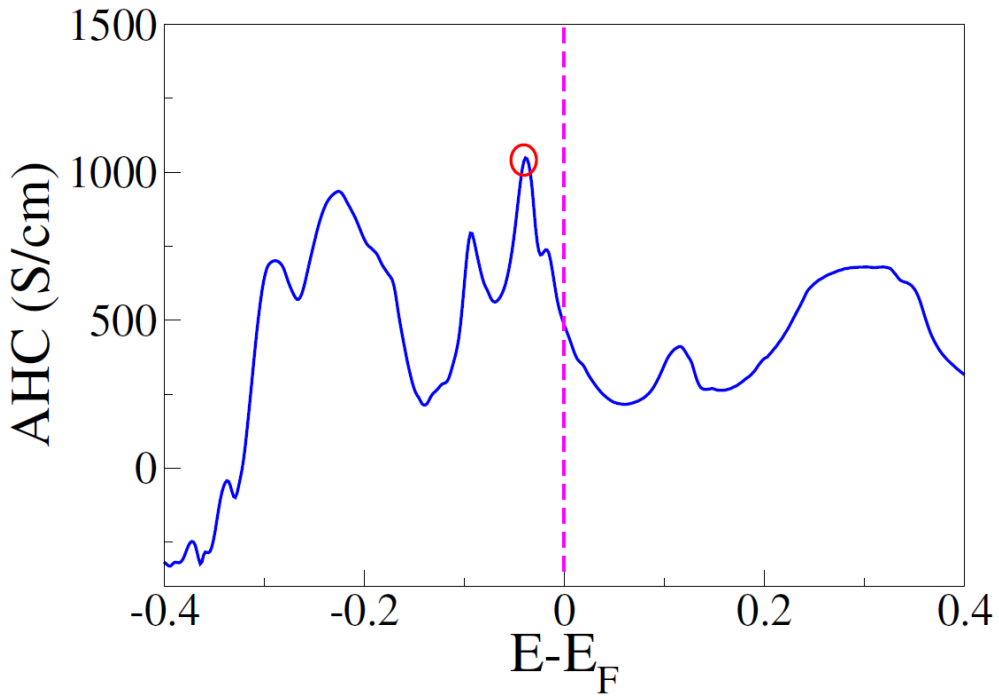

FIGURE 3.7: Energy (E-E_F) dependence of the AHC For Co_2CrGa where the red circle is the position of the gapped nodal line (at Energy -0.05 eV).

the theoretically calculated intrinsic AHC value for this ferromagnetic full Heusler compound.

Chapter 4

Hydrostatic Pressure-Induced Anomalous Hall Effect in Co_2FeSi Semimetal

4.1 Introduction

In recent years, the field of condensed matter physics has witnessed a burgeoning interest in three-dimensional topological semimetals (TSMs) exhibiting a symmetry-protected gapless quantum state which arises from novel physical phenomena and has many potential applications in device fabrication [178–181]. The TSMs have linear dispersion near the crossing points they are divided into three types based on the degeneracy of the band crossing points in the Brillouin zone (BZ). The first one is zero-dimensional (0D) nodal points, which include Weyl points[178], Dirac points [182], triple points[183] and other higher degenerate nodal points [184]. The One-dimensional (1D) nodal-line (NL) systems[185] such as nodal rings [186], nodal chains [187], and nodal nets [187] are of second type. Two-dimensional (2D) nodal surfaces[188] are the third one.

The 0D nodal point topological systems have been extensively studied due to their exotic transport properties in the last decade [189, 190], however, 1D NL

system studies have only recently begun [191, 192]. The search for materials with significant anomalous transport features has gained popularity recently, particularly for TSMs[193]. The TSMs material is one most promising candidates for the 1D NL material and some of these like Fe_3GeTe_2,CrB_2,CaP_3,LnX (Ln=La, Gd; X=Cl, Br)[194–198] etc exhibits anomalous transport properties which are visible as a transverse voltage drop caused by a longitudinal current that is, only caused by the intrinsic spin-orbit coupling (SOC) and magnetism. The origin of anomalous transport in these materials can arise due to two mechanisms: first, the intrinsic mechanism in which the finite Berry curvature (BC) contributes to anomalous transport properties and the second is the extrinsic mechanism, includes the side jump[199] and skew scattering[200] contribution both of which come from spin-orbit mediated electron scattering off the disorder. The intrinsic property is independent of disorder details and depends solely on the topology of the electronic band structure [201–203]. In fact, a large number of ferromagnetic [204–207] and antiferromagnetic materials [208–210] show large intrinsic anomalous Hall conductivity (AHC) and such anomalous behavior is contributed due to the emergence of large BC in momentum space [204, 205, 211, 212]. However, the large AHC materials like Heusler ferromagnets Co_2MnGa[206, 213] and Co_2MnAl [207] have the conductivities order of 10^3 S/cm and are of intrinsic origin.

The family of Heusler compounds is considerably large comprising more than 1,000 members and can display paramagnetic, ferromagnetic, and antiferromagnetic properties and fascinating anomalous electric, thermal, and thermoelectric transport properties [214]. The AHC has been reported to be intrinsic in several Heusler compounds such as Co_2CrGa, Co_2VAl,Co_2FeGe,Co_2MnGa[185, 206, 213, 215, 216]. The major challenge in these compounds is to design Heusler compounds with large anomalous transport properties and their tunability of intrinsic anomalous behavior i.e. going from a low to high AHC. Another challenge is to understand the suitable parameters like applying the pressure and doping of the compound to tune from dominant extrinsic to intrinsic transport properties in Heusler. The intrinsic mechanism is related to BC near the NL and the spin-orbit interaction

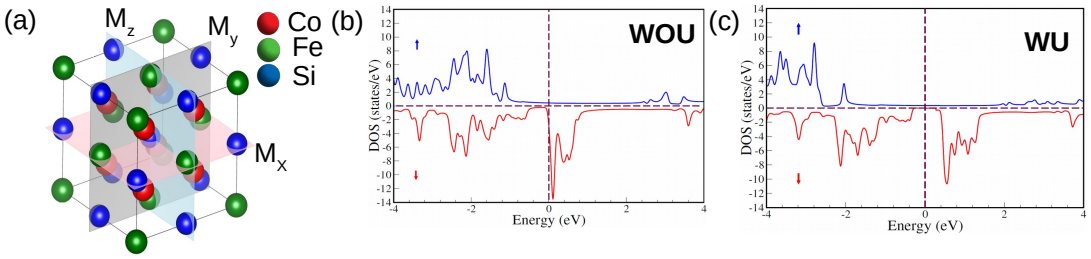

FIGURE 4.1: (a) The Co_2FeSi crystal structure features three distinct mirror planes where red, green, and blue balls represent Co, Fe, and Si respectively. (b) The total density of states (DOS) of Co_2FeSi without Hubbard U (WOU) exhibits semi-metallic characteristics. (c) The total DOS of Co_2FeSi with Hubbard U (WU) exhibits a half-metallic nature. The blue and red curves denote the total DOS for the majority and minority spins, respectively.

helps to open a tiny gap near the gapless line [193, 216]. The intrinsic mechanism strongly depends on the energy offset of the NL from the Fermi level (E_F) [194, 217]. Therefore, it is necessary to find either a material that has NL near E_F or away from it such as in some of the Heusler compounds. In the case of Heusler compounds E_F or NL can be easily shifted through hydrostatic pressure or doping.

In this chapter[1], our ab-initio density functional theory (DFT) calculation notes that there is NL crossing at 0.1 eV above the E_F of the electronic structure of Co_2FeSi. The DFT calculation without Hubbard U of this material suggests the semimetallic properties with a non-integer magnetic moment which are contradictory to the experimental observation of integer magnetic moment and half-metallic behavior. We also show that a finite Hubbard U is required to fix these discrepancies, but it shifts the NL crossing point to 0.4 eV above E_F and opens a gap in the minority spin channel. We also investigate the effect of hydrostatic pressure on the NL location and show that it shifts towards the E_F, and altering the AHC from extrinsic to intrinsic. A thorough analysis of the NL symmetry-breaking mechanism is provided in the presence of SOC with magnetization along [001] direction. We also analyze the symmetry-protected Weyl nodes and their chirality. Moreover, the NL is situated at E_F at 26 GPa, creating a large AHC.

[1]This chapter is based "Hydrostatic Pressure-Induced Anomalous Hall Effect in Co 2 FeSi Semimetal" - J. Sau*, D.Sa,and M. Kumar, Electron.Struct.6 015008 (2024)

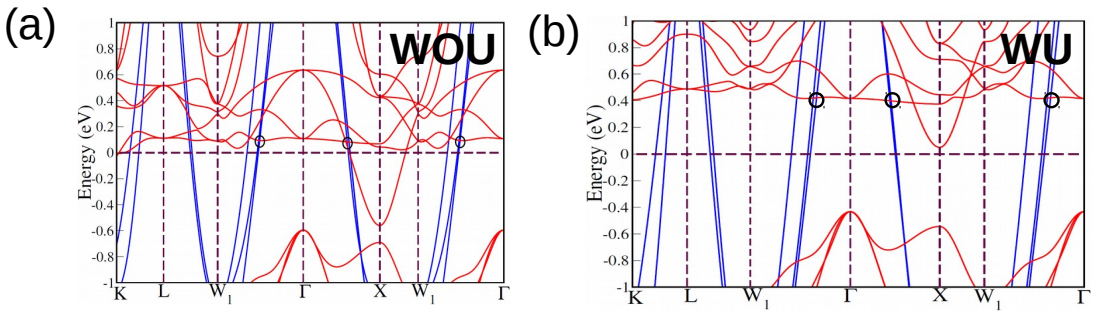

FIGURE 4.2: (a) The band structure of Co_2FeSi without Hubbard U (WOU). (b)The band structure of Co_2FeSi with Hubbard U (WU), where the crossing point has been shifted to 0.38 eV above the E_F.

4.2 Methods

We theoretically investigate the electronic band structure of the real materials employing the ab initio DFT calculation and for this, we employ the VASP package [218] with a plane-wave basis set and pseudopotentials. The cutoff energy of the plane waves is 600 eV and the exchange-correlation potential is described in the generalized-gradient approximation (GGA+U) [219]. The integration in k-space are carried out on a 13 ×13×13 grid. All structures are relaxed until forces smaller than 0.001 eV/Å. Previous studies suggest that full Heusler compounds with moderate magnetic moments require GGA+U DFT calculations to explain the experimental results [220, 221]. Therefore, we use a similar numerical approach to study the magnetic and transport properties of the full Heusler compound Co_2FeSi. In the next step we extract Wannier functions from the DFT band structure via the WANNIER90 package [222, 223]. The initial projections are chosen as s and d orbitals of Co and Fe and s and p orbitals of Si. From the Wannier functions we construct a tight-binding Hamiltonian H to calculate the BC in the system via the Kubo formula using Wanniertools[224].

4.3 Materials characterization and Magnetism

The crystal structure of Co_2FeSi is of the Heusler type which is a ternary intermetallic compound consisting of three metallic elements arranged in a specific

crystal structure. It has a cubic structure that belongs to the space group $Fm\bar{3}m$ (space group no. 225) with a lattice parameter of a_0=5.64Å[225]. Our optimized structure obtained using ab initio calculations is consistent with experimentally found crystal structure. The Co and Fe atoms occupy the face-centered cubic (fcc) sublattice while the Si atoms occupy the body-centered cubic (bcc) sublattice. The Co and Fe atoms are partially ordered on the fcc sublattice, forming a B2-type structure while the Si atoms occupy the interstitial sites. The unit cell of Co_2FeSi contains 32 atoms with the atomic positions given as follows: Co at (0,0,0), Fe at (0.5,0.5,0), and Si at (0.25,0.25,0.25) as shown in Fig.4.1(a).

The ab initio calculation suggests that Co_2FeSi is a typical ferromagnet with a magnetic moment of 5.35 μ_B/f.u. However, this value contradicts with the experimentally found magnetic moment 6.0 μ_B/f.u [225] and it is observed to be a half-metallic system. These discrepancies may arise because DFT underestimates the electronic correlation due to higher charge fluctuations. To account for the electronic correlation underestimate, we employ the effective Coulomb-exchange interaction U_{eff} (U-J), where U and J are the Coulomb and exchange parameters, respectively. It is noticed that a magnetic moment of 6.0 μ_B/f.u is achieved by taking values of U_{eff}=4 eV for Co and 3.5 eV for Fe. The introduction of U_{eff}'s have two consequences: the first one is DOS at E_F is suppressed creating a gap in the minority spin channel as shown in Fig.4.1(b) and (c) and the second one is a finite shift in the minority spin band, making double occupancy energetically expensive. The up spin occupancy is favored by the Hunds coupling but placing a down electron in the same orbit will need more energy at finite U_{eff}. The finite shift in the energy dispersion due to finite U is shown in Fig.4.2(a) and (b). According to the Slater-Pauling (SP) rule[226] the magnetization and the number of valence electrons can be related as $M = Z - 2N^{\downarrow}$ [226, 227] and for full Heusler half-metal $N^{\downarrow}$ is 12 and M =6 μ_B/f.u. We notice that our calculations give $N^{\downarrow}$ =12.325 in absence U and 12.008 for finite U. The finite U makes the system half metallic and the calculated magnetic moment is consistent with the experimentally observed value [225].

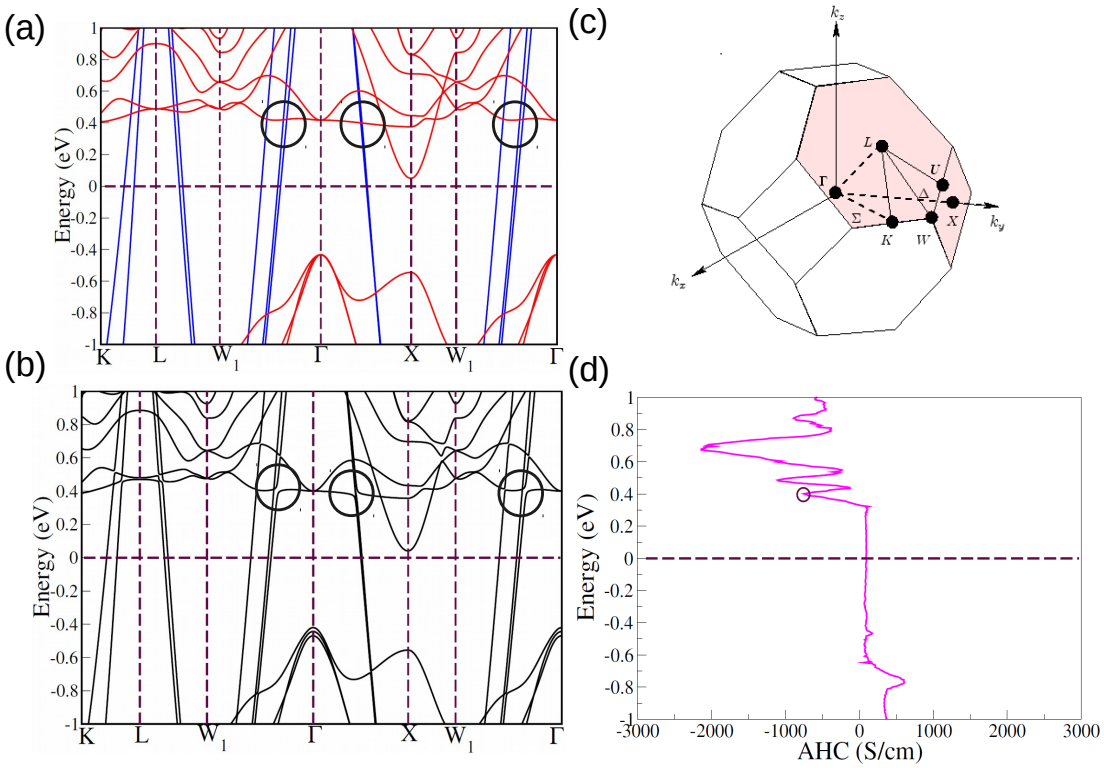

FIGURE 4.3: (a) The band structure of Co_2FeSi without SOC, with the nodal point above 0.38eV from the E_F indicated by the black circle. (b) The band structure of Co_2FeSi with SOC, with black circles denoting the gapped nodal lines. (c) The first bulk Brillouin Zone (BZ) of Co_2FeSi.High symmetry points are highlighted. (d) Energy (E-E_F) dependency of the AHC for Co_2FeSi, where the position of the gapped nodal line is indicated by the black circle. (at 0.38 eV of Energy).

4.4 Band topology

The electronic band dispersion is calculated using a plane wave-based pseudopotential in the presence and absence of SOC to understand the topological feature of the material and the Brillouin zone of the fcc lattice shown in Fig.4.3(c). The magnetization axis of the Co and Fe spins are set parallel to the z-axis [001]. The Co_2FeSi band structure along the high-symmetry paths of the BZ are depicted in Fig.4.3(a),(b) which shows the band structures without and with the SOC respectively. The blue and red curves represent the majority and minority bands and d orbitals of Co have a major contribution to the band near the E_F, and some of these bands have a small contribution from Fe d-orbitals. Linear band crossing points are observed along the Γ-W_1 and Γ-X high-symmetry points and

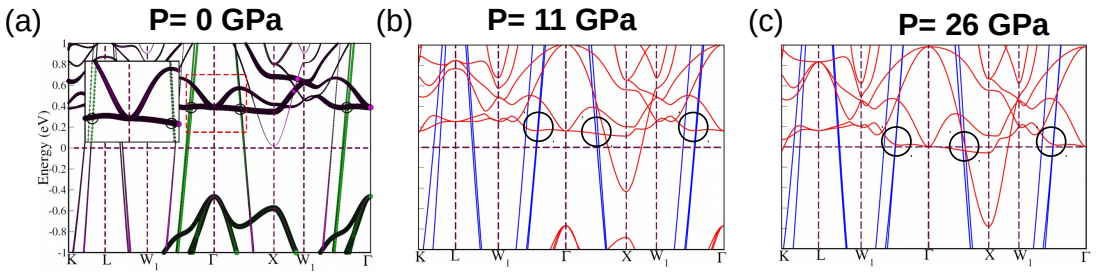

FIGURE 4.4: The band structure of Co_2FeSi with Hubbard U under various pressures in the absence of SOC. The nodal point is represented by black circles. (a) At P=0 GPa, the nodal point is 0.38 eV away from the E_F Whereas the green colour indicates that the t^{2g} orbital of Co is mostly responsible for extremely dispersive bands, the magenta colour indicates that flat bands are primarily contributed by the e_g orbital of Co. (b) At P=11 GPa, the nodal point is 0.25 eV above the E_F . (c) At P=26 GPa, the nodal point is located near the E_F.

these points are shown inside black circles. These points are approximately 0.38 eV above the E_F and form the NL-like band structure in the first BZ. The details of NL is analyzed in sec.4.5.

In 3d elements, the SOC has finite value and it plays an important role in transport properties, therefore we also calculate the electronic band structure in the presence of the SOC. In the presence of finite SOC, the spin and its S^z component are no longer conserved quantum numbers therefore, the spin-up and spin-down energy bands cannot be differentiated individually. The mixing of the spin-up and down bands breaks the degeneracy of the crossing point and opens a tiny gap as shown in Fig.4.3(b).

The experimental observation of the AHC of this material is shown to be mostly contributed from the extrinsic mechanism [225] and this is consistent with our calculations which show the presence of NL 0.38 eV above the E_F. We also explicitly calculate the intrinsic AHC as a function of E_F and notice that the value of AHC is close to zero at E_F as shown in Fig.4.3(d). In order to investigate the temperature-dependent anomalous Hall effect in Co_2FeSi, Mort et al. also noticed an extrinsic mechanism by observing skew scattering[228] at magnons. The value of AHC peaks at 0.38 eV above the E_F in Fig.4.3(d). This is expected due to the presence of the NL. There are two ways to achieve high AHC either by chemical

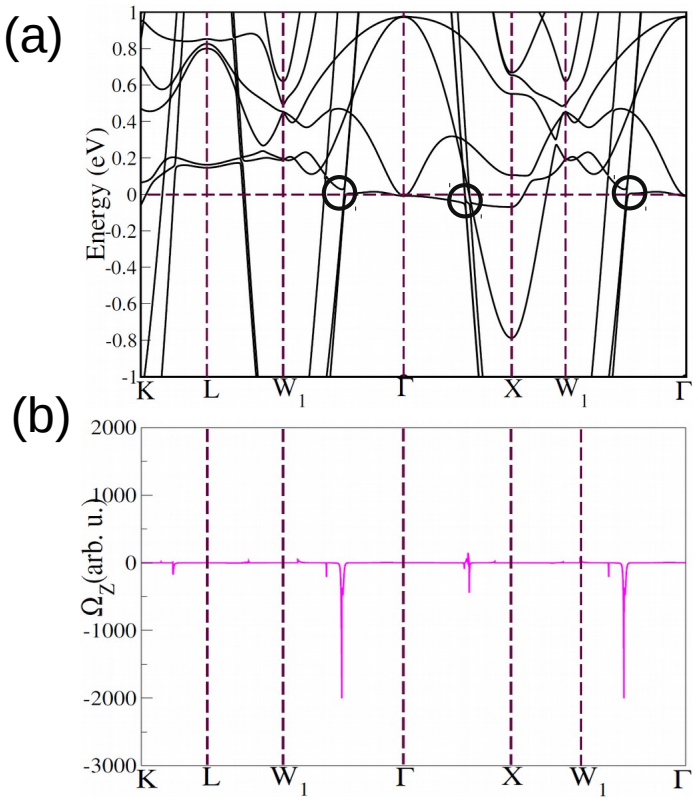

FIGURE 4.5: (a)The band structure of Co_2FeSi with SOC. black circles represent the gapped nodal line (b) The BC (Ω_z) at the nontrivial crossings along the high symmetry lines.

doping (doping electrons) to fill the band up to crossing points or by applying the pressure to bring down these crossing points near the E_F.

In this work, hydrostatic pressure is applied to explore the shift of the NL (the crossing points) towards the E_F. We notice that on increasing the pressure the minority spin DOS increases at the E_F, the half-metallic properties of the system are lost and the nodal point shifts towards the E_F as shown in Fig.4.4 (a),(b)and(c). By performing a fat band calculation, we can also determine the contribution of the d-orbitals to the electronic band structure. As can be seen in the inset of Fig.4.4 (a), the highly dispersive bands are primarily contributed by the t^{2g} (d^{xy},d^{yz},d^{xz}) orbitals of Co by the green filled circle, while the weakly dispersive flat bands are primarily contributed by the e_g (d^{z^2}, $d^{x^2-y^2}$) orbital of Co, as indicated by the magenta filled circle. A sharp peak in the DOS corresponds to the flat band shown in Fig.4.1(c). The band dispersion corresponding to the three pressures P = 0,

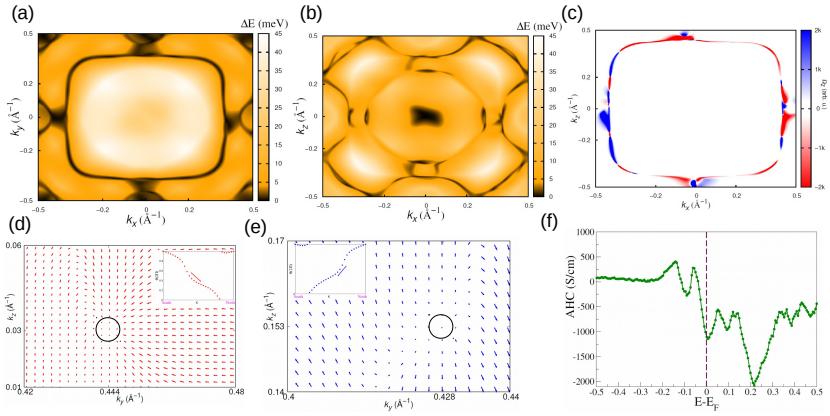

FIGURE 4.6: (a)Energy gap between two intersecting bands in the vicinity of E_F on the k_x-k_y plane, where the black rectangular closed line denotes the nodal line. (b)The nodal line is gapped out in the k_x-k_z plane, and the gap is represented by a white line. (c) The BC distribution is displayed in the k_x-k_z plane along the gapped nodal line. (d)For Co_2FeSi with SOC normalized BC is shown for Weyl point W_1 Source type (W_1+) which is indicated by the outward red arrow from the marked black circle; Average position of wannier charge centre corresponding to +1 chern number (e) Normalized BC behaves as Sink type (W_1-) which is indicated by the inward blue arrow marked black circle; Average position of wannier charge center corresponding to −1 chern number. (f) Energy (E-E_F) dependence of the AHC For Co_2FeSi

11, and 26 GPa are shown in Fig.4.4(a),(b), and(c) and the crossing points shift towards E_F are also shown in Fig.4.4(c).

TABLE 4.1: Lattice parameter of Co_2FeSi crystal at different pressure.

Pressure(Gpa)	a=b=c($\mathring{A}$)	$\alpha = \beta = \gamma$ (degree)
0	5.64	90
11	5.38	90
26	5.40	90

The application of the hydrostatic pressure changes the volume of the material and we change the lattice parameter a_0 from 5.64 $\mathring{A}$ to 5.40 $\mathring{A}$ as shown in Table 4.1. Previous study on the Heusler compound indicates that the compound is stable at high pressure[229–231]. Due to a decrease in the volume of the unit-cell atoms come close together and have a larger overlap between the atomic orbitals. We have also studied the Bader charge analysis to demonstrate how hydrostatic pressure alters atomic volume and influences charge transfer.

TABLE 4.2: Charge and Atomic volume of different atoms at P=0 Gpa of Co_2FeSi.

Atom	Charge	Atomic Volume
Co	9.3193	11.5261
Co	9.3211	11.5335
Fe	7.5020	10.0353
Si	3.8574	12.1873

TABLE 4.3: Charge and Atomic volume of different atoms at P = 26 Gpa of Co_2FeSi.

Atom	Charge	Atomic Volume
Co	9.5939	9.5960
Co	9.5905	9.5864
Fe	7.4964	7.8526
Si	3.3190	8.2256

The approximate minimum and maximum energy band dispersion can be written as $E_{\alpha,\sigma} \approx E_\alpha \pm 2Z_\alpha < t >$, where α and σ are orbital and spin index and Z_α is coordination number of α type orbital. According to the analysis of the tight-binding parameter obtained from Wannierization, for P=26 GPa the magnitude of hopping parameters are increased by approximately 50% (from 0.6 eV to 1.1 eV) while pressure squeezes the unit cell and it also increases the energy of the system, i.e the effective site energy of the system. Due to large Hund's interaction, the $E_{\alpha,\uparrow}$ has a lower energy than the $E_{\alpha,\downarrow}$ and when pressure is applied, the $E_{\alpha,\uparrow}$ and $E_{\alpha,\downarrow}$ change by around 27 % and 35 % respectively, i.e $E_{\alpha,\downarrow}$ of the Co band shift more as compared to $E_{\alpha,\uparrow}$. Therefore, the minority energy band (red) decreases more than the majority bands (blue) and the minority energy band has a lower degree of dispersion than the majority energy band as shown in Fig.4.4. Thus the interplay of enhancement of magnitude of the hopping parameter and relative change in the site energy $E_{\alpha,\downarrow}$ and $E_{\alpha,\uparrow}$ lead to a shift of the band crossing point near to the E_F.

In the presence of SOC at P = 26 GPa, we notice that the degeneracy of the crossing points is broken at E_F as shown in Fig.4.5(a). We also calculate the z-component of BC along the high-symmetry path and noticed that there are sharp

peaks of BC along the Γ-W_1 and Γ-X directions and negligible BC in the other directions which are shown in Fig.4.5(b). As a result, the BC distribution that surrounds the Fermi surface has a significant impact on the conduction electrons for our system, which we will examine extensively in sec.4.6.

TABLE 4.4: The Weyl points' positions, Chern numbers, and the energy relative to the E_F of Co_2FeSi.

Weyl points	k_x	k_y	k_z	Chern number	E-E_F
W_1	0.000	0.440	0.030	-1	0.000
W_1	0.000	0.420	0.155	+1	-0.050
W_2	-0.004	1.081	0.410	+1	0.062
W_2	0.005	-1.081	-0.416	-1	0.040
W_3	-0.013	-0.911	-0.006	+1	0.012
W_3	-0.010	0.910	-0.014	-1	0.021

4.5 Nodal Line and Berry curvature distribution

Co_2FeSi crystallizes in fcc lattice with the space group $Fm\bar{3}m$ and experimental magnetic measurements establish the half-metallic ferromagnetic nature of the ground state. The relevant symmetries in this system are the three mirror planes $M_x(k_x=0)$, $M_y(k_y=0)$, $M_z(k_z=0)$, and three C_4 rotation axes[217, 232] are k_x, k_y and k_z as shown in Fig.7.1(a). We present the results keeping the magnetization axis along the (001) in the presence of SOC. Only the $M_z(k_z=0)$ mirror symmetry and the C_{4z} rotational symmetry are preserved in the presence of a finite value of SOC, therefore, only the nodal line on the $k_z = 0$ plane will survive [232]. The other two NL on the $k_x = 0$ and $k_y = 0$ planes, on the other hand, are gapped out due to broken mirror symmetries.

The energy gaps are calculated in the first BZ in the presence of SOC shown in Fig.4.6(a) and Fig.4.6(b) for the k_z=0 and k_y=0 plane respectively. The persistence of mirror symmetries in the k_z=0 plane prevents the nodal line from gapping out, as shown in Fig.4.6(a). In the k_y=0 plane, NL opens a small gap (white region) except for some of the gapless weyl points as shown in Fig.4.6(b). There is a significant BC in the k_y=0 planes because of gapped NL. The distribution of

BC in the k_y=0 plane is depicted in Fig.4.6(c). Notably, these Weyl points are obtained from the NLs since at some k-points the NLs do not break out. Some of the Weyl points lie far from the E_F in the same plane and have finite BC, but their contribution to the AHC is small. Similar effects have also been observed in the k_x=0 plane as well.

The coordinates in k and energy E-E_F space of the Weyl points are listed in Table 4.4 along with their Chern numbers. The normalized BC corresponding to Weyl points in $k_x = 0$ plane is calculated to verify its existence as shown in Fig.4.6(d) and (c). We observe that BC is produced by the Weyl point with chirality + 1 as a source (outward flux in Fig.4.6(d)) and by the Weyl point with chirality -1 as a sink (inward flux in Fig.4.6(e)). High chern no additionally appear in multi-component systems[233–235]. We have also seen high chern nodes in our system. The Weyl charge centers (WCC) are calculated to verify the chirality of weyl points. Additionally, we also look into the Wilson-loop method for average WCC position as it is applied to a sphere that has these two nodes of opposing chirality. The inset of Fig.4.6(d) illustrates the average WCC shifting from north to south when the Chern number of W1 is positive, while the inset of Fig.4.6(e) illustrates the average WCC shifting from north to south when the Chern number of W1 is negative. We also carried out the same exercise for the other Weyl nodes. The major fraction of the AHC in the system is contributed by large BC near the gapped NLs. For this, we used Eq.3.1 and Eq.3.2 to calculate the AHC by integrating the Berry curvature of all occupied dispersion bands. The underlying space group with the magnetization along [001] direction contains the 4_{001} symmetry operation. Considering the symmetry properties of the BC shown in Eq.4.1 and summation of these Ωs over the BZ gives zero for x and y component due to their antisymmetric nature, and Ω_z sum has non-zero value [236]

$$\begin{aligned} -\Omega_x(k_x, k_y, k_z) &= \Omega_x(-k_x, -k_y, k_z) \\ -\Omega_y(k_x, k_y, k_z) &= \Omega_y(-k_x, -k_y, k_z) \\ \Omega_z(k_x, k_y, k_z) &= \Omega_z(-k_x, -k_y, k_z) \end{aligned} \tag{4.1}$$

4.6 Anomalous Hall effect

We notice that nearly degenerate bands close to the nodal line in the k_y=0 plane have large BC as shown in Fig.4.6(c) and contribute to the intrinsic AHC. Giant anomalous transport behavior may be caused by the large BC. To determine the AHC, we integrated the BC of the bands that were occupied across the entire BZ [Eq.3.1 and Eq.3.2]. Intrinsic AHC is calculated on a 301 × 301 × 301 k grid using maximally localized Wannier orbitals. The AHC have only z-component σ_z^A finite and the contribution of the x and y components σ^A vanish due to the odd nature of the BC. Fig.4.6(f) depicts the variation of AHC with Fermi energy. At the Fermi energy, we observed a giant intrinsic AHC (σ_z^A), which is about 1143 S/cm. The AHC value is comparable to the largest AHC observed in the Co_2MnGa [237] and much larger than the other compounds of the Heusler family [215, 238–240].

4.7 Summary

We theoretically study the magnetic and anomalous transport properties of Co_2FeSi, a Heusler compound using the ab-initio DFT calculations. In the electronic structure, three NLs arise due to the mirror symmetries in the $Fm\bar{3}m$ (space group no. 225) group of the material and NL gaps out along the direction of magnetization in the presence of SOC. The degeneracy at some of the k points remains intact and these points are Weyl points with specific Chern numbers.

We also observed the emergence of a substantial BC near the gapped NL, resulting in a significant AHC in our Heusler compound, particularly when the NLs are precisely positioned at or slightly below the E_F. In order to properly account for the magnetic and other electronic features, DFT+U calculations were essential. As a result, we found that the NL crossing point is moved at an energy level of 0.38 eV above E_F.Consequently, the AHC exhibited negligible contributions from the topological properties or NLs of the system, aligning with experimentally observed AHC properties [225]. To shift the NL positions closer to E_F, we applied

hydrostatic pressure to the material and studied the resulting changes in electronic properties. Intriguingly, at a pressure of 26 GPa, the NLs shifted to coincide with E_F, resulting in Co_2FeSi displaying a remarkable giant AHC ($\sigma_z^A = 1143$ S/cm), thereby transforming the system into an intrinsic topological metal. In conclusion, the mirror symmetries in this magnetic material with finite SOC play an important role in the emergence of NLs and Weyl points, and the finite hydrostatic pressure is crucial in tuning the position of NL near the E_F to have large intrinsic AHC which is an essential quality of a material for device applications.

Chapter 5

Flat band separation featuring a robust spin Hall Effect with nontrivial band topology in the presence of finite correlation in bilayer kagome

5.1 INTRODUCTION

The kagome lattice consisting of the vertices and edges of the trihexagonal tiling pattern, leads to geometrical frustration due to its corner-sharing triangles, making magnets composed of transition elements on this lattice captivating for their tendency to display correlated topological band structures [240–245]. The topologically protected quantum states found in strongly correlated systems, particularly on non-trivial geometries like the kagome lattice, hold significant promise for exploring exotic quantum phases[246, 247], with applications in diverse quantum technologies[167, 248–260]. The electronic band structure of the Kagome lattice

shows the destructive interference of Bloch wave functions which results in non-dispersive flat bands (FB)[244, 260–262], Dirac cone at high symmetry point K [263, 264] and van Hove singularity (VHS) at M point[265]. The instabilities near the flat band states have the potential to induce emergent novel phenomena, including ferromagnetism, high-temperature superconductivity, and the fractional quantum Hall effect[259, 266–271].

In recent decades, theoretical research in condensed matter systems has paid significant attention to the development of model Hamiltonians [272, 273]that describe the electronic structure of Kagome lattice in order to understand the emergence of these novel phases[274–276]. The spinless Haldane model is one of the most commonly employed models to understand the behavior of electronic structure in kagome lattices which incorporates spin-orbit coupling (SOC) and out-of-plane ferromagnetism [256]. It predicts the emergence of chern gap at Dirac points (DP)[243, 254], a phenomenon observed in various Kagome magnets. Recent experimental findings have corroborated the theoretical predictions, revealing spin-polarized Dirac cones with spin-orbit coupling-induced gaps in single-layer two-dimensional (2D) kagome materials such as Fe_3Sn_2[243, 277, 278] and $Co_3Sn_2S_2$[240, 279–281], as well as the manifestation of anomalous Hall effects in compounds such as Mn_3Sn and Mn_3Ge[282, 283] due to gigantic Berry curvature.

It is possible to envisage layer stacking of 2D Kagome materials forming bilayer three-dimensional (3D) Kagome materials. The AMn_6Sn_6(A=Li,Mg,Ca) family is such a set of bilayer 3D Kagome materials that have recently attracted considerable interest due to the exhibition of many interesting electronic properties like the presence of Chern-gapped Dirac fermions in $TbMn_6Sn_6$, which also demonstrates a ferrimagnetic order perpendicular to the kagome lattice plane. YMn_6Sn_6 [238, 284–286] exhibits an intriguing topological Hall effect near room temperature. However, the intriguing property of the emergence of the flat band is either not observed (Fe_3Sn_2, $Co_3Sn_2S_2$)[245, 250, 277] or far away from E_F (FeSn)[244]. The VHS and flat bands found in previously studied Mn-, Fe-, and Co-based kagome metals are typically situated far from the Fermi energy (E_F) in energy space. Unlike the model kagome lattice, the dispersion of the flat band in kagome compounds is modified

by additional factors, such as in-plane next-nearest-neighbour hopping, interlayer coupling, and multiple orbital degrees of freedom of transition metals. In the case of the rare-earth based AMn_6Sn_6 or related systems, atoms of the rare earth sit close to the Mn-Kagome layer and therefore influence the electronic band structure significantly [287]. Therefore, the experimental realization of the Kagome flat band requires careful and systematic material design. These complexities along with the interplay between electron correlation and topological features, pose challenges in detecting the FBs, saddle points, and Dirac fermions near the Fermi level (E_F) in magnetic Kagome systems.

In this chapter[1], we examine the bilayer 3D Kagome material $MgMn_6Sn_6$ consisting of two Kagome Mn single layers sandwiching the MgSn layer where non-magnetic Mg atom sits in the Sn plane and does not interact with Mn Kagome electrons. We notice from our minimal multiband Hubbard model that Sn atoms play a crucial role in determining the nature of magnetic exchange in the Mn layer. We use ab initio density functional theory (DFT) calculations to explore the electronic properties of $MgMn_6Sn_6$. The energy band structure of this system shows interesting properties: first, the Dirac point is located at the Brillouin zone (BZ) corner and just below the E_F. Second, at the $K_z = 0$ plane, there is a nodal line which open a narrow gap in the presence of SOC which also generates finite intrinsic Berry curvature along this line. It exhibits an intrinsic anomalous Hall effect (AHE) due to the non-trivial band topology, with an anomalous Hall conductivity σ_{xy}^{A} reaching a significant value of 500 S/cm. Another intriguing observation is the opening of a gap at the touching point of the quadratic band, emerging from the Dirac band, and flat bands in the presence of SOC. The nontrivial topology of the gapped-out flat band results in a finite spin Hall conductivity (SHC) and this is confirmed by calculating the Z_2 index. We also perform dynamical mean field theory (DMFT) calculations to include the effects of electronic correlations in the system and show that Curie temperature $T_c \sim 300$ K is consistent with the experiment.

[1]This chapter is based on "Flat band separation featuring a robust spin Hall Effect with nontrivial band topology in the presence of finite correlation in bilayer kagome metal" - J.Sau*, H.Banerjee, S.Saha, N.Kumar, and M.Kumar

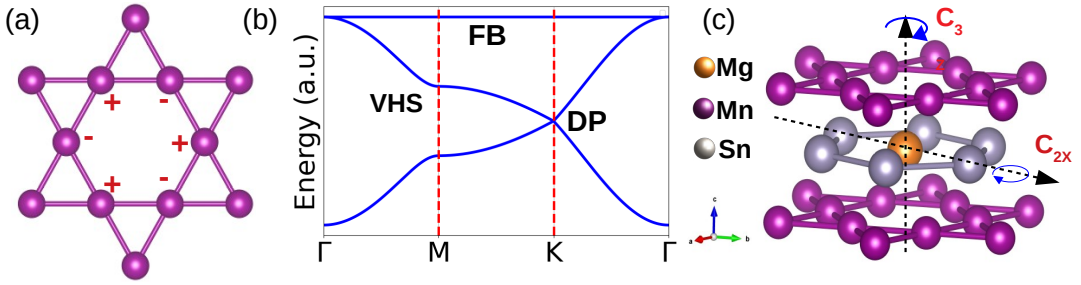

FIGURE 5.1: (a) structure of kagome lattice and a quenched eigenstate induced by destructive interference. (b) The band structure of electronic kagome lattice without SOC, with NN interaction dominating the in-plane hopping process. (c)The kagome metal's three-fold (C_{3z}) rotation-axis symmetries are when the two kagome layers sandwich the hexagonal Sn layer.

5.2 Crystal Structure

We first describe the crystal structure of the chosen material $MgMn_6Sn_6$. The Kagome compound $MgMn_6Sn_6$ possesses a hexagonal structure, falling within the space group *P6/mmm*, with lattice parameters of a = b = 5.517 Å and c = 9.032 Å. It comprises of double Mn Kagome lattice layers parallel to the ab plane, with a honeycomb lattice of Sn atoms.

Computational Details

DFT Calculations: Our computational approach utilized the Vienna ab initio simulation package code, employing density functional theory (DFT). The generalized gradient approximation (GGA) was employed to approximate the exchange-correlation functional. We conducted first-principles calculations incorporating an effective Coulomb-exchange interaction U_{eff} (U-J), where U and J represent the Coulomb and exchange parameters, respectively. To address the high electronic correlation effect of the Mn 3d electrons, we included an onsite Coulomb interaction parametrized with a Hubbard U_{eff} = 3.0 eV [288]. The cutoff energy for expanding the wave functions into the plane-wave basis remained constant at 550 eV throughout the project. We utilized the Monkhorst-Pack scheme to sample the Brillouin zone in k-space for computations. The equilibrium structure served as

the basis for the k-mesh, which was set at 10×10×6. The intrinsic Hall conductivity (σ_{xy}^{int}) was computed by integrating the z-component of Berry curvature (Ω^z) over all occupied states across the Brillouin zone, with spin-orbit coupling (SOC) taken into account.

DFT+DMFT Calculations: For our DFT+DMFT calculations we are using the full-potential augmented plane-wave basis as implemented in the WIEN2K code package.[289] For the WIEN2K calculations, we used the largest possible muffin-tin radii, and the basis set plane-wave cutoff was defined by $R_{\min} \cdot K_{\max} = 10$, where $R_{\min}$ is the muffin-tin radius of the O atoms. The consistency between the VASP and WIEN2K results has always been cross-checked. DMFT calculations were performed using the TRIQS/DFTTools package [290–292] based on the TRIQS libraries[293]. Projective Wannier functions as implemented in the DMFTPROJ module of TRIQS were employed to crosscheck the results and also to calculate the initial occupancy of the correlated orbitals. All five Mn d orbitals have been taken into account in the correlated subspace. A projection window of $-12\,\text{eV}$ to $+20\,\text{eV}$ was chosen to take into account any hybridisation and charge transfer effects. The Anderson impurity model constructed by mapping the many-body lattice problem to a local problem of an impurity interacting with a bath was solved using the continuous-time quantum Monte Carlo algorithm in the hybridization expansion (CT-HYB)[294] as implemented in the TRIQS/CTHYB package[295]. For each DMFT step, 1280000 cycles of warmup steps and 128000000 cycles of measures were performed for the quantum Monte Carlo calculations. We performed one-shot DFT+DMFT calculations, using a fully localised limit (FLL) type double-counting correction[296]. We use a fully rotationally-invariant Kanamori Hamiltonian parametrised by Hubbard U and Hund's coupling J_H, where we set the intraorbital interaction to $U' = U - 2J_H$. For our DMFT calculations, we used U value of $6\,\text{eV}$ and $J_H = 0.5\,\text{eV}$. The choice of U and J for DMFT calculations has been motivated by previous studies on Manganites excellent agreement between DMFT and experimental ARPES band structure, as well as band gaps, and T_N have been demonstrated for a similar range of U and J_H values as well as prediction of experimental properties driven by correlations.

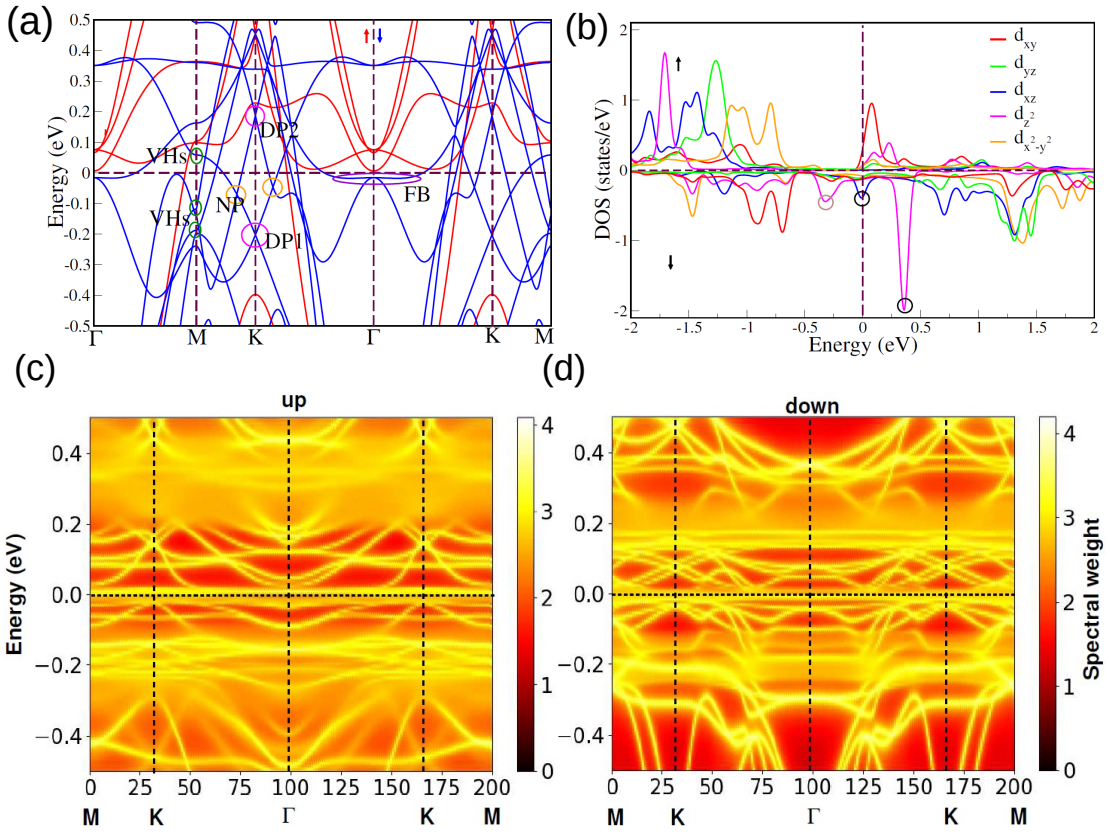

FIGURE 5.2: (a) The band structures, excluding spin-orbit coupling (SOC), depict majority and minority spin carriers with red and blue curves, respectively. Notable features such as the flat band (FB1), Dirac points (DP1 and DP2), saddle points (SP1), and Weyl points are denoted by maroon, magenta, green, and orange circles, respectively. (b) The DOS of different d-orbitals of the Mn atom displays a metallic character. The peak in the Minority dos is attributed to FB1, FB2, and SP. (c),(d) Figure showing DMFT bands at β=150eV^{-1} for the K path M-K-Γ-K-M. This figure shows the effect of incoherent scattering due to dynamic correlation effects at finite temperature on the band structure in the spin-polarised state while maintaining the same features of the bands as observed with 0K DFT.

[297–299] Real-frequency spectra and real-frequency self-energy for band structure have been obtained using the maximum-entropy method of analytic continuation as implemented in the TRIQS/MAXENT application.[300]

5.3 Ab initio Electronic Structure

The electronic band structure of a single-orbital kagome lattice (see Fig.5.1(a)) in the tight binding paradigm is initially explored, as illustrated in Fig.5.1(b). In this

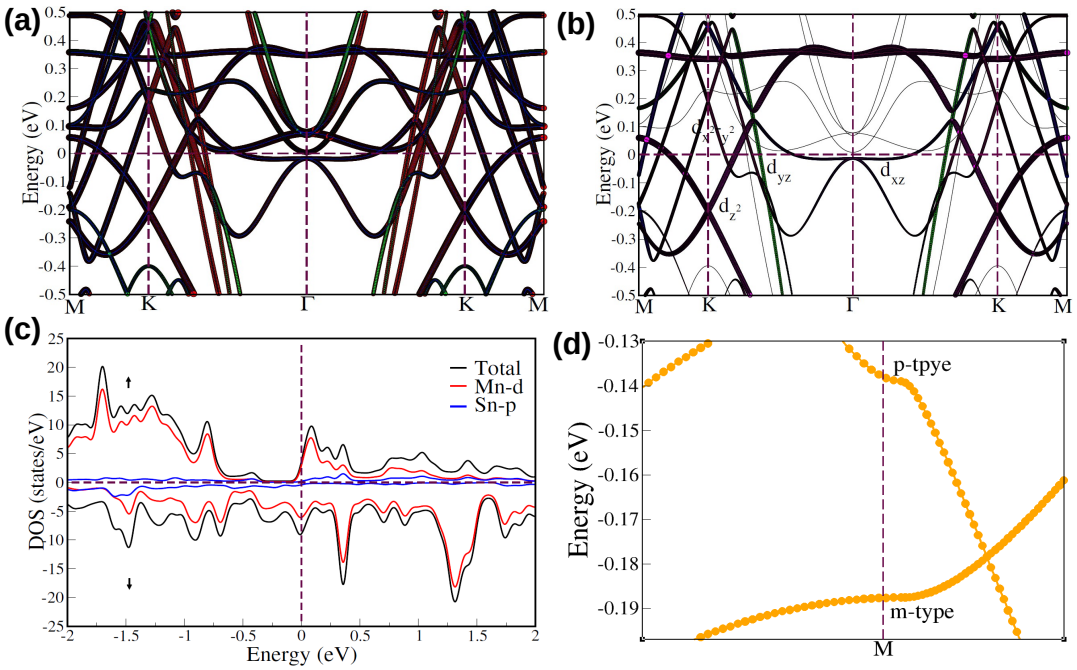

FIGURE 5.3: (a)Mn, Sn, and Mg's projected orbital contributions to the band dispersion in $MgMn_6Sn_6$. (b) Projected d-orbital contribution of Mn in the band dispersion in $MgMn_6Sn_6$. (c)The total DOS of $MgMn_6Sn_6$ is represented by the black curve, and the dos of Mn-d and Sn-p are represented by the red and blue curves, respectively. (d) P-type and m-type VHS at the M point for $MgMn_6Sn_6$

limit, the flat band emerges alongside a pair of Dirac cones and VHS which arise due to the fact that the honeycomb lattice and the Dirac points are protected by lattice symmetry [263–265]. The flat band arises due to the destructive interference of electron wavefunction and the phase of the wavefunction at different atoms at the hexagons as shown in Fig.5.1(a) [301].

$MgMn_6Sn_6$ is a more complex system where the honeycomb Sn layer is sandwiched between two Kagome layers, ensuring that all relevant symmetries are preserved, as depicted in Fig.5.1(c) and this requires a first principles approach for the calculation. Let us then analyze the electronic band dispersion of our system where the spin-up and -down bands are shown in blue and red colour (see Fig.5.2(a)) as obtained from PBE+U calculations. These bands exhibit linear crossings points near the Fermi energy (E_F) without SOC and it is shown in K_z=0 plane along Γ-M-K-Γ-K-M, illustrated in Fig.5.2(a).

The first striking feature in the band structure is the presence of Dirac cones with linear dispersion that are observed at the corner points K and K′ of the Brillouin zone, owing to the protection provided by two-fold and three-fold rotational symmetries (C_{2x} and C_{3z}, respectively) of the Kagome layer, as depicted in Fig.5.1(c). The magenta circle in Fig.5.2(a) highlights the location of the band's Dirac point1 (DP1) at the K point, situated approximately 0.25 eV below E_F. Orbital-projection band calculations indicate that the Dirac point primarily originates from the out-of-plane Mn d_{z^2} orbital (magenta), as illustrated in Fig.5.3(b). Another linearly dispersing Dirac point 2 (DP2), indicative of the band structure arising from the kagome lattice, is identified at the K point, situated approximately 0.19 eV above E_F, created by the Mn atom's d_{z^2} and $d_{x^2-y^2}$ orbitals. Furthermore, we have illustrated the constant energy contours at DP1 and DP2, revealing the distinctive hexagonal symmetry of the kagome lattice. Additionally, a circular electron pocket is identified near the center of the Brillouin zone (Γ), as depicted in Fig.5.4.

Next, we observe in Fig.5.2(a) a degenerate crossing point positioned below the E_F, marked by an orange circle, which is identified as a Weyl point. Further detailed analysis of this observation is provided in Sec.5.6. Additionally, a linear band crossing point is noted along the high-symmetry *M*-*K* direction at the E_F, denoted by a black circle in Fig.5.2(a), which forms the nodal-line-like band structure in momentum space. Sec.5.6 will provide a specific analysis of these nodal lines in more detail.

We also observe the presence of VHS in the energy dispersion of the tight-binding model on the Kagome lattice, as illustrated in Fig.5.1(b). In $MgMn_6Sn_6$ exhibits two types of VHS with opposite concavities: the m-type VHS which demonstrates an upward energy shift as the band approaches the M point and the p-type VHS which exhibits a downward energy shift as the band approaches the M point as shown in Fig.5.3(d). Additionally, this VHS phenomenon signifies a divergence in the density of states (DOS), as illustrated in Fig.5.2(b).

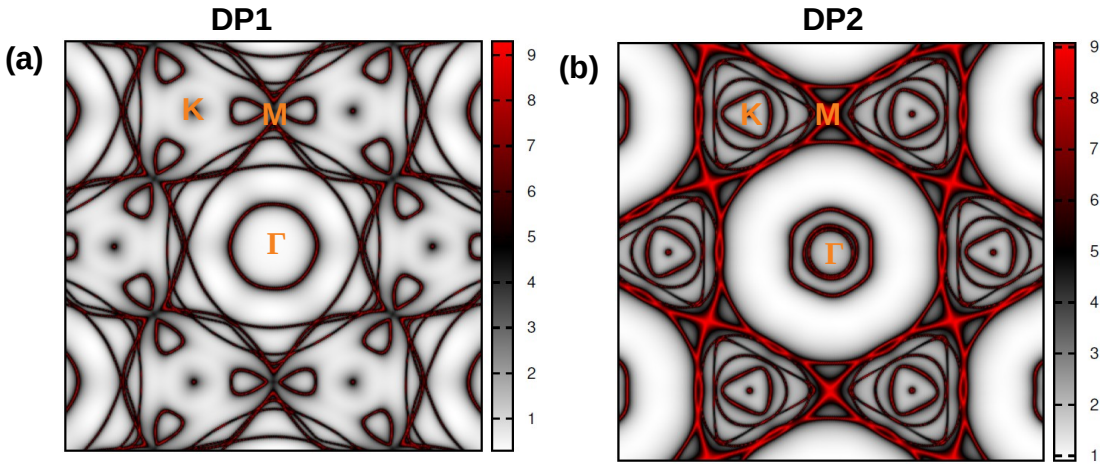

FIGURE 5.4: a) Constant energy contour (CEC) at $K_z = 0$ plane estimated by DFT at DP1 (b) Constant energy contour (CEC) at $K_z = 0$ plane estimated by DFT at DP2

Finally, the most important observation in the band structure of $MgMn_6Sn_6$ is the flat band(FB) which has d_{xz} and d_{yz} orbital character of Mn atoms. This FB feature appears along the $\Gamma - K$ direction at 0.04 eV below E_F. The dispersion of the FB in this material may be influenced by many factors beyond spin-orbit coupling, such as in-plane next-nearest-neighbor hopping, interlayer coupling, or multiple orbital degrees of freedom as discussed in Sec.5.4.

Next, we move on to analyze the partial density of states (PDOS) of Mn atoms near the E_F and notice that the major contribution to the DOS comes from d-orbitals of the Mn as shown in Fig.5.2(b). The peak in the DOS in the minority spin channel marked by the black circle (Fig.5.2(b)), confirms that the Mn minority spin channels are responsible for the formation of FB. At the Γ point, a quadratic band (QB) emerges from the Dirac band (DP2) and touches the FB, as depicted in Fig.5.2(a). This touching point remains robust against perturbations except for SOC. Further details on the tight-binding calculation can be found in Sec.5.4. Both the flat band and the quadratic band are primarily composed of d_{xz}/d_{yz} orbitals of Mn, as illustrated in Fig.5.3(b).

Further investigation of the robustness of this touching point requires exploration of the impact of dynamic correlations and finite temperature effects on the band dispersion which are completely missed by standard DFT+U calculations. We

have conducted this analysis by DFT+DMFT calculations. In contrast to DFT+U which represents a static correlation energy correction without frequency dependence DFT+DMFT includes both static and dynamic correlation effects within the frequency dependent self energies. Utilizing continuous-time Quantum Monte Carlo (QMC) solvers within hybridization expansion, we simulate the influence of temperature. We observe the effect of dynamic correlations through the finite frequency self-energy and utilize this self-energy to compute momentum- and energy-resolved correlated spectral functions, as illustrated in Fig.5.2(c),(d). These spectral functions represent a DMFT band structure incorporating both correlation effects from the self-energy and finite temperature effects, providing a direct comparison with ARPES. Additionally, we simulate the ARPES band structure of the bulk material, which directly corresponds to the observations with DFT+U. We find a significant impact of electron scattering on the band structure, as expected at finite temperatures. This scattering predominantly exhibits incoherent scattering characteristics, evident from the large values of Im Σ for $\omega \to 0$ (frequency (ω)-dependent dynamic self-energy). This behavior aligns with previous findings in near half-filled manganites [298] and other strongly correlated materials [302]. While dynamic correlations and finite temperature effects introduce some mass renormalization, the features observed at 0K remain preserved.

5.4 Tight-binding model

We consider nearest and next-nearest neighbor hopping on a kagome lattice with spin-orbit interactions, represented by the following Hamiltonian:

$$\begin{aligned} H = &-t_1 \sum_{\langle i,j\rangle\sigma} c^\dagger_{i\sigma} c_{j\sigma} + i\lambda_1 \sum_{\langle i,j\rangle\alpha\beta} (\mathbf{E}_{ij} \times \mathbf{R}_{ij}) \cdot \boldsymbol{\sigma}_{\alpha\beta} c^\dagger_{i\alpha} c_{j\beta} \\ &-t_2 \sum_{\langle\langle i,j\rangle\rangle\sigma} c^\dagger_{i\sigma} c_{j\sigma} + i\lambda_2 \sum_{\langle\langle i,j\rangle\rangle\alpha\beta} (\mathbf{E}_{ij} \times \mathbf{R}_{ij}) \cdot \boldsymbol{\sigma}_{\alpha\beta} c^\dagger_{i\alpha} c_{j\beta} \end{aligned} \tag{5.1}$$

where $c^\dagger_{i\sigma}$ creates an electron with spin σ on the site $\mathbf{r}_i$ on the kagome lattice. Here $\langle i,j\rangle$ denotes nearest neighbors and $\langle\langle i,j\rangle\rangle$ next-nearest neighbors. The second

and fourth terms describe spin-orbit interactions which preserve time-reversal invariance. $\mathbf{R}_{ij}$ is the distance vector between sites i and j and $\mathbf{E}_{ij}$ the electric field from neighboring ions experienced along $\mathbf{R}_{ij}$.

We first study just nearest-neighbor hopping so $t_2 = \lambda_2 = 0$. In momentum space, Eq.5.1 becomes

$$H(\mathbf{k}) = -2t_1 \begin{pmatrix} 0 & \cos k_1 & \cos k_2 \\ \cos k_1 & 0 & \cos k_3 \\ \cos k_2 & \cos k_3 & 0 \end{pmatrix} \pm i2\lambda_1 \begin{pmatrix} 0 & \cos k_1 & -\cos k_2 \\ -\cos k_1 & 0 & \cos k_3 \\ \cos k_2 & -\cos k_3 & 0 \end{pmatrix} \tag{5.2}$$

where $\mathbf{a}_1 = \hat{x}$, $\mathbf{a}_2 = (\hat{x} + \sqrt{3}\hat{y})/2$, $\mathbf{a}_3 = \mathbf{a}_2 - \mathbf{a}_1$, and $k_n = \mathbf{k} \cdot \mathbf{a}_n$. We use units where the hopping parameter $t_1 = 1$ and $\lambda_1 = 0.01$. The $+$ $(-)$ sign refers to spin-up (down) electrons; from here we focus on just the spin-up electrons.

For a more realistic scenario, we next include second-nearest neighbor hopping. This gives us additional terms in the Hamiltonian:

$$\begin{aligned} H(\mathbf{k}) = &-2t_2 \begin{pmatrix} 0 & \cos(k_2 + k_3) & \cos(k_3 - k_1) \\ \cos(k_2 + k_3) & 0 & \cos(k_1 + k_2) \\ \cos(k_3 - k_1) & \cos(k_1 + k_2) & 0 \end{pmatrix} \\ &+i2\lambda_2 \begin{pmatrix} 0 & -\cos(k_2 + k_3) & \cos(k_3 - k_1) \\ -\cos(k_2 + k_3) & 0 & -\cos(k_1 + k_2) \\ \cos(k_3 - k_1) & -\cos(k_1 + k_2) & 0 \end{pmatrix} \end{aligned} \tag{5.3}$$

We use units where the hopping parameter $t_2 = 0.3$ and $\lambda_2 = 0.008$.

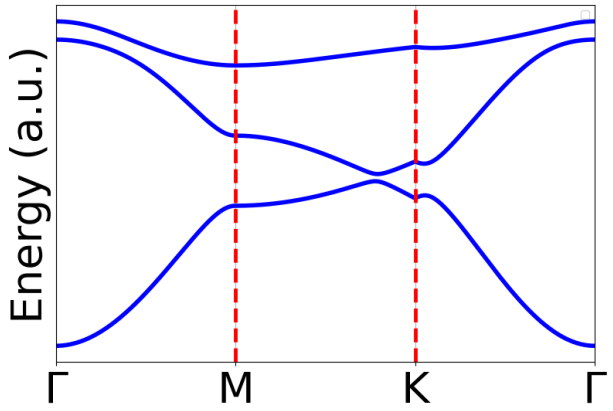

FIGURE 5.5: Dispersion of energy bands in the presence of spin-orbit coupling (SOC) with second-nearest neighbor hopping.

5.5 Model

Next, we intend to determine the magnetic ground state with many-body methods exploring all possible configurations state of the chosen material. To build an effective model, we examined the total DOS and atomic projected band structure, confirming the crucial role played by the d-orbitals of Mn and the p-orbitals of Sn in shaping the energy band dispersion near E_F. This observation is illustrated in Fig.5.3(a). In the total density of states (DOS), the spin-up DOS exhibits a lower value at the E_F compared to the minority carrier, while the spin-up DOS shows a higher value at low energy. This indicates the localization of the spin-up d-orbital of Mn. The local moment of Mn is measured to be 2.3 μ_B/f.u., which is consistent with experimental measurements [303]. The Bader charge analysis suggests that the d orbitals of Mn are half-filled. Similarly, in Sn, the p orbitals are also half-filled, with one electron residing in each orbital.

All the d-orbitals of Mn are equivalent, and similarly, the three p-orbitals of Sn are also equivalent. therefore, we construct a minimal multi-band Hubbard model which includes only two d-orbitals of Mn and one p-orbital of Sn to study the emergence of the magnetic ground state (gs) in the relevant parameter space.

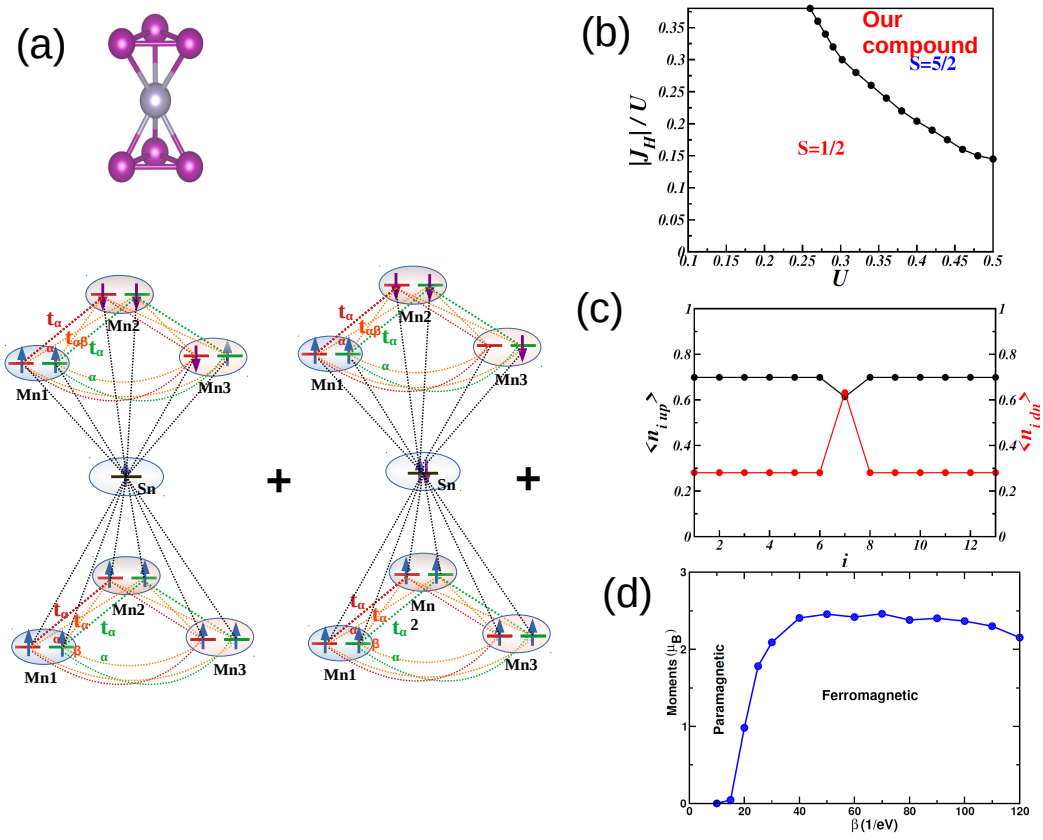

FIGURE 5.6: (a) The unit cell of a bi-layer Kagome structure featuring one Sn atom, along with the predominant configurations in the ground state wave function. (b) The average charge density for up spin and down spin within the unit cell, where the black curve represents the up spin charge density and the red curve represents the down spin charge density. (c) The phase diagram for the unit cell as U is varied with J_H/U. (d) The evolution of magnetic states as a function of temperature.

We use the multiband Hubbard model

$$H = \sum_i H_i^{int} + \sum_{<ij>} H_{ij}^{tb}, \tag{5.4}$$

where H_i^{int} represents the interaction term on i^{th} site and can be written as:

$$\begin{aligned} H_{int} = &\sum_{i,\alpha} U_i n_{i\uparrow\alpha} n_{i\downarrow\alpha} + \sum_{i,\alpha<\beta} (U_i' - \frac{J_{i,H}}{2}) n_{i\alpha} n_{i\beta} \\ &-2 \sum_{i,\alpha<\beta} J_{i,H} \mathbf{S}_{i\alpha}.\mathbf{S}_{i\beta} + \sum_{i,\alpha} \Delta_{i,\alpha} n_{i,\alpha} \quad . \end{aligned} \tag{5.5}$$

The first two terms are the intra and inter-orbital Hubbard interaction at i site. The third term is the inter-orbital Hund's coupling between spins at site i. U_i, U_i'

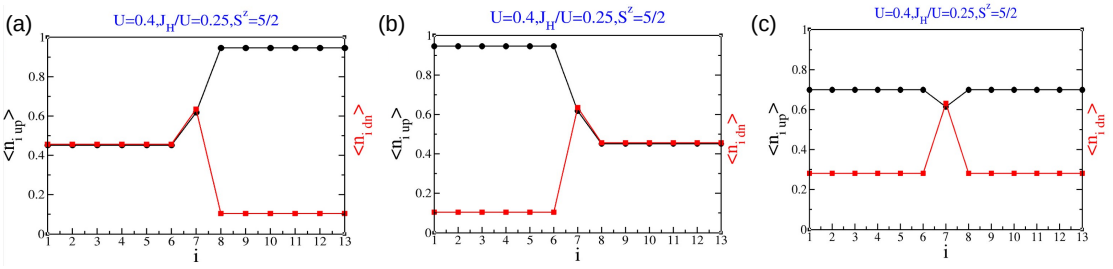

FIGURE 5.7: (a) and (b) corresponds to the up and down spin charge densities for all the orbitals of each site, which we have taken in our ED calculation, for two degenerate ground state wave functions respectively. (c) Average up and down spin-charge density for these two degenerate wave functions.

and $J_{i,H}$ are the usual Kanamori parameters for ith site and we use the standard relation $U_i' = U_i - 2J_{i,H}$. For Mn, we assumed the Coulomb interaction, U, and the Hund's coupling, J_H as 0.4 and 0.25 respectively[304]but in the case of Sn, these parameters are taken to be 0. $\Delta_{i,\alpha}$ represents the chemical potential for the α orbital of ith site. For the Sn atom, it is -1.5 eV and for the e$_g$ orbitals of Mn, it is taken as 0 eV, as suggested by Wannier calculation. Now, the tight binding part of the Hamiltonian is written as

$$H_{tb} = \sum_{\sigma,\alpha,\beta} t_{i,j,\alpha,\beta}(c^{\dagger}_{i\sigma\alpha}c_{j\sigma\beta} + H.c.), \tag{5.6}$$

where, $t_{i,j,\alpha,\beta}$ is the hopping strength between the orbital α of i-th site and orbital β of j-th site. $c^{\dagger}_{i\sigma\alpha}$ is the creation operator of an electron with spin σ, orbital α, at site i whereas, $c_{j\sigma\beta}$ is the annihilation operator with the same spin at site j, orbital β . The hopping interaction is restricted to the two d orbitals of different Mn atoms and one p orbital of Sn. The hopping matrix element of $t^{Mn-Mn}_{\alpha-\beta}$ and t^{Mn-Sn}_{α} are given in the appendix. We solve this Hamiltonian, given in eq. (1) in many body basis using exact diagonalization (ED) technique.

We consider a unit cell of the system as depicted in Fig.5.6(a), and this cell includes six Mn atoms and one Sn atom, where each Mn atom possesses two orbitals and two electrons, and the Sn atom possesses one orbital and one electron.

The ground state is twelve-fold degenerate (6×2)with S=5/2, where six arise from

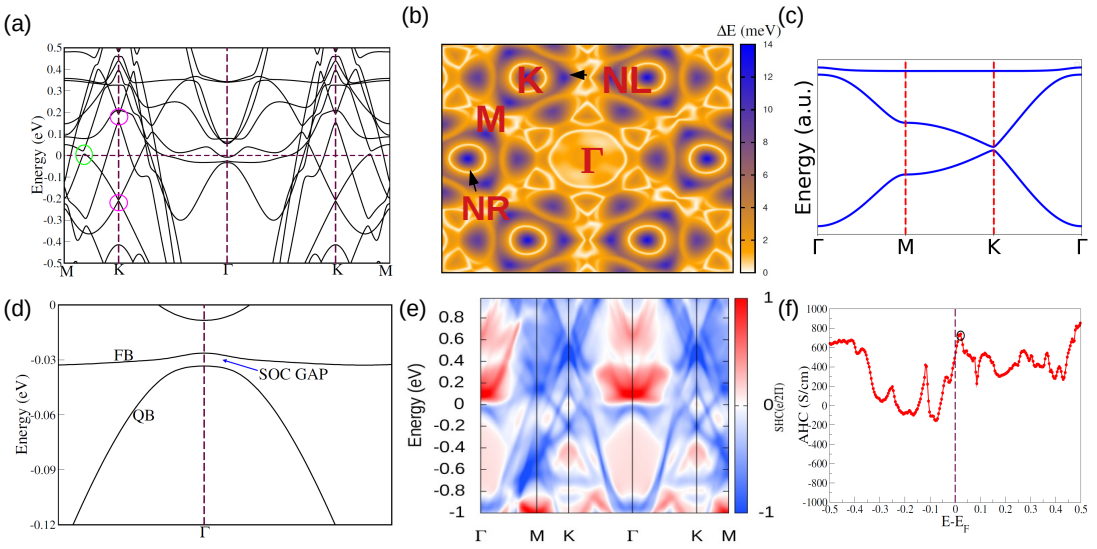

FIGURE 5.8: (a) The band structure of $MgMn_6Sn_6$ with SOC. (b) The energy gap between two crossing bands at the Fermi level (EF) is shown, with the nodal ring (NR) around the high-symmetry point K marked by a white line. The gapped-out nodal line (NL) is indicated by a violet circle, and the gap Dirac point is represented by a blue section at the K point.(c) Tight binding band structure in the presence of SOC. (f)The gap between the QB touching and the FB at the Γ point in the presence of SOC. (d) The spin Hall conductivity (SHC) of $MgMn_6Sn_6$ varies with high symmetry points. Integration of in-plane momentum contributions up to a certain energy reveals a significant enhancement of SHC within the nontrivial SOC gap between the flat and Dirac bands (e) The AHC's energy (E-E_F) dependence For $MgMn_6Sn_6$, the gapped NL position is indicated by the black circle.

spin degeneracy (2S+1=6; S=5/2) and two from orbital degeneracy(due to configurational symmetry). In Fig.6.3(a), we illustrate the two most dominant configurations in the ground state wave function. The first configuration demonstrates that all orbitals of each atom are singly occupied due to the onsite Coulomb repulsion (U). In the lower layer (LL) of Mn atoms, spins tend to align in the same direction due to the large Hund's coupling (J_H), whereas in the upper layer (UL), spins of two Mn atoms align in the same direction, while the spins of another Mn atom align in the opposite direction due to the antiferromagnetic exchange developed between the hoping of the electrons in Mn orbitals to nearest Mn orbitals and triangular geometry lead to frustration. However, the Sn electron is in a down spin configuration due to the large hopping between Mn and Sn. Another dominant configuration maintains ferromagnetic coupling in the LL triangle of Mn, similar to the first configuration, but one electron from the d-orbital of the Mn-orbital is

transferred to the Sn site making it double occupied. Consequently, Sn exhibits an effective zero magnetic moment.

The stability of the S=5/2 magnetic gs state is examined by constructing a phase diagram, where we varied the parameters U and J_H/U of the Mn atom. This diagram is shown in Fig.5.6(c). It is observed that by varying U for a fixed J_H/U, the gs system goes from an S=1/2 state to an S=5/2 state. Further details of the S=1/2 magnetic gs are discussed. The $S^z = 5/2$ state of the gs shows two fold orbital-degeneracy and the corresponding up and down spin charge densities are shown in Fig.5.7(c). We calculated average spin-resolved charge densities(see Fig.5.6(b)), revealing effectively positive spin densities for each orbital of Mn sites $\rho(Mn)$=0.698, while Sn sites exhibit effectively zero spin density and the per site spin density for Mn for all five orbitals $\rho_S^t = 1.15$ which is consistent with DFT predictions. This ferromagnetic ground state is also observed in rare earth bi-layer compounds such as RMn_6Sn_6 (where R = Li, Mg, Ca, Tb, Ho, Er, Tm, Lu, and Dy).

Finally, we examine the evolution of the magnetic states with temperature using DMFT calculations, as illustrated in Fig.5.6(d). Initially, at high temperatures, a paramagnetic state is observed. As the temperature is reduced, ferromagnetic ordering begins to emerge around $\beta = 20eV^{-1}$ (corresponding to T=580K), reaching a saturation magnetization of approximately $2.45\mu_B$ at $\beta = 40eV^{-1}$ (T=290K), which aligns excellently with experimental findings.

5.6 Influence of SOC

Topological properties are highly sensitive to spin orbit coupling (SOC) effects, in this next section, we explore the impact of the SOC on the band dispersion resulting from the transition metal atom Mn. Mn, with its significant SOC, is anticipated to have a substantial impact, particularly on the degenerate points, due to the mixing of up and down spin channels. From the tight-binding model, we have also noticed that with the coefficient of SOC even at 1/100th of the nearest

neighbor hopping, the degenerate points are gapped out at K and Γ. When we incorporate the second nearest neighbor hopping, the degeneracy breaks even at low SOC values, as indicated in Sec.5.4. On examination of the electronic band structure in the presence of SOC, we find that the DP1 at the K point exhibits a tiny bandgap opening (13 meV) in the presence of SOC, as shown Fig.5.8(b). We have represented the energy gap where violet spots at the K points represent the gap at DP1 as shown in Fig.5.8(a)and this non-trivial Dirac fermion resides in the occupied state and is located closer to the E_F, contributing significantly to the Berry curvature (BC), depicted by a red spot in Fig.5.9(a). Moreover, another crossing point, DP2 at the K point, exhibits a wider bandgap opening (42 meV) in the presence of SOC. However, since it is distant from the E_F, it will not impact the electron conduction. Nevertheless, by doping electrons into the system, we can access this larger gap.

In sec.5.3 we have pointed out the degenerate point that is forming the Nodal Line (NL). The NL loops in the $k_z = 0$ and $k_z = \pi/c$ planes are protected by the M_x mirror[217] symmetry and these NLs in the Γ-K-H-A plane that links them. The six-fold rotational symmetry results in six NL and NL loops symmetrically distributed near the K and L points. However, due to the finite magnetization in the system, the time-reversal symmetry is broken, leading to the NLs beginning to gap out in the presence SOC, although the gap size remains small (< 14 meV) which is shown in the Fig.5.8(a). We have illustrated the energy gap of the NL in the K_z=0 plane in Fig.5.8(b), where a violet circle centered at K denotes this gap. This gap induces a significant Berry Curvature (BC) along this line, as depicted by a red speck in Fig.5.9(a).

Another crossing point, indicated by an orange circle, remains ungapped even in the presence of SOC, as depicted in Fig.5.8(a). The energy gap in the k_x-k_y plane is illustrated in Fig.5.8(b), where the white circular ring surrounding the K point forms the nodal ring (NR), forming Weyl points at certain k-points in momentum space. We have listed the Weyl points in Table 5.1 and also computed the normalized BC enclosing the coordinates of the points in the $k_z = 0$ plane. It is noted that the BC is produced by the Weyl point with chirality +1 as a source

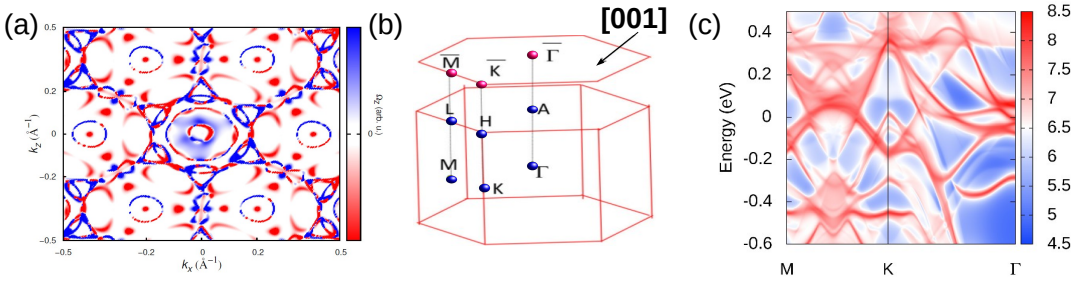

FIGURE 5.9: (a) Berrycurvature distribution in K_x-k_y plane. (b) Brillouin Zone with high symmetry point (c) display the surface band dispersion for the slab (001).

and by the Weyl point with chirality -1 as a sink. We performed the same analysis for the other Weyl nodes and confirmed their chirality.

TABLE 5.1: The Weyl points' positions, Chern numbers, and the energy relative to the E_F of $MgMn_6Sn_6$.

Weyl points	k_x	k_y	k_z	Chern number	E-E_F
W_1	0.188	0.294	0.0009	-1	-0.05
W_1	-0.239	0.147	0.00002	1	-0.08
W_2	-0.105	-0.060	-0.0005	1	-0.065
W_2	-0.188	0.056	0.0003	-1	-0.083
W_3	-0.05	-0.164	0.0009	1	-0.1
W_3	-0.007	0.121	0.00009	-1	-0.12

In our investigation, we explored the impact of the SOC on the touching point of the quadratic band and FB, as illustrated in Fig.5.8(c) from the tight-binding calculation in the presence of SOC with nearest neighbour hopping. We observed a gap opening at the contact point at Γ as well as at the Dirac point which we have already discussed.

The gap at the contact point of these two bands in $MgMn_6Sn_6$ measures 20 meV as shown in Fig.5.8(d), which is smaller than the gap observed at the linear band crossing of Fe_3Sn_2 (30 meV), yet FB and band touching is near Fermi compared to other systems. Wherein it is located far from the E_F. The SOC induced gap strongly suggests that the reported flat band at $k_z = 0$ has a nontrivial structure, endowing nonzero Z_2 invariant under the time-reversal breaking condition. To derive the Z_2 index,the parities of the occupied bands at the time-reversal-invariant (TRI) moments are analyzed and six sets of Z_2 numbers were computed for them.

If the system is in a Z-trivial state, this index will be even, and if not, odd. The Z_2 calculations of the six TRI planes can be utilized to obtain the Z_2 topological indices (ν_0, $\nu_1\nu_2\nu_3$) using the formula:$\nu_0 = (Z_2(k_i = 0) + Z_2(k_i = 0.5)) \mod 2$ and $\nu_i = (Z_2(k_i = 0.5))$. Consequently, $MgMn_6Sn_6$ is identified as a topological metal with a bulk Z_2 topological number of (1,011). This leads to the emergence of possible topologically nontrivial surface states. Surface bands can be observed between any pair of diametrically opposing points on the NR, as confirmed by the drumhead-like surface states in surface computations, which generally validate the NR state. The topological charges of the WPs are identified along the Γ-K-M direction. As depicted in Fig.5.9(c), these WPs are further projected onto various surface momentum routes, resulting in surface energy spectra exhibiting Fermi arcs for the top surface.

5.7 Transport Properties

Since the electronic structure of topological materials is intimately linked to their transport properties, in this section, we examine the transport properties of $MgMn_6Sn_6$, specifically exploring phenomena such as the Spin Hall Effect and Anomalous Hall Effect. The immediate detection of the spin-orbit coupling separation amid the Dirac and the flat band emphatically indicates the complex structure of the noted flat band at k_z=0.

To support this, we employ the DFT-based Wannier tight-binding model to examine the parity eigenvalue of the flat bands at the k_z=0 plane using the Fu-Kane formula[305]. This examination results in a topological index Z_2=1 for both flat bands, affirming their topological character. To illustrate how the nontrivial topology of the flat bands influences bulk properties, we additionally computed the band-resolved spin Hall conductivity (SHC) for our compound. The constructed Wannier tight-binding model for $MgMn_6Sn_6$ enables us to conduct ab initio calculations for the SHC and the k-resolved contributions from each band, utilizing the

Kubo formula[306, 307]. The in-plane momentum-resolved SHC primarily concentrates near the point where the degeneracy between the Dirac and flat bands is lifted, a feature connected to its topological nature. This connection is crucial for the formation of quantized SHC within the SOC induced gap, as depicted in Fig.5.8(e).

The Anomalous Hall Conductivity (AHC) is directly linked to the BC, resulting in a transverse anomalous velocity during electronic motion. Evaluating the intrinsic AHC involves applying linear response theory within the Kubo formalism focusing specifically on the AHC in the xy plane by integrating the BC of the bands that are occupied in the whole BZ [Eq.3.1 and Eq.3.2]. A 501 $\times$ 501 $\times$ 501 k grid is used to calculate intrinsic AHC using maximally localised Wannier orbitals. The spin polarised bands of the Mn Kagome lattice, which produce large intrinsic BC, due to the presence of Dirac point, and gapped nodal line close to the E_F. The variation of AHC with Fermi energy is shown in Fig.5.8(f). We found a substantial intrinsic AHC of roughly 500 S/cm at the E_F.

5.8 Summary

In conclusion, we have reported an interesting topological itinerant metal $MgMn_6Sn_6$ which is composed of bilayer Kagome Mn-layer sandwiching the hexagonal Sn layer. We have presented comprehensive electronic properties using ab initio DFT and DMFT calculations. We constructed a two-orbital Hubbard model (see Eq1) and solved it for a unit cell to analyze the many-body configuration of the magnetic ground state. The electrons in the d-orbitals of the Mn atoms do not exhibit full polarization; instead, they form a many-body state characterized by orbital degeneracies. Additionally, competing hopping terms between Mn-Mn and Mn-Sn contribute to frustration within the system. The many-body gs show strong electrons hoping term between Sn and Mn plays an important role in the Ferromagnetic nature of the ground state.

Our ab initio calculations suggest that for $MgMn_6Sn_6$ the nodal line in the K_z=0 plane is protected by mirror symmetry. In the presence of SOC, gaps were found along the nodal line in the presence of magnetic ordering and resulting in a large intrinsic Berry curvature. We have also demonstrated the presence of Dirac fermions at the Brillouin zone corner K, van Hove singularities (VHS) at the zone edge M, and flat bands across the Brillouin zone of $MgMn_6Sn_6$ in the absence of SOC. The Dirac nodes gain a finite mass gap in the presence of SOC and contribute to the BC. Finite SOC breaks the degeneracy at the touching point at the zone centre Γ of the quadratic band and the FB. To the best of our knowledge, the position of the flat band and the gap is the closest to the E_F ever reported in the literature.

there is no reported paper where people showed this gap too near the E_F. The gap induced by SOC strongly suggests that the reported flat band possesses a nontrivial structure, resulting in a nonzero Z2 invariant. Examining how the nontrivial topology of the flat bands influences bulk properties, we additionally computed the band-resolved SHC. The AHC is directly associated with the BC, leading to a transverse anomalous velocity during electronic motion. We discovered a significant intrinsic AHC of approximately 500 S/cm at the E_F. Altogether the electronic properties of $MgMn_6Sn_6$ exhibit many interesting topological properties and interesting frustrated magnetic properties. We hope our study will influence further experimental analysis in this material which may have potential application in future device applications like spintronics(Spin Current Generation, Spin-Orbit Torques, Spin Hall Magnetoresistance) and quantum computing(Spintronic Logic and Memory Devices).

Chapter 6

Topological properties and anomalous transport in van der Waals ferromagnets Fe_nGeTe_2: a comparative study

6.1 INTRODUCTION

Discovery of two and three dimensional non-spatial time reversal symmetry protected topological insulating materials and their prospective applications inspired further prediction of a group of novel states protected by various symmetries such as crystalline symmetry [308–310]. Furthermore, the concept of topological band insulator has been extended to topological semimetals (TSMs)[311–317] which are described by crossing of valence and conduction bands in the Brillouin zone (BZ); for example, the nodes formed by touching the conduction and valence bands at a discrete point are the Weyl/Dirac semimetals since the Weyl/Dirac equations govern their low excitation behavior[316–318]. The recent addition of new type of materials is topological nodal line semimetals (TNLSMs) where bands cross each

other along a line or closed-loop in BZ, and in principle, it can exist in quasi-two-dimensional[245] and three dimensional materials[216, 319].

In TNLSMs, the degenerate crossing point of the conduction and the valence bands near E_F are protected by the spatial symmetry in crystal and time-reversal (TR) symmetries. Any local doping or impurity in the bulk can not lift the degeneracy without breaking protecting symmetries in the system, however, by breaking time-reversal or spin-parity symmetry, the system may have gapped nodal lines or nodal points such as the first principles calculations demonstrate that the electronic band structure of TaAs in the absence of SOC exhibits two nodal lines, which are protected by mirror reflection and spin-rotation symmetries and each nodal line gaps into three pairs of Weyl nodes in the presence of SOC [320, 321]. A double nodal line in $SrIrO_3$ is another example of nodal lines gaping into a pair of Dirac nodes when a mirror reflection symmetry is broken [322, 323]. These nontrivial topological energy bands lead to many exotic phenomena, such as the anamolous Hall conductivity (AHC) and anomalous Nernst conductivity (ANC). The ANC is a thermoelectric counterpart of the AHC, both of which are associated with the Berry curvature (BC) [324, 325]. Moreover, compared to AHC which includes contribution of Berry curvature from all the states below Fermi-level, ANC has the dominant contribution of the BC near E_F [326].

Recently, the van der Waals (vdW) ferromagnet Fe_3GeTe_2 has been demonstrated to be a magnetic variant of TNLSM where in the large BC induced AHC has been attributed to the presence of a gapped nodal line near E_F[327]. Later, related iron-rich compounds in the series Fe_4GeTe_2 and Fe_5GeTe_2 are synthesized and interestingly, both are ferromagnetic vdW compounds [327, 328]. Therefore, topological and magnetic properties of these materials motivated us to investigate the interplay of magnetism and topology in the magnetic vdW materials series, Fe_nGeTe_2 (n = 3, 4, 5)[1] and also to understand their effect on the anomalous transport properties.

[1]"Topological properties and anomalous transport in van der Waals ferromagnets Fe_nGeTe_2: a comparative study" - J. Sau, S. R. Hassan, N. Kumar and M. Kumar, Phys. Scr. 98 125916 (2023)

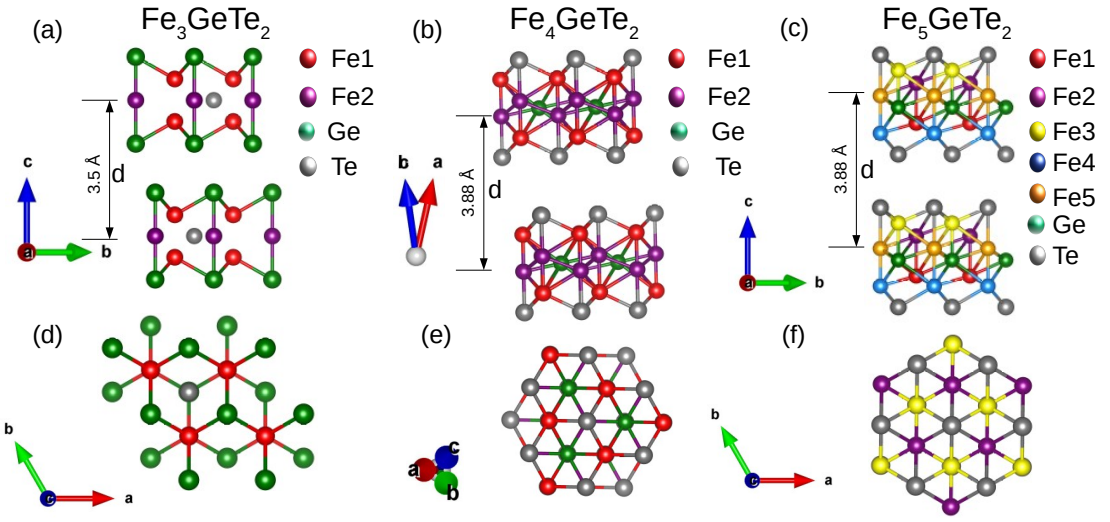

FIGURE 6.1: Three stable vdW structures in the series of Fe_nGeTe_2 for n=3, 4, 5. The upper panels (a), (b), and (c) are side views of the structures Fe_3GeTe_2, Fe_4GeTe_2, and Fe_5GeTe_2, respectively. While the lower panels (d), (e), and (f) are corresponding top views and d represents the inter-layer distance.

In literature the topological vdW ferromagnets are scant, therefore, Fe_nGeTe_2 have recently attracted a lot of attention. This series of compounds are also technologically important due to the large Curie temperature (T_C); T_C = 230 K, 270 K, and 293 K for Fe_3GeTe_2 [327, 329, 329], Fe_4GeTe_2[330] and Fe_5GeTe_2[331], respectively. Chen et al. showed that T_C of Fe_5GeTe_2 could be further enhanced to 478 K upon Ni-doping[326]. The monolayer of these systems shows interesting magnetic behavior and the thin atomic layer can be tuned using the femtosecond laser[332]. Fe_3GeTe_2 also indicated a high electronic correlation in terms of the emergence of Kondo behavior[333]. The density functional theory (DFT) predicts large magnetic anisotropy in Fe_3GeTe_2 and Fe_4GeTe_2 monolayers in the presence of electric field[334, 335]. Fe_5GeTe_2 shows butterfly type of magneto-resistance[336]. These materials have a potential application in the electrical control of magnetism and spintronic devices[186, 337–339].

The structural characteristics of Fe_nGeTe_2 could be understood in terms of the triangular Fe-layers and Fe-Fe dumbbells. In Fe_3GeTe_2, Fe1 makes a triangular lattice when considered together with Ge which can be viewed as a honeycomb lattice. Fe2-Fe2 dumbbells align perpendicular to the layer, in the center of each hexagon of the honeycomb lattice, with one Fe2 above the hexagon and another

Fe2 below the hexagon. Fe_3GeTe_2 belongs to the space group $P6_3/mmc$ (No.194). Fe_4GeTe_2 consists of two types of dumbbells each displaced with respect to the other along the direction perpendicular to the vdW layer. Fe_4GeTe_2 has a rhombohedral structure with space group $R\bar{3}m$ (No.166). The structure of Fe_5GeTe_2 also consists of two types of dumbbells as in the case of Fe_4GeTe_2, in addition to a triangular layer of Fe. The space group of Fe_5GeTe_2 is $P3m1$ (No.156)[327]. These materials also have C_{3y} symmetry in addition to a mirror or C_2 symmetry. The top and side views of Fe_nGeTe_2 structures have been depicted in Fig.7.1, where different Fe atoms are distinguished with separate colors. Crystal symmetry plays an important role to host symmetry protected states in these systems.

In this chapter, we perform a comparative study of the electronic properties of Fe_nGeTe_2 (n = 3, 4, 5) and explore the origin of the topological states. These materials have large anomalous transport properties, therefore, a comparative study of transport properties has been carried out. The magnetic space group and their associated symmetry are also studied to show the effect on the degeneracy of energy dispersion. A tight-binding model Hamiltonian is extracted by fitting bands obtained from the DFT calculations, and the model is used to explore AHC and ANC using the Wannier90. The main goal of this manuscript is to do a comparative study of anomalous transport in this series of materials and the effect of crystal symmetry on topological states.

The remainder of this chapter is organized as follows. In Sec.6.2, we briefly discuss the computational details followed by a discussion on the magnetism of these three materials in Sec.6.3. Magnetic space group detail analysis and associated electronic band topology are covered in Sec.6.5 and Sec.6.4. Sec.6.6 summarises our results on the nontrivial band topology, nodal lines, and corresponding BC distribution. We present our paper's primary focus, anomalous transport, in Sec.6.7 and conclude with a summary and conclusion in Sec.6.8

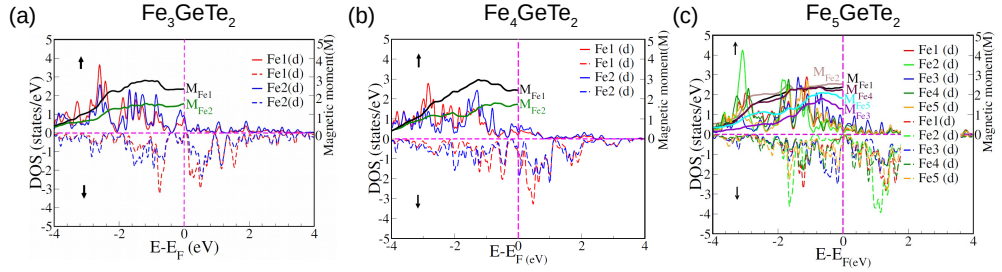

FIGURE 6.2: (a) The total DOS for Fe_3GeTe_2 as a function of (E-E_F) is plotted where the blue and red curves represent the total DOS for the majority spin carrier (solid) and minority spin carrier (dotted) of Fe1 and Fe2, respectively. The magnetic moments, M_{Fe1} (M_{Fe2}) is shown with the black (green) curve, the main contribution from the majority spins. (b) Similarly, the total DOS for Fe_4GeTe_2 as a function of (E-E_F) is plotted where the blue and red curves represent the total DOS for the majority spin carrier (solid) and minority spin carrier(dotted)of Fe1 and Fe2, respectively. The magnetic moments, M_{Fe1} (M_{Fe2}) is shown with the black (green) curve. (c)the total DOS for Fe_5GeTe_2 as a function of (E-E_F) is plotted where the red, green, blue, deep green and orange curves represent the total DOS for the majority spin carrier (solid) and minority spin carrier (dotted) of Fe1 and Fe2, Fe3, Fe4 and Fe5, respectively. The magnetic moments, M_{Fe1}, M_{Fe2}, M_{Fe3}, M_{Fe4} and M_{Fe5} are shown by black, brown, violet, maroon and cyan, respectively.

6.2 Theory and Computational Details

We examine the electronic structures and transport properties of Fe_nGeTe_2 in the scheme of DFT. First principles calculations are performed using the VASP package [340] based on the generalized gradient approximation (GGA)[219] of the Perdew-Burke-Ernzerhof (PBE)[341] for the exchange-correlation functional. A plane-wave basis set with a kinetic energy cutoff of 600 eV is considered while performing first principles calculations. Furthermore, we have used 6×6×6 k-point mesh for Fe_nGeTe_2. The Gaussian smearing method is employed for broadening the Fermi surface with a width of 0.05 eV. Both cell parameters and internal atomic positions were fully relaxed until the forces on all atoms were smaller than 0.01 eV/A. To explore the nontrivial band topology and the intrinsic AHE, the tight-binding Hamiltonian was constructed with the maximally localized Wannier functions [168, 169]. The intrinsic AHC is computed using the linear-response Kubo formula approach in the clean limit, and a 500×500×500 k-grid in the BZ was used for the integral of the AHC.

6.3 Magnetic Properties

In this section, the magnetic properties of all three vdW compounds Fe_3GeTe_2, Fe_4GeTe_2 and Fe_5GeTe_2 are studied. We calculate spin resolved total density of states (DOS) to understand the magnetic moments. We notice that the d-orbitals of Fe atoms dictate the magnetism, therefore, we show only the DOS of the d-orbitals where down spin DOS is shown as negative of its value. We calculate the total magnetic moment of Fe atoms as a difference of total up and down spin electrons filled up to E_F where the density of up or down electron at any energy is proportional to the DOS of up and down spins at that energy.

Fe_3GeTe_2: In this compound, there are two in-equivalent Fe atomic sites denoted as Fe1 and Fe2 as shown in Fig.6.1(a), Fe1 lies in the a-b plane and arranged on hexagonal structure whereas Fe2 lies perpendicular to this plane. Energy dependence of spin up (solid line) and down (dashed line) DOS are shown in Fig.6.2(a): red lines represent the DOS of Fe1 atoms, whereas the blue line represents the DOS of Fe2 atoms. The partial DOS calculations suggest that the DOS of all d-sub-orbitals are spread near the E_F therefore, electrons of all the sub-orbitals are delocalised. The DOS of Fe1 compared to Fe2 has a higher magnitude at -2.5 eV, whereas, the DOS of Fe2 has a marginally larger value compared to Fe1 between the energy range -2 eV to 0 eV. We note that the difference between up and down DOS of Fe2 atoms has a higher spread than that of Fe1 atoms; therefore, we expect a higher magnetic moment for Fe1 than Fe2. The magnetic moments M_{Fe1} and M_{Fe2} for Fe1 and Fe2 atoms are shown as solid black and green lines in Fig.6.2(a). M_{Fe1}(2.5 μ_B/atom) is higher than that of M_{Fe2}(1.6 μ_B/atom) at 0K.The magnetic moment is substantial along the c-axis due to uniaxial magnetocrystalline anisotropy along this direction[195]. In our calculations, magnetic polarisation is considered along the [001] direction. As a result, for Fe_3GeTe_2, $M_{Fe}(2.2\mu_B/\text{atom})$ represents the average contribution of the magnetic moment in Fe along the c-axis, and it closely matches the experimentally observed value (2.4 μ_B/atom)[195].

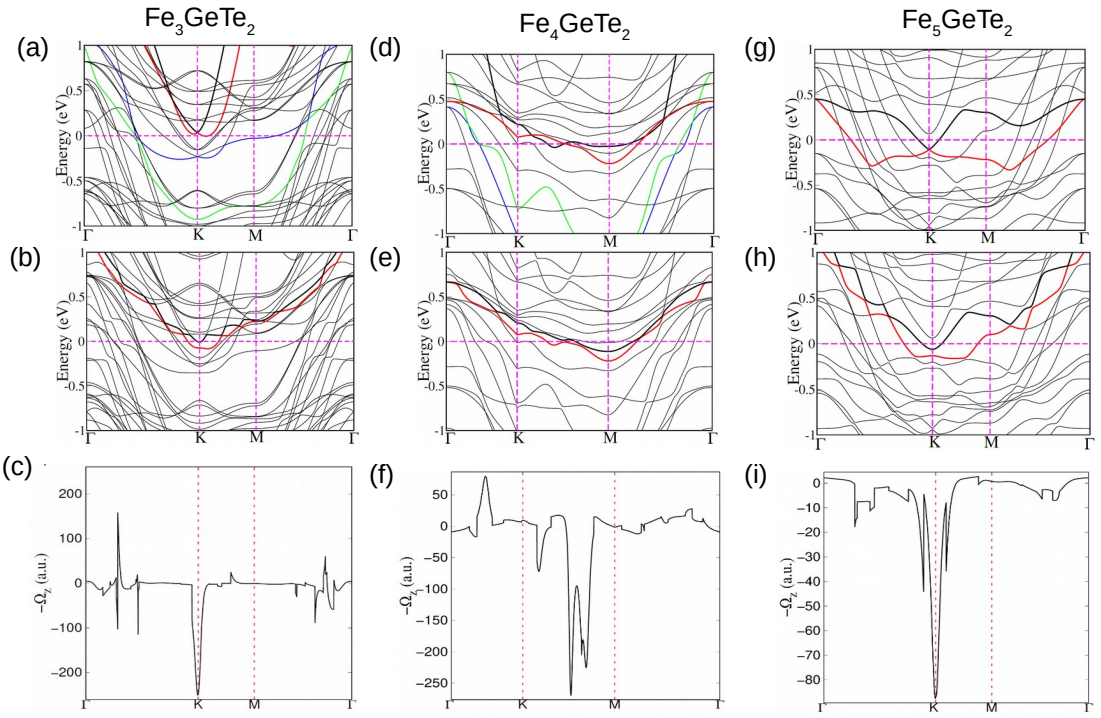

FIGURE 6.3: The band structure of Fe_nGeTe_2 without and with SOC. After opening a gap, there is a Berry curvature along high symmetry lines. (a) For Fe_3GeTe_2, the crossing point at K, 0.03 eV above the E_F without SOC. At K point the crossing point is formed by thick red and black colour bands. Green and blue bands also form nontrivial crossing near E_F along K-Γ (b) The gap opens just below the E_F due to SOC. (c) Corresponding to nontrivial crossings there are finite Berry curvature (d) The crossing point is between K and M points at the E_F for Fe_4GeTe_2 without SOC. The crossing point is formed by thick red and black colour bands. Green and blue bands also form nontrivial crossing near E_F along K-Γ (e) Lifting the degeneracy in the direction of K-M and K-Γ due to SOC. (f) Finite Berry curvature corresponds to this degeneracy. (g) The crossing point formed by thick red and black colour bands)K point below the E_F in Fe_5GeTe_2 without SOC. (h) With SOC, the gap opens (i) Negative Berry curvature is shown due to TR (inclusion of SOC) symmetry breaking.

Fe_4GeTe_2: This system has also two in-equivalent Fe sites labeled as Fe1 and Fe2 in Fig.6.1(b). Fe2 atoms lie below the Te atom of hexagonal plaquettes and Fe1 atoms are present in hexagonal plaquettes. The up and down spin DOS are plotted as a function of energy with solid and dotted lines. Red and blue colour represents the DOS of Fe1 and Fe2 d-orbitals. The Fe2 d-bands are more dispersed compared to Fe1. The DOS of Fe1 has a larger amplitude at -2.8 eV for spin up electron than in Fe2 DOS, as shown in Fig.6.2(b). The magnetic moments M_{Fe1} and M_{Fe2} for atoms Fe1 and atoms Fe2 are shown as solid black and green

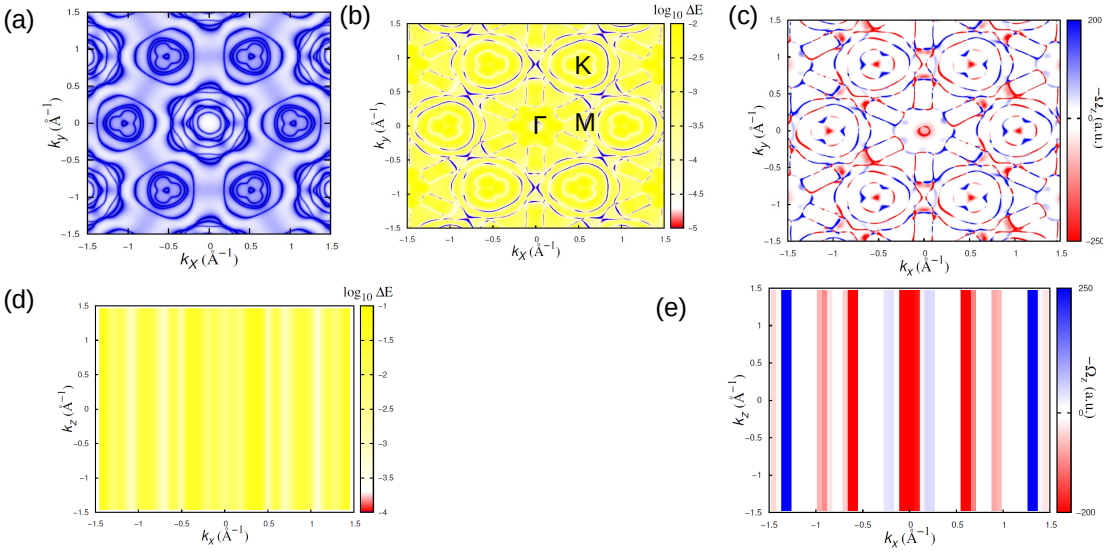

FIGURE 6.4: For Fe_3GeTe_2 with SOC: (a) 2D Fermi surface using spectral function A(K_x, K_y, $K_z = 0$, E_F). (b) Energy gap, ΔE(K_x, K_y, K_z) = (E$_a$ (K_x, K_y, K_z)-E$_b$ (K_x, K_y, K_z)), between two crossing bands (a(red) and b(blue)) and the high symmetry points are also shown. (c) The Berry curvature distribution, Ω_z (K_x, K_y, $K_z = 0$) has a large negative value at the K point (red spot). (d) Energy gap, ΔE (K_x, K_z, $K_y = 1$ Å^{-1}) and gapped nodal line at $K_x = 0.5$ Å^{-1} and $K_x = -0.5$ Å^{-1}. (e) The Berry curvature distribution along gapped Nodal line, Ω_z (K_x, K_z, $K_y = 1$ Å^{-1}).

lines in Fig.6.2(b). M_{Fe1} and M_{Fe2} are 2.47 and 1.7μ_B/atom, respectively.The easy magnetic axis is observed experimentally along the c-axis[330]. Our analysis takes the magnetic polarisation direction along the [001] direction. The predicted value of M_{Fe}=2.084 μ_B/atom for Fe's average magnetic moment in the c direction coincides nicely with the experimental measurement (1.8 μ_B/atom)[327]

Fe_5GeTe_2: It contains five in-equivalent Fe sites which are shown in Fig.6.1(c) and two atoms Fe1, Fe4, and Fe5 are in the same a-b plane in negative c direction. Fe1 and Fe4 have similar chemical environments but Fe5 has different chemical environments. Fe2 and Fe3 are also the same a-b plane in positive c direction and have different chemical environments. d-orbitals of these atoms are also highly hybridized. DOS of all five Fe d-orbitals are shown in Fig.6.2(c). DOS of Fe1 and Fe4 looks similar, whereas it is distinct from the other three Fe atoms. The green curve exhibits a large peak in up DOS of Fe2 at -3.0 eV signifying localization of magnetic moment. Fe2 atoms have the highest magnetic moments and Fe5 and Fe3 have the lowest contribution. Fe5 and Fe3 d-orbitals have higher DOS

for both up and down spins near the E_F but they are dispersed over energy. The colored thick lines represent the magnetic moments for all five Fe atoms and the largest magnetic moment is M_{Fe2}=2.55 μ_B/atom for Fe2, as expected. The magnetic moment of Fe1 and Fe4 are nearly the same M_{Fe1}=2.4 μ_B/atom and M_{Fe4}=2.3 μ_B/atom respectively, whereas the magnetic moment of Fe_3 and Fe5 are M_{Fe3}=1.29 μ_B/atom and M_{Fe5}=1.84 μ_B/atom. Experimental research has also revealed that the magnetic easy axis in this material is along the c axis[342]. The average magnetic moment per Fe atom along the c direction is M_{Fe}=2.064 μ_B/atom, which agrees with the experimental reported value (2.4 μ_B/atom).[342]

6.4 Nontrivial band topology

The electronic band structure of the Fe_nGeTe_2 system is studied and the topological aspect of energy bands is explored at energy band crossover points. We notice that the majority of the contributions energy bands are from the d-orbitals of the magnetic atom Fe near the E_F, therefore, the main focus of our study of energy bands will be close to the E_F. Using the wannier90 we compute a multiorbital tight-binding model

$$H_{tb} = \sum_{<ij>,\sigma,\alpha,\alpha'} t_{ij}(c_{i\sigma}^{\dagger\ \alpha} c_{j\sigma}^{\alpha'} + H.c.) + \sum_{i,\sigma,\alpha} \epsilon_i^{\alpha} n_{i\sigma}^{\alpha} + \sum_{i\alpha} \lambda_i \vec{L}_i^{\ \alpha} \cdot \vec{S}_i^{\ \alpha}$$

where i and j are the atomic index and α is the index for various orbitals of the atoms. σ is the spin index. The tight-binding hopping parameters are represented by t_{ij}. The tight-binding Hamiltonian is constructed using the s and d orbitals of Fe atoms, the s and p orbitals of Ge and Te atoms. The spin-orbit coupling constant is represented by λ_i.

Fe_3GeTe_2: The energy dispersion near E_F is shown in Fig.6.3(a) without SOC and in Fig.6.3(b) with SOC and in the absence of SOC two bands represented by 'a' (thick red line) and 'b' (thick black line) cross at point K above 0.03 eV E_F as shown in Fig.6.3(b). These two bands are solely contributed by the d orbitals

of Fe1 and Fe2 atoms. We observe that the band crossing resembles Mexican-hat shapes induced by the Rashba effect with quenched spins, as reported in the literature[195], and degeneracy at the K point arises due to crystal symmetries of Fe1 and Fe2 atoms. However, the application of SOC and the magnetic moment along [001] direction lifts this degeneracy. In the neighborhood of E_F, there are some other band crossings that contribute to large BC which lie along the high symmetry direction M-Γ and K-Γ as shown in Fig.6.3(a). These bands are shown in blue and green color; blue color bands are composed of d-orbitals of Fe1 and Fe2, whereas the green color band has a majority contribution from the p-orbital of Ge. The non-trivial crossing points open a gap in the presence of the SOC.

Fe_4GeTe_2: All the energy bands close to the E_F are contributed by Fe atoms, Many energy bands cross, close to E_F, as shown in Fig.6.3(d), and these bands are formed from the d_{xy}, d_{xz}, d_{yz}, and $d_{x^2-y^2}$ sub-orbitals of Fe atoms. The nontrivial degeneracies near the E_F are along the K-M and the other band crossings are located along the high symmetry direction K-Γ in the vicinity of E_F, contribute to significant BC. These bands are depicted in blue and green; the blue bands include d-orbitals of Fe1 and the green band is due to d-orbitals of Fe2. We have shown one nontrivial crossing point which is originated by two bands represented by 'a' (thick red line) and 'b' (thick black line) at E_F. However, the magnetic moment is along [001] direction and degeneracy is lifted in the presence of SOC as shown in Fig.6.3(e). The BC in this system shows a large negative value along the K-Γ symmetry direction as shown in Fig.6.3(f).

Fe_5GeTe_2: Most energy bands near the E_F are contributed from the d_{xz},d_{yz} and $d_{x_2-y_2}$ sub-orbitals of Fe atoms. The nontrivial band crossing is -0.11 eV below the E_F at the K point as shown in Fig.6.3(g). There are two other crossings close to K point along K-M and K-Γ directions -0.1 eV below E_F. However, in the presence of SOC, the gap opens at these points as shown in Fig.6.3(h). The BC along the K-M and K-Γ symmetry directions are shown in Fig.6.3(i). We notice a large negative BC at the K point and two other crossings around the K point as mentioned earlier and this crossing point has a similar origin to that of bands close to the E_F in Fe_3GeTe_2.

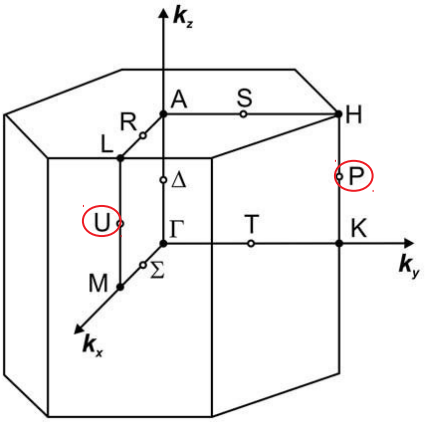

FIGURE 6.5: First Brillouin zone of a hexagonal lattice where P and U are high symmetry lines along K-H and M-L

6.5 Magnetic Space group symmetry

To comprehend the degeneracies of energy bands in BZ, we analyze the magnetic space group (MSG) symmetry, which relies on the crystal's magnetization and points group symmetry. There are 1651 MSG in total, but only 528 of them are pertinent to two-dimensional magnetic materials[343]. Using the Bilbao crystallographic server, the MSG for Fe_nGeTe_2 materials is calculated. We calculate a fat band to analyze the d-orbital contribution to the energy dispersion.

Fe_3GeTe_2 belongs to the 194-space group symmetry, and the MSG number is 194.26, which is confirmed by using the three-dimension structure of the system and considering the magnetic moment along the easy axis. There are two types of Fe in this system: Fe1 and Fe2. Fe1 is in the Wyckoff position of 4e and has a 3m site symmetry with a high symmetry line along P (K-H) shown in Fig.6.5. The Wyckoff position of Fe2 is 6h which has mm2 site symmetry. This symmetry results in high symmetry points along U(M-L), and these high symmetry lines are related by rotational and translational symmetry. The Fe1 and Fe2 orbitals are orthogonal to each other; therefore, crossing points of these bands along a high symmetry line may give the degenerate line. To show the orthogonality of these bands, we examine the orbital contributions at K points and detect that there are two orbitals:d_{xz} and d_{yz} of each Fe1 and two orbitals: $d_{x^2-y^2}$ and d_{xy} of each Fe2 contribute.In total, there are 12 orbitals per unit cell. The molecular orbital

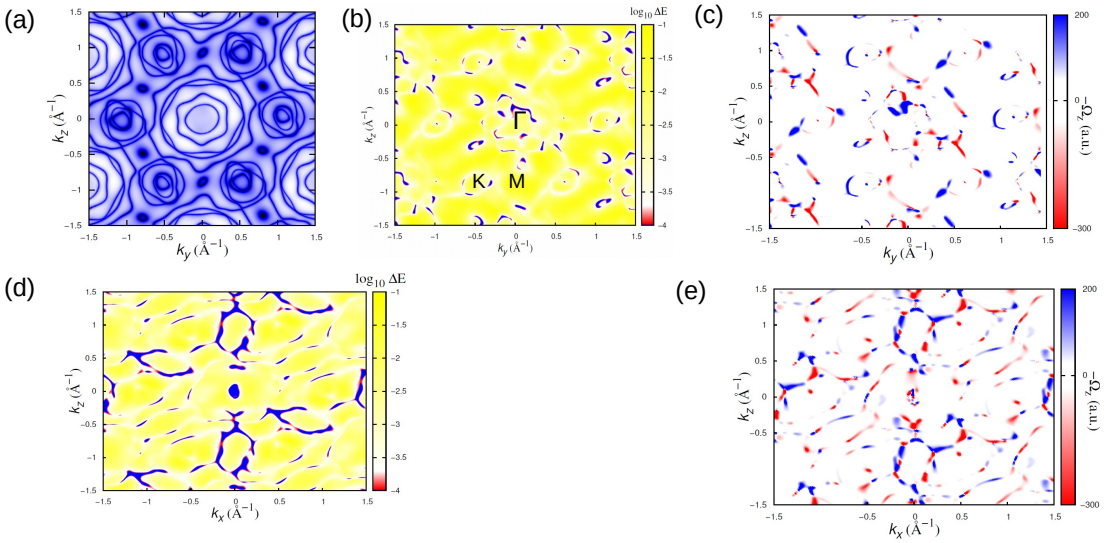

FIGURE 6.6: For Fe_4GeTe_2 with SOC: 2D Fermi surface, the energy gap, $\Delta E(K_y, K_z, K_x = 0)$ and the Berry curvature distribution are plotted in (a),(b) and (c), respectively. We also calculate the energy gap, $\Delta E(K_x, K_z, K_y = 0)$ and the Berry curvature distribution in K_y=0 in (d) and (e), respectively

of linear combination of Fe1 orbitals has angular momentum $L^Z_{Fe1} = \pm 1$ whereas Fe2 molecular orbitals has $L^Z_{Fe2} = \pm 2$. Therefore, the bands of Fe1 and Fe2 are orthogonal to each other as L^Z_{Fe2} of these two atoms are different. These results are similar to that in ref [195]. The SOC acts at the atomic site and is defined as H_{so} = A $\mathbf{L}\cdot < \mathbf{S} >$ for all atoms, and can be treated as the perturbation in the Hamiltonian.The doubly degenerate bands along the K-H line opens a gap in the presence of SOC, and the perturbation term in Hamiltonian H_{so} can be treated by degenerate perturbation theory in the doubly degenerate bases. The first-order energy correction is obtained by diagonalizing the 2×2 matrix in these bases. The energy gap has a dominant contribution from the first-order perturbation component, therefore, if magnetization has a finite z-component, the degeneracy at the symmetry points can be lifted, and the gap is proportional to the average magnetization $< L^z S^z >$.

Fe_4GeTe_2 is a member of the 166-point group symmetry, also known as the $R\ \bar{3}\ m$ symmetry group. In this material, Fe1 and Fe2 atoms make two hexagonal layers as shown in Fig.7.1(b) and have C_3 symmetry about the axis perpendicular to layers. Compared to Fe_3GeTe_2, which only has 24 symmetry operations, this

three-dimensional structure has 36 symmetry operations and has an MSG number 166.67, where both Fe1 and Fe2 atoms are at the 36i Wyckoff position. The degenerate point is along the K-M, resulting from Fe1 and Fe2 bands composed of orthogonal orbitals that give rise to degenerate points. The d_{xy} and d_{yz} orbitals of each Fe1 are composed of a crossing band, whereas the other crossing band is formed of $d_{x^2-y^2}$ and d_{xz}. We examine the contribution of orbitals at the crossing points shown in Fig.6.3(e) to understand the bands' orthogonality. Linear combination of d_{xy} and d_{yz} orbitals can have angular momentum $L^z = \pm 1$, whereas, for Fe2 band the $L^z = \pm 3$. In the presence of finite magnetic moment along the z-direction similar to that in Fe_3GeTe_2, SOC lifts the degeneracies and can be explained by degenerate perturbation theory.

Fe_5GeTe_2 is a member of the $P3m1$ symmetry group, also known as space group symmetry No.156 [327]. In addition to a mirror or C_3 symmetry similar to Fe_3GeTe2, it also has C_{2y} symmetry and corresponds to MSG number 156.49. The band degeneracies and bands near E_F are composed of Fe2 and Fe3 orbitals, and the site symmetry groups for Fe3 (Wyckoff position 1a) and Fe2 (Wyckoff position 3d) have site symmetry 3m and m, respectively. The two-fold degeneracy is caused by the Fe2 and Fe3 bands having an orthogonal orbital contribution at the K point. At this point, Fe2 band is composed of d_{xz} and d_{yz}, whereas the Fe3 band is composed of d_{xy} and $d_{x^2-y^2}$. The molecular orbital of Fe2 has $L^z = \pm 1$; on the other hand, the molecular orbital of Fe3 has $L^z = \pm 2$, similar to Fe_3GeTe_2 material. The lifting of degeneracy due to SOC along the K-H line is very similar to that of the Fe_3GeTe_2 system.

6.6 Nodal line and Berry curvature distribution

This section highlights the band crossing features by the 2D Fermi surface using the spectral function $A(\mathbf{k}, E_F)$ computed using the wanniertools[**?**], the energy gap, $\Delta E(\mathbf{k})$ between the band crossing and the z component of the BC, $\Omega_z(\mathbf{k})$ at each point of the BZ. We usually observe large BC at the crossing points or the

nodal lines. We show our results in various two dimensional planes like the $K_z = 0$ plane, $K_x = 0$ plane, and $K_y = 0$ plane separately.

Fe_3GeTe_2: Fig.6.4(a) shows the FS plot in $K_z = 0$ plane. The calculated FS consists of a circular-shaped pocket centered at the six K-point and a hexagonal-shaped pocket centered at Γ. The blue region shows a high spectral function value and the white region represents a small spectral function value. The spectral function's intense value reveals the band's degeneracy and crossing between different bands. Most of the region is blue i.e., high spectral function regime which is present around Γ point and six K points which exhibit high spectral function. In Fig.6.4(b) gap distribution $\Delta E(K_x, K_y, K_z = 0)$, is shown in the presence of SOC, and a gap smaller than 10^{-5} eV is considered to be zero. The white region is around K points and corresponding to this gap there is a finite BC as shown in Fig.6.4(c) with the red spot. We also studied the energy gap in $K_y = 0$ plane and observed a gapped line, as shown in Fig.6.4(d) by a white line (at near $K_x = 0.5$ Å^{-1} and $K_x = -0.5$ Å^{-1}) called a gapped nodal line. The BC is large at this nodal line, and we show it in Fig.6.4(e) by a red line(at near $K_x = 0.5$ Å^{-1} and $K_x = -0.5$ Å^{-1}).

Fe_4GeTe_2: In Fig.6.6(a), 2D FS using the spectral function is plotted in the $K_y = 0$ plane, and there is a Γ-centered hexagonal-shaped and six K and M point-centred circular-shaped FS. Like the previous system, the blue region shows a high spectral function value indicating band degeneracy and the crossing point. The white region represents a value close to zero i.e., a small spectral function. The intense value of the spectral function at the black dots around the Γ points and blue lines around K and M points indicate band crossing and band degeneracy. SOC opens tiny gaps along the K-M direction, as shown in Fig.6.6(b). White spots between the K-M line and Γ points correspond to gapped regions and BC at these points are high, as shown in Fig.6.6(c) by red spots. The gaps and BC are also calculated in the $K_x = 0$ plane, but there is not much feature associated with it. Gaps and finite BC are scattered in the first BZ; therefore, we safely conclude the absence of a nodal line.

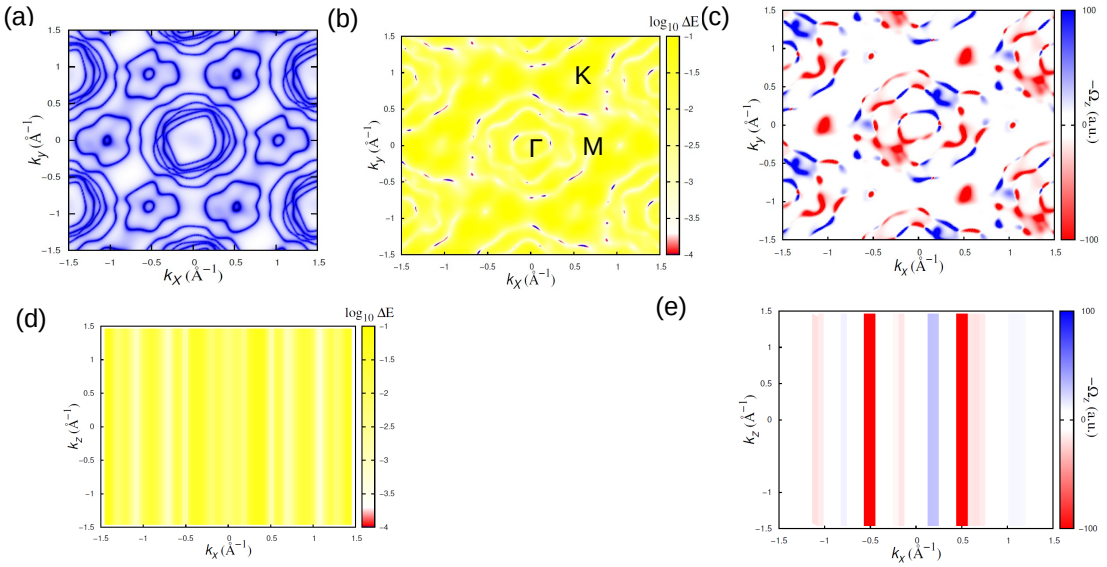

FIGURE 6.7: For Fe_5GeTe_2 with SOC: (a) 2D Fermi surface using spectral function A(K_x, K_y, $K_z = 0$, E_F). (b) Energy gap, ΔE(K_x, K_y, K_z) = (E$_a$ (K_x, K_y, K_z)-E$_b$ (K_x, K_y, K_z)), between two crossing bands (a(red) and b(blue)) and the high symmetry points are also shown. (c) The Berry curvature distribution, Ω_z (K_x, K_y, $K_z = 0$) has a large negative value at the K point (red spot). (d) Energy gap, ΔE (K_x, K_z, $K_y = 1$ Å^{-1}) and gapped nodal line at $K_x = 0.5$ Å^{-1} and $K_x = -0.5$ Å^{-1}. (e) The Berry curvature distribution along gapped Nodal line, Ω_z (K_x, K_z, $K_y = 1$ Å^{-1}).

Fe_5GeTe_2: Fe_3GeTe_2 and Fe_5GeTe_2 have similar symmetries; therefore, the spectral function behavior and its symmetry are expected to be similar, as can be seen in Fig.6.7(a) of the contour plot of FS. The blue line with a high spectral function value in the neighborhood of Γ points and six K points, reflects the band degeneracy and the band crossing. In Fig.6.7(b), gap distribution, $\Delta E(K_x, K_y)$, is shown in the first BZ, and blue and white regions show tiny gaps opened at the high symmetry points due to the SOC. Mainly the white region is around the K points, and corresponding to this gap, there is a finite BC, as shown in Fig.6.7(c) with the red spot. In $K_y = 0$ plane, white stripes represent the gaped nodal line as shown in Fig.6.7(d), and there is a large BC associated with it as shown in Fig.6.7(e) by a red and blue line(near $K_x = 0.5$ Å^{-1} and $K_x = -0.5$ Å^{-1}).

6.7 Anomalous transport properties

We also study anomalous transport properties described by a tight-binding Hamiltonian, H constructed by fitting its parameters with DFT results. As discussed in the previous section, these materials exhibit a large BC on the nodal lines in the presence of SOC. The BC ($\mathbf{\Omega}$) acts as a magnetic monopole in the momentum space giving rise to anomalous Hall and heat conductivity.

The computation of the BC requires the energy eigenvalues $E_n(k)$ is the eigenvalue of the nth eigenstate $\psi_n(k)$. The BC $\mathbf{\Omega}^n(\mathbf{k})$ is written[335] using Eq.3.1 and Eq.3.2.

The BC-effect also manifests in thermoelectric transport is driven by a statistical force, for example, temperature gradient. In the presence of a temperature gradient, the local current of carriers acquires an additional term from the carrier's magnetic moment in the presence of a non-uniform distribution. The extra term, an extrinsic Hall current $\mathbf{j}_{in}$, can be written in terms of the BC as,

$$\mathbf{j}_{in} = -\frac{\nabla T}{T} \times \frac{e}{h} \sum_n \int d\mathbf{k} \Omega^n(\mathbf{k}) [(\epsilon_{n\mathbf{k}} - \mu) f_n(\mathbf{k}) + k_B T log(1 + e^{\beta(\epsilon_{n\mathbf{k}} - \mu)}] \tag{6.1}$$

the Nernst conductivity α_{xy} can be extracted using $j_x = \alpha_{xy}(-\Delta T_y)$ and the α_{xy} can be written as[335]

$$\alpha_{xy} = -\frac{1}{e} \int d\epsilon \frac{-df(\epsilon)}{d\mu} \sigma_{xy}(\epsilon) \frac{(\epsilon - \mu)}{T}, \tag{6.2}$$

where intrinsic AHC $\sigma_{xy}(E_F)$ at zero temperature with Fermi-energy E_F.

All three materials show the variation in AHC as (E-E_F) varies, which is prominent in n = 3, 5 compared to n = 4. For Fe_3GeTe_2 as the energy (E-E_F) varies, AHC first decreases from 300 S/cm to −400 S/cm at (E-E_F) = −0.1 eV and then increases as (E-E_F) approaches zero and acquires a value of 150 S/cm. This material reveals the large BC at the nodal line, as seen in Fig.6.3(c), which causes a

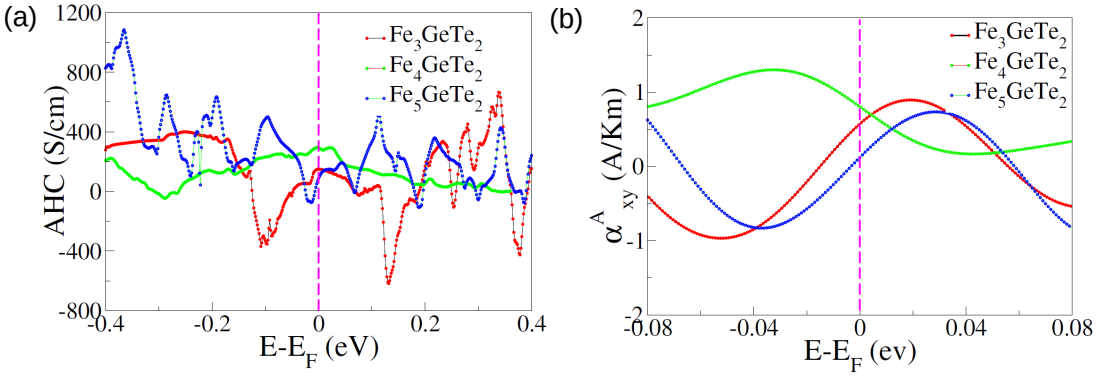

FIGURE 6.8: (a) Red, green and blue curves represent Energy (E-E_F) dependence of the AHC For Fe_3GeTe_2, Fe_4GeTe_2 and Fe_5GeTe_2 respectively. (b) Red, green, blue curve represent Energy (E-E_F) dependence of the ANC for Fe_3GeTe_2, Fe_4GeTe_2 and Fe_5GeTe_2, respectively.

high value of AHC. The SOC opens the gap in the energy bands below the Fermi energy, E_F, which contributes to a large variation in BC. Further, we can tune its values by doping, for example, up to 600 S/cm by electron doping and 450 S/cm by hole doping. Our result is consistent with the experimental value of AHC[195] 150 S/cm, at a low temperature. In Fe_4GeTe_2 the six-fold degeneracy around K and M points lying close to E_F contributes to the large value of AHC, 295 S/cm at (E-E_F) $= -0.4$ eV decrease to -100 S/cm at (E-E_F) $= -0.3$ eV and at E_F its value reaches to 300 S/cm. In the case of Fe_5GeTe_2, various bands contribute to BC, which is responsible for fluctuating AHC with (E-E_F). The calculated AHC is 90 S/cm and most of the contribution comes from the nodal line below the E_F.

Compound	Magnetic moment		AHC		ANC	
	Theory	Experiment	Theory	Experiment	Theory	Experiment
Fe_3GeTe_2	$2.2\mu_B$/atom	$2.4\mu_B$/atom	150S/cm	150S/cm	0.55A/Km	0.50A/Km
Fe_4GeTe_2	$2.0\mu_B$/atom	$1.8\mu_B$/atom	295S/cm	366S/cm	0.8A/Km	no experiment
Fe_5GeTe_2	$2.1\mu_B$/atom	$2.4\mu_B$/atom	90 S/cm	147 S/cm	0.10A/Km	no experiment

We now discuss ANC which is intimately related to anomalous Nernst effect (AHE) via anomalous thermoelectric response tensor and emerges when charge carriers acquire an anomalous transverse velocity in a longitudinal temperature gradient and a finite BC. In contrast to ANC which probes BC of the whole Fermi sea, ANC is sensitive to the BC near E_F. As a result, ANC may become the dominant

term of the total Nernst signal in this series of materials with an enhanced BC near the Fermi energy. Fig.6.8(b) shows ANC at room temperature and as a function of (E-E_F) for all three materials. The behavior of Fe_3GeTe_2 and Fe_5GeTe_2 are similar but opposite to Fe_4GeTe_2. Near Fermi energy E-E_F = 0, Fe_4GeTe_2 has a large value while Fe_3GeTe_2 and Fe_5GeTe_2 have a small value. This suggests that band crossing near the Fermi energy in all these materials is different, as evident in the band structure calculation discussed in the previous section. The calculated value of ANC for Fe_4GeTe_2 (0.8 A/Km), followed by Fe_3GeTe_2 (0.55 A/Km) and Fe_5GeTe_2 (0.10 A/Km) at room temperature. The experimentally observed value of ANC [344] for Fe_3GeTe_2, 0.55 A/Km, is close to our calculated value. It is confirmed from magnetic space group symmetry how the small gap at the degenerate point is caused in the presence of SOC. Eq.3.2 allows us to determine the z component of BC corresponding to this tiny gap. The xy component of AHC and ANC can be calculated using the BC. Other components of AHC and ANC are almost zero because of the magnetic moment along [001] direction.

6.8 Summary

In this work, we perform a comparative study of the electronic properties, the topological aspect of their energy bands, and the accompanying anomalous transport characteristics of Fe_nGeTe_2 (n=3,4,5), itinerant van der Waals ferromagnetic semimetals. Fe_3GeTe_2 and Fe_5GeTe_2 contain nodal lines in the electronic band. In contrast, in Fe_4GeTe_2, non-trivial energy band crossings occur between the high symmetry points K and M. All three systems contain either two-fold mirror symmetry or rotational symmetry perpendicular to the c-axis, as well as three-fold rotational symmetry about this axis. In Fig.6.4(a), Fig.6.6(a), and Fig.6.7(a) the influence of symmetry is mirrored in the spectral densities at the Fermi surface. We also show that Fe_3GeTe_2 exhibits additional non-trivial degenerate points along the high symmetry lines of K-Γ near E_F and M-Γ near E_F, in addition to the bands crossing at the K point discovered in ref.[195]. These crossing bands are composed of Fe d-orbitals and Ge p-orbitals but have finite BC at these crossing

points. The electrons in the d-orbitals of the Fe atoms contribute all the magnetic moments (M) in this system, and the computed values of M are compatible with the experimental values ([195, 342**?**]). We also show that the emergence of symmetry-protected energy degeneracy is strongly influenced by magnetic space group symmetry. The mechanism of lifting the degeneracy of crossing points is also discussed in the presence of SOC with a finite magnetic moment which leads to non-zero BC. The finite value of BC contributes to intrinsic anomalous Hall and Nernst conductivity. The calculated value of AHC at low temperatures agrees with the experimentally reported value [195] for Fe_3GeTe_2. In the case of Fe_4GeTe_2, we notice that a large contribution of BC comes from the vicinity of band crossing points along K-M, which are close to E_F. Therefore, this material has the largest AHC (295 S/cm) out of all three materials. We find that the ANC for Fe_3GeTe_2, Fe_4GeTe_2, and Fe_5GeTe_2 are 0.55 A/Km, 0.80 A/Km, and 0.10 A/Km, respectively. The experimentally reported value of ANC in Fe_3GeTe_2 in Ref [344] is fairly close to our calculated value. Comparing magnetic and transport measurements' theoretical and experimental data of Fe_nGeTe_2 are listed in Table **??**. It has also been explored how the AHC and ANC correlate with the change in E_F, and how this shift might be brought on by the system being doped with electrons or holes. The enormous ANC in these materials offers intriguing potential for the subsequent evolution of thermoelectric energy conversion devices.

In conclusion, we have carried out a comparative study of magnetism, electronic band structure, topological band crossing, and their effect on the anomalous transport properties in Fe_nGeTe_2 (n=3,4,5) materials. We now present a table in the Supplemental section for comparing theoretical and experimental magnetic and transport measurement results. We investigated how different Fe d-orbitals contributed to the ferromagnetism in Fe_nGeTe_2. Symmetry analysis includes magnetic space group symmetry-related topological features in the band structure, which give rise to the Berry curvature effect in the presence of spin-orbit coupling, responsible for large anomalous Hall conductivity and anomalous Nernst conductivity. This study will help us comprehend these materials better.

Chapter 7

Emergence of anomalous transverse conductivity in ferromagnetic topological double perovskite Ba_2CoWO_6 due to intrinsic spin-orbit coupling within the multi- orbital Hubbard model and ab initio method

7.1 Introduction

Topological states are of significant interest in condensed matter physics and materials science due to their exotic behavior and potential applications [178–181, 345, 346] These states are protected by symmetries present in the system and based on the symmetry, the system can be topological Insulators (TIs)[347–350], Weyl points[178], Dirac points[182], Topological Superconductors (TSs)[351–354],

and topological nodal lines (NL) semi-metal [355–357] and half metal [358–360] etc. The NL in the electronic band originates from band crossings along the high symmetry points that govern electron transport and can manifest in both quasi-2D and 3D systems. In the presence of the internal magnetic order and spin orbit coupling (SOC), the degeneracy gets lifted and produces the no-zero Berry curvature which induces the anomalous Hall effect (AHE).

Transition metal based double perovskite (DP) oxides, represented by $A_2BB'O_6$ ($A = Ba, Sr, ..; B = Co, Fe, ..; B' = W, Re, ..$) [361, 362], have extremely tunable electronic structure due to possible variation of A, B or B' and this tunability manifest into the diverse type of transport[363, 363–365], magnetic [366–368], and optical properties [364, 369–371]. These systems exhibit numerous crystal symmetries that could play a role in preserving topological degeneracies, which may manifest as points or lines referred to as NL. There are a few theoretical studies on the topological aspect of DP that shows NL and Weyl points [372, 373]. Evidence of topological features in the transition metal DP remained scantly studied in some of the systems like Sr_2FeMoO_6 (SFMO) show a nodal line much above the Fermi-energy E_F [374].

The SFMO systems have been extensively studied and the oxidation state of Fe is 3+ and has five electrons in d-orbitals. Therefore, in large U limit (along with high Hund's coupling) the orbital degrees of freedom are frozen [375, 376]. Thereby a double-exchange (DE) mechanism becomes applicable to account for the ferrimagnetism of SFMO. Besides the semi-classical DE mechanism, multi-orbital Hubbard models have been employed to describe ferromagnetism in DP materials like Sr_2FeReO_6, but they are often limited to Hartree-Fock decoupling methods [377], and transport calculations demonstrating half-metallicity are scarce. Also, another common thread for these ferromagnetic DP materials is the presence of itinerant charge carriers at the $B'(Mo, Re)$ atom, which mediates the long range order and stabilizes a high T_C ($\approx$ 400 K). On the contrary, for Ba_2CoWO_6 (BCWO) system, where Co has seven electrons in the d-orbital, the orbital, charge, and spin all three degrees of freedom are active. Furthermore, the influence of the W atom in BCWO differs from all other DP members discussed above as W does

not have any charge density, but a low T_C FM order indicates charge mobility. For instance in Sr_2FeWO_6, the antibonding W($5d$) states are at higher energy due to hybridization with oxygen p orbitals, leaving W in a $5d^0$ configuration [378]. These observations underscore the need for investigating the BCWO system using the full many-body model Hamiltonian in conjunction with ab initio methods.

In this chapter[1], we execute ab initio calculations to investigate the effect of the electronic band topology and its effect on the transport properties in the BCWO material. This material also shows the interesting magnetic properties which arises due to the quantum many body effect amongst the electrons. The BCWO is a face-centered cubic crystal structure and each of the metal centers are surrounded by the six oxygen forming an octahedral structure as shown in Fig. 7.1a. The octahedral symmetry leads to the lifting of d-orbital degeneracy and splitting it into t_{2g} and e_g orbitals.The d-orbital splitting gap strength and Hund's coupling exchange determines the spin state of Co and also exhibits the correlated nature of the electrons.

The space group of the crystal is $Fm\bar{3}m$ (space group no. 225), which possesses O_h^5 octahedral symmetry and a lattice parameter of a = 8.210 Å[379]. The structure exhibits three mirror planes, illustrated in Fig.7.1(b) resulting in three nodal lines near the Fermi energy (E_F). However, in the presence of the magnetic ordering in a certain direction and spin orbit coupling (SOC) strength, mirror plane symmetries [380] along that direction can be disrupted which lifts the degeneracy along the disrupted symmetry lines. Additionally, we demonstrate that the finite Berry curvature along this gapped line leads to the emergence of the AHE. The competing Hund's and crystal field splitting plays an important role in making this system semi-metal. We use density functional theory to calculate the electronic band structure and use wannierization to find transport properties (see method section in supplemental section[381]). The correlated nature of the system is addressed

[1]This chapter is based on "Emergence of anomalous transverse conductivity in ferromagnetic topological double perovskite Ba_2CoWO_6 due to intrinsic spin-orbit coupling within the multi-orbital Hubbard model and ab initio methods" - J. Sau, S. Chakraborty, S. Saha, K. Pradhan, A. Mukherjee and M. Kumar

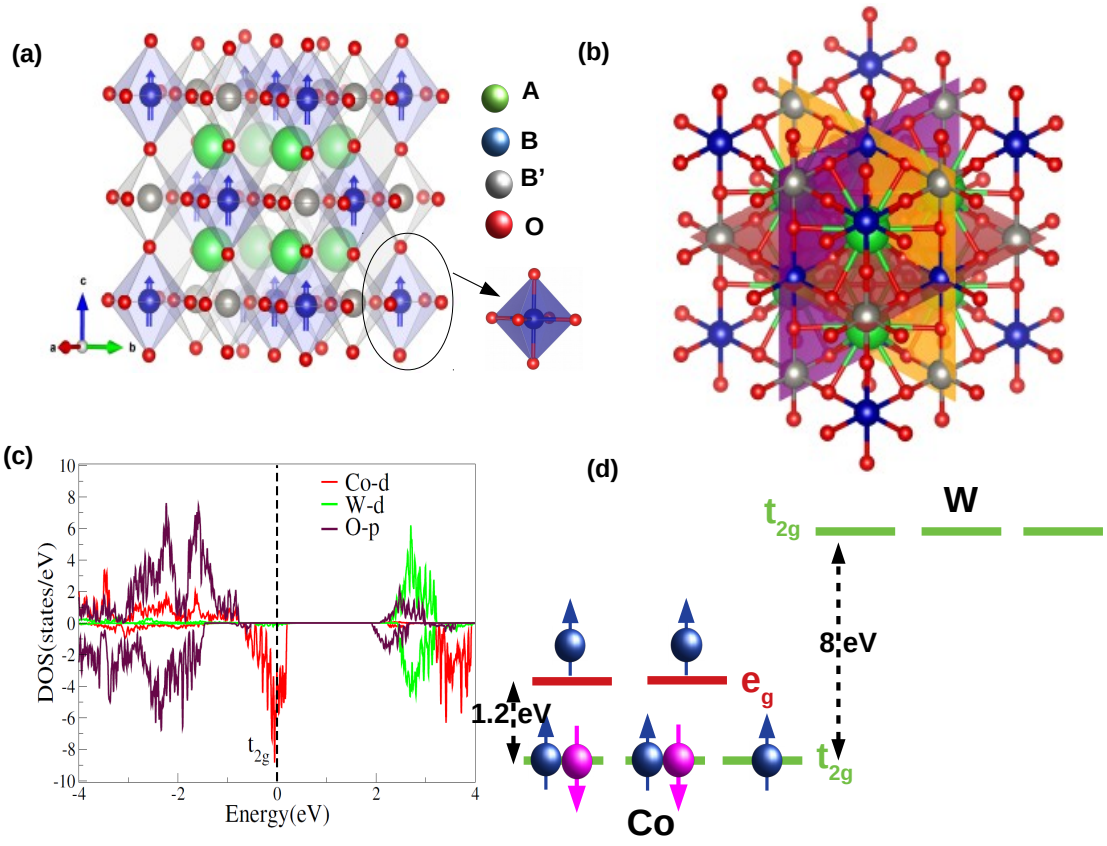

FIGURE 7.1: (a) The $Ba_2BB'O_6$ ($B = Co, Fe; B' = W$) crystal structure where green, blue, gray, and red balls represent Ba, B, B' and O respectively and we have shown the magnetisation (M) direction along [001] by blue arrow. (b) This structure features three distinct mirror planes (M_x, M_y, M_z) .(c) spin-polarized PDOS of Co-d, O-P and W-d orbitals where minority spin channel of Co (t_{2g}) orbitals are itinerant. (d) Schematic Diagram of Magnetic Ground sate Of Ba_2CoWO_6

using both exact diagonalization (ED) and the mean field Monte Carlo (MFMC) method.

7.2 Model

Initially, we analyze the spin-polarized partial density of states (PDOS) to comprehend the involvement of atomic orbitals in BCWO near the Fermi energy (E_F). It is observed that spin-down electrons from the d-orbitals of the Co atoms make a significant contribution, while those from W also contribute to a lesser extent, as depicted in Fig.7.1 (c). The spin-up channel of the PDOS shows a large band gap of 2.5 eV and it can be shown to be a half-metallic system with large DOS

at E_F. The Bader charge analysis indicates that transition atoms are $Co2^+$ ($3d^7$) in the high spin state and $W6^+$ ($5d^0$) with valence spin-magnetic moments of S =3/2 and S = 0, respectively. Consequently, the theoretical total spin magnetic moment is 3.0 μ_B/f.u. for the ferrimagnetic [Co(3d)↑ − W(5d)↓] ground state of Ba_2CoWO_6. The crystal field of oxygen octahedral symmetry splits the five d-orbitals of Co into three t_{2g} at site energy $\Delta_{t_{2g}}$=0 eV and two e_g orbitals with site energy Δ_{e_g}=1.2 eV. The d orbitals of W also split into t_{2g} and e_g orbitals due to identical crystal field splitting. The t_{2g} orbitals of W are positioned at Δ_W=8.0 eV, whereas the e_g levels of W are significantly higher and do not allow for hopping. The wannierization calculations suggest that there are only hopping from the t_{2g} orbitals Co to W and the diagonal hopping matrix is most dominant.

7.3 Hopping Matrix

The hopping matrix which we took in our calculation is given by: t= $\begin{pmatrix} 0.4 & 0.08 & 0.08 \\ 0.08 & 0.4 & 0.08 \\ 0.08 & 0.08 & 0.4 \end{pmatrix}$

It is taken in the basis of $\{d^\dagger_{xz}, d^\dagger_{yz}, d^\dagger_{xy}\}$.Since our Wanieriztion calculation suggest that e_g orbitals are not taking part in the hopping process. So, we are ignoring that hopping.

The multi-band Hubbard model can be written for this system as

$$H = \sum_i H_i + \sum_{<ij>} H_{ij} + \sum_i H_i^{soc} \tag{7.1}$$

Here H_i represents multi-orbital Hamiltonian without hopping for site i, H_{ij} represents the hopping term between the nearest neighbour Co and W atoms and the

H_{SOC} represents the spin-orbit coupling(SOC) term. The H_i can be written as

$$H_i = \sum_{\alpha}(\Delta_{i,\alpha} n_{i,\alpha} + U_i n_{i\uparrow\alpha} n_{i\downarrow\alpha}) + \sum_{\alpha<\beta}(U_i' - \frac{J_{i,H}}{2}) n_{i\alpha} n_{i\beta} \\ -2J_{i,H} \sum_{\alpha<\beta} \mathbf{S}_{i\alpha}.\mathbf{S}_{i\beta} + J'_{i,H} \sum_{\alpha<\beta}(c^{\dagger}_{i\uparrow\alpha} c^{\dagger}_{i\downarrow\alpha} c_{i\downarrow\beta} c_{i\uparrow\beta} + H.c.), \tag{7.2}$$

where $\Delta_{i,\alpha}$ is site energy of ith site and α orbitals and $U_{i,\alpha}$ is Hubbard interaction of site i and α-orbital. $(U_i' - \frac{J_{i,H}}{2})$ is coulomb interaction between the electrons on different orbitals of the same site i. $J_{i,H}$ and $J'_{i,H}$ denote the strengths of Hund's coupling and pair hopping, respectively, between different orbitals at the i^{th} site. Due to symmetry, these terms have equal values. Hence, in our ED calculation, we set $J'_{i,H}$=$J_{i,H}$. For Co sites U_i is taken to be 2.5 eV and $J_{i,H} = 0.25U_i$ and to maintain rotational invariance of orbitals U_i' is set as $U_i - 2J_{i,H}$. For the W atom, an infinitesimal U_i value is considered. The hopping term H_{ij} can be written as

$$H_{ij} = -\sum_{\sigma,\alpha\beta} t_{\alpha,\beta}(c^{\dagger}_{i\sigma\alpha} c_{j\sigma\beta} + H.c.), \tag{7.3}$$

where $t_{\alpha\beta}$ is the hopping strength between the orbital α of i-th Co site and orbital β of j-th W site. $c^{\dagger}_{i\sigma\alpha}$ and $c_{j\sigma\beta}$ are the creation operator of σ spin, at α orbital of i^{th} Co and annihilation operator at β-orbital of j^{th} W. The hopping interaction is restricted to the three t_{2g} orbitals of Co and W as DFT calculations [see Fig.7.2(a)] exhibit that only the t_{2g} electrons are extended. The spin-orbit coupling term is given by,

$$H_i^{soc} = \lambda \mathbf{L}_i.\mathbf{S}_i \equiv \sum_{\alpha,\beta} \lambda_{\alpha,\beta} c^{\dagger}_{i\alpha} c_{i\beta}, \tag{7.4}$$

where λ is a 6x6 matrix, whose matrix elements are written as $\lambda_{\alpha,\beta}$.

We use the MCMF method [382, 383] to solve this model Hamiltonian at finite temperature T and extract the DOS from the model system at very low temperature T = 40 K. The DOS calculated from DFT and the MCMF method are compared in Fig.7.2(a) and (b) for only d-orbitals of Co. In fact, both calculations suggest the semi-metallic behaviour and large band gap in the majority (spin up)

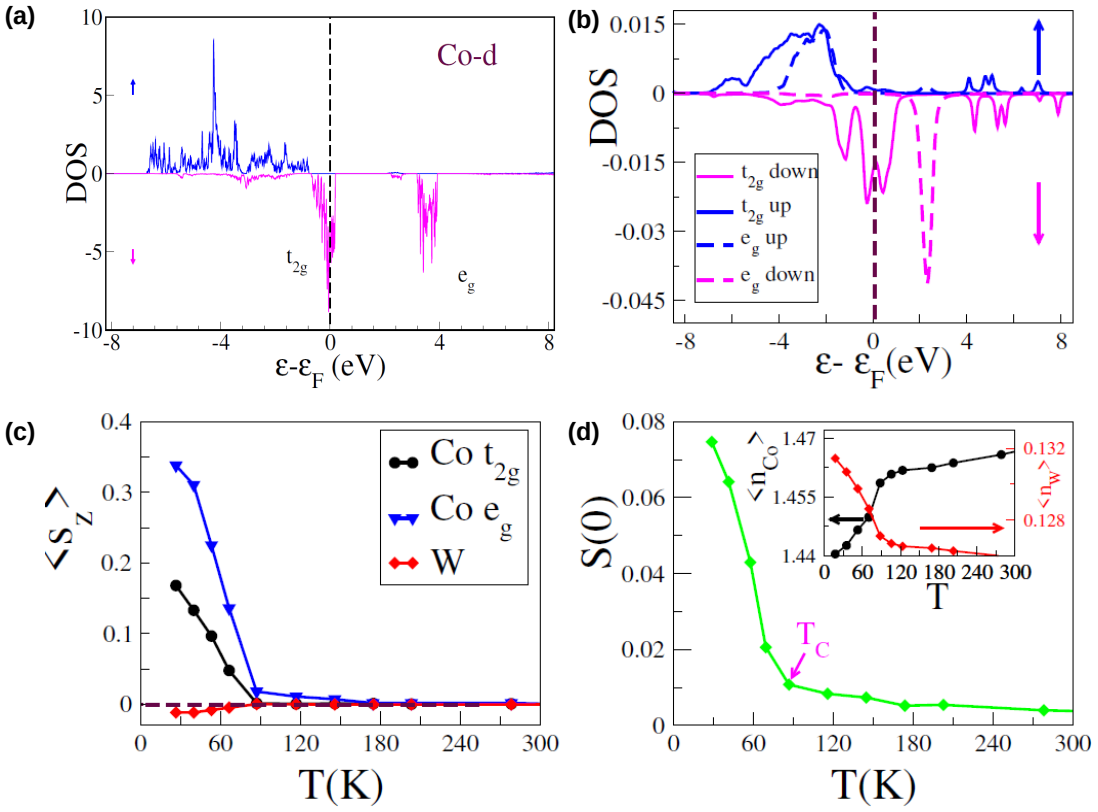

FIGURE 7.2: (a) DFT results for the partial DOS of Co d states of BCWO with Hubbard U, where minority spin carriers participate in conduction and majority spin carriers are entirely gapped. (b) Same as (a) obtained from the 5-orbital Hubbard model study. The contribution of the two e_g and three t_{2g} states are depicted separately. The inset shows the full DOS incorporating both Co and W energy states. (c) The system averaged expectation value of the z-component of total spin operator for Co t_{2g} and e_g states and for W. (d) Ferromagnetic structure factor S(0) vs. temperature for the full system. The average charge density at Co decreases steeply at T_C [see inset], where the charge density at W increases.

channel and only spin down channel is conducting. Two e_g electrons of Co are completely localized and ferromagnetically aligned due to Hund's coupling as the hoping of electrons are only between the t_{2g} orbitals of Co and W. In Fig.7.2(c) averaged total S_z value for each t_{2g} and e_g are 0.16 and 0.38 at $T = 40$ K. The average value of $S_z = 0.16$ at each t_{2g} validates a total average $S_z \approx 1/2$ at t_{2g} of Co and both $< S^z >$ of decrease with increasing T as shown Fig.7.2(c). There is a tiny antiferromagnetically aligned magnetic moment at the W due to fractional down spin charge transfer from Co to W to minimize the Hubbard U cost

at t_{2g} orbitals and avoiding large site energy Δ_W cost at W. Therefore, the spin-down transport channel in this charge transfer system induces a tiny negative S^z value at W sites, which is essential to stabilize the long range order ferromagnetic ordering in the Co. The inset of Fig.7.2(d) shows the double occupancy of t_{2g} increases whereas the density of W decreases with T which results in decreasing the magnetic moment of the system with T. With the knowledge about the spin configurations at each Co and W sites, we calculate the ferromagnetic structure factor S(0) for the whole system, which shows a $T_C = 80K$ [see Fig.7.2(d)].

In order to understand the ground state (gs) properties of the model Hamiltonian in Eq.7.1, first we consider the single site Hamiltonian H_{Co} of Co in Eq.7.2 with all five d-orbitals and seven electrons and perform the exact diagonalization (ED) calculations keeping all parameters same as given above. The gs of H_{Co} is twelve-fold degenerate and effective spin, S_{eff} is 3/2. The twelve-fold degeneracies can come from four-fold spin degeneracy and each of these have three-fold orbital degeneracies. The orbital degeneracy comes because of three possible arrangements of singly occupied electrons in t_{2g} orbitals shown in section II of Supplemental Material[381]. The lowest excited state is a charge transfer state where a down electron goes from doubly occupied t_{2g} orbitals to e_g orbitals. The lowest excitation energy is equal to the difference between t_{2g} and e_g levels. We also notice that if we consider four orbitals i.e. three orbitals of t_{2g} and one e_g the low energy physics remains the same except the effective spin changes to one.

We now try to understand the effect of the hopping term in the Hamiltonian H in Eq.7.1 without SOC and we consider a system of four atoms, two Co and two W, arranged in one dimension shown in Fig.7.4. Each Co has four d-orbitals, three t_{2g} and one e_g orbitals with six electrons and each W atom has three t_{2g} orbitals without any electron. Therefore, The total number of orbitals and electrons are fourteen and twelve respectively. The gs of the system is S=2 and it is five-fold degenerate. In Fig.7.4 charge density $< n_{t_{2g}} >$ and $< S^z_{t_{2g}} >$ of t_{2g} orbitals of Co atoms are 1.543 and 0.19, whereas for Co e_g, $< n_{e_g} >$ and $< S^z_{e_g} >$ are 1 and 0.5 respectively. The charge and spin density at t_{2g} of W are 0.124 and a negative value of 0.022 respectively. The spin densities at Co sites in ED calculations are

Coefficient	*Configuration*
0.243	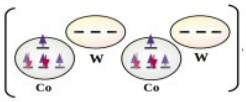
0.107	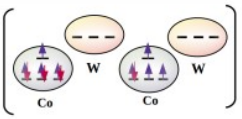
0.089	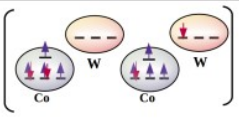
0.043	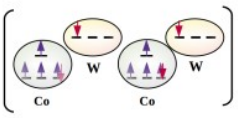
0.041	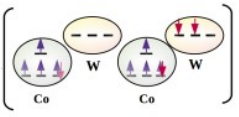
0.040	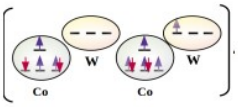
0.024	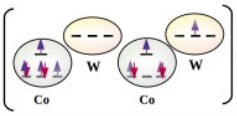

FIGURE 7.3: The schematic of the GS wavefunction and the corresponding spin density and charge density for Co t_{2g}, Co e_g and W t_{2g} for four sites calculated using ED with the same parameters as taken above.

relatively higher than that obtained from the MCMF method, and this may be because of thermal fluctuations and charge density fluctuations in larger systems used in the MCMF method.

The many body effect in ED calculation shows that the gs is a linear combination of many dominant configurations as shown in Fig.7.4. The most dominant configurations have two doubly and one singly occupied t_{2g}-orbitals and singly occupied e_g-orbital of Co, whereas there are no electrons in W, because of large Δ_W and large Hund's coupling the singly occupied orbitals preferred to align all the spins in the same direction. There are $3N_{Co}$ possible configurations due to orbital degeneracy of t_{2g} where N_{Co} is a number of Co sites. Another most probable configuration has all three t_{2g} orbitals doubly occupied and one spin up electron in e_g

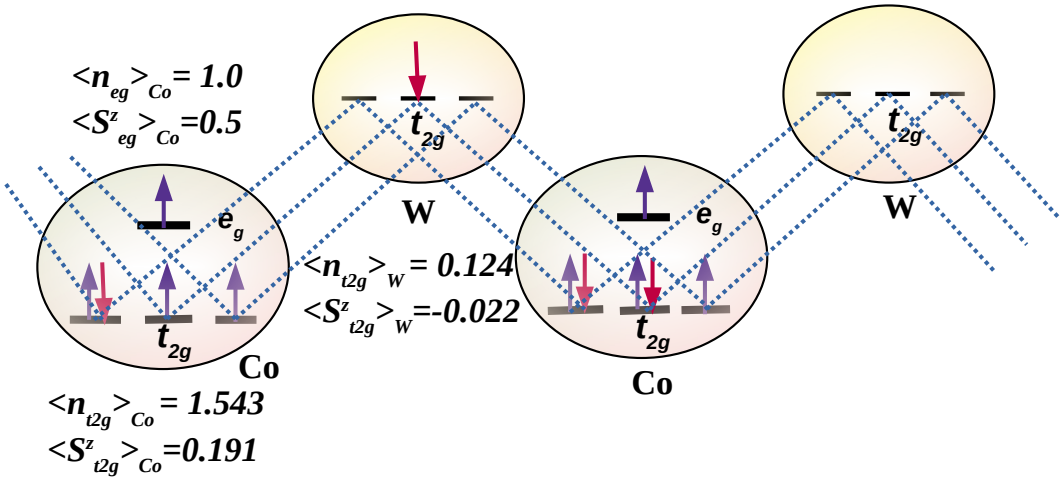

FIGURE 7.4: The schematic of the GS wavefunction and the corresponding spin density and charge density for Co t_{2g}, Co e_g and W t_{2g} for four sites calculated using ED with the same parameters as taken above.

orbitals of Co, whereas, the neighboring Co site has only one t_{2g} orbital which is doubly occupied and the remaining orbitals have one up spin electron. This configuration also carries significant weight in the gs wave function, and the number of configurations goes as $3N_{Co}$. This configuration shows the finite probability for the existence of the Co^{1+} and Co^{3+} and there is a finite probability of an alternate site having the S=1 and 2. Another configuration with third highest probability is where one down spin from a doubly occupied t_{2g} state of Co is transferred to neighbouring W atom and this type of configuration has 24 possibilities. We also note that the direct hopping of electrons from Co to Co leads to antiferromagnetic ordering in the system. Our next objective is to comprehend the impact of SOC on the transport and magnetism in our system, for which we will employ model Hamiltonian and ab initio methods.

7.4 Band Topology

The band dispersion of the spin-polarized band structure of BCWO is calculated using a plane wave-based pseudopotential and the energy dispersion is shown in the absence of the SOC in Fig.7.5(a). The blue and magenta colored bands represent majority and minority spin bands. A linear band crossing point is observed along

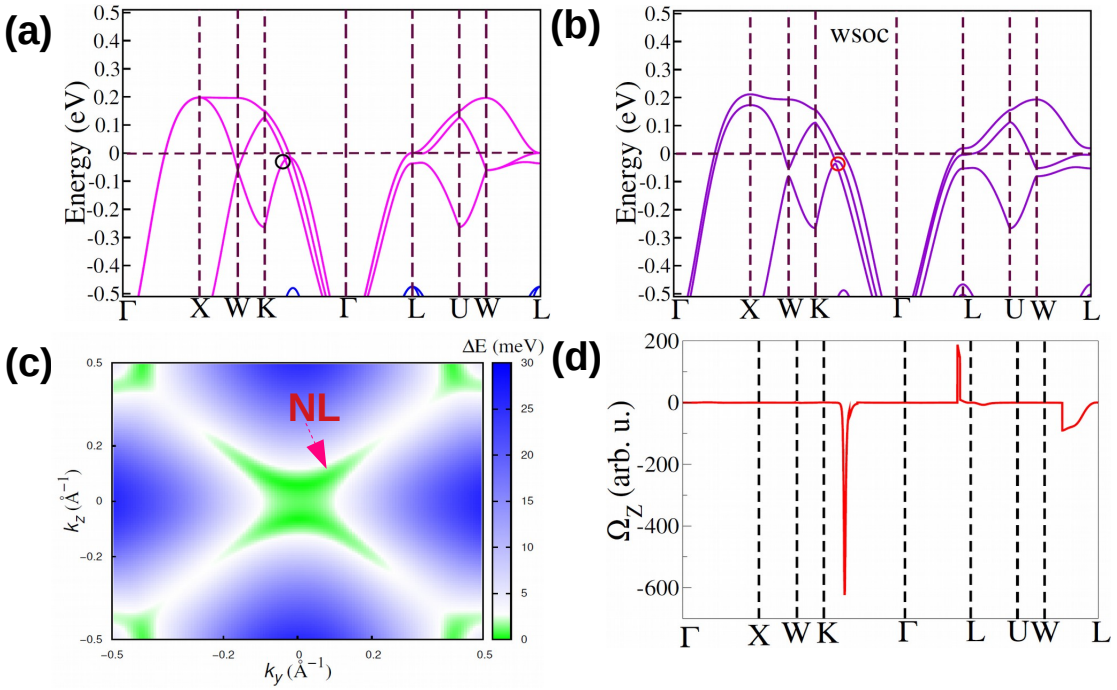

FIGURE 7.5: (a) The band structure of Ba_2BWO_6 without SOC. where the nodal point is indicated by the black circle. (b) The band structure of BCWO with SOC. The gapped nodal lines are shown by a green circle. (c) The energy gap between two intersecting bands in the vicinity of E_F on the K_y-k_z plane, where the black line denotes the nodal line in the absence of SOC. (d) The Berry curvature along the high-symmetry lines due to the nontrivial crossings.

the Γ-K direction, just below the E_F, (The zoom version of the crossing point is shown in Fig.7.6 and this crossing band hybridization between the Co-d_{xz} and Co-d_{yz} orbitals, gives rise to a nodal line-like dispersion. A detailed analysis of the nodal line is provided later. These crossing points are the consequence of the mirror symmetries in the system. We have considered the magnetization axis along the z-direction, therefore, the mirror symmetries perpendicular to the magnetization axis are preserved while the other mirror symmetries parallel to the magnetization axis are broken.

In the presence of the SOC, the spin-orbital mixing leads to the opening of the gap at these degenerate points as shown in Fig.7.5(b) along the high-symmetry point Γ-K. We calculated the Z component of Berry curvature along the same high-symmetry path and noticed that there is a sharp peak of BC along the Γ-K and Γ-L directions and negligible BC in the other directions as shown in Fig.7.5(d). A

gapped nodal line with band inversion, as depicted in Fig.7.6(b), indicates the non-trivial topological nature of the electronic energy band. The non-trivial topology of the electronic bands gives rise to non-zero Berry curvature distribution around the E_F and significantly impacts the conduction electrons for our system.

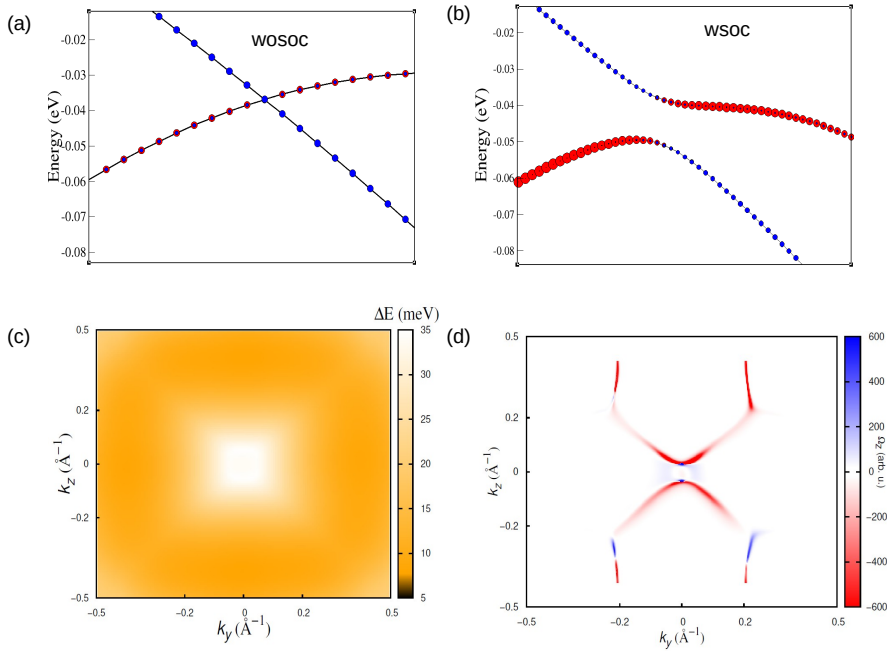

FIGURE 7.6: (a) The zoomed version of the nodal crossing point without SOC (b) The zoomed version of the nodal crossing point in the presence of SOC which shows the band inversion (c)The nodal line is gapped out in the presence of SOC in the K_y-k_z plane, and the gap is represented by a white line. (d) The Berry curvature distribution is displayed in the K_y-k_z plane along the gapped nodal line.

The mirror symmetries of crystal are responsible for the formation of nodal lines in the Brillouin zone (BZ) of the nodal line. These relevant symmetries are the three mirror planes shown in Fig.7.1(b), $M_x(k_x=0)$, $M_y(k_y=0)$, $M_z(k_z=0)$ and three C_4 rotation axes, k_x, k_y and k_z[384]. With the magnetization along the (001) direction and in the presence of spin-orbit coupling, only the $M_z(k_z=0)$ mirror symmetry and the C_{4z} rotational symmetry are preserved. Hence, we expect only a nodal line on the $k_z = 0$ plane to survive. On the other hand, the other two nodal lines on the $k_x = 0$ and $k_y = 0$ planes are gapped out due to the breaking of the respective mirror symmetries. We estimated the energy gap between the lowest conduction and topmost valence bands, which is illustrated in Fig.7.5(c) in the k_x=0 plane where the green line represents a gapless region. The nodal

line is significantly gapped out as shown as a white region in Fig.7.6(c). There is a noticeable significant berry curvature in the k_x=0 and k_y=0 planes because of the small gaps in the neighborhood of the nodal line. The distribution of Berry curvature in the k_x=0 plane is depicted in Fig.7.6(d).

So far we have expounded half-metallicity and emergence of Berry curvature with finite SOC using DOS and band structure calculations. These transport properties can be further examined using Kubo formalism, which is a more robust tool as this consists two body current-current correlations. We compute resistivity (ρ) separately for majority and minority spin channels by evaluating the dc limit of optical (longitudinal) conductivity using thermalized eigenvalues and eigenvectors of the model Hamiltonian in Eq.7.1. In Fig.7.7(a), in the absence of SOC $\lambda = 0$, resistivity further confirms half-metallicity as ρ steeply increases for $T < T_C$ in the majority ($\uparrow$) spin channel, while a sudden drop signifies the onset of metallicity in the minority ($\downarrow$) spin channel. In this phase, spins mainly align along the z-direction, breaking rotational symmetry, resulting in negligible transverse conductivity (σ_{xy}) at finite T. For finite SOC $\lambda \neq 0$, the degeneracy of the t_{2g} levels lifts, causing spin canting and picking up finite x,y components, leading to an increase in σ_{xy} for $T < T_C$ [see Fig.7.7(b)]. Fig.7.7(c) represents a Monte Carlo snapshot of spin configuration and illustrates spin canting with finite λ which is comparable to the previously reported value[385].

In general, half-metallicity results in a notable level of spin polarization, which effectively amplifies the AHE by directing the applied electric current primarily through the metallic spin channel. Consequently, this generates a transverse voltage due to the AHE, resulting in a heightened anomalous Hall conductivity (AHC) in comparison to non-half-metallic ferromagnets possessing similar magnetic characteristics. Numerous theoretical studies have delved into the influence of spin polarization on bolstering the AHC in half-metallic ferromagnets[386–388]. The intrinsic AHC can be evaluated in the linear response theory of Kubo formalism[170]. The 4_{001} symmetry operation is contained in the underlying space group with the magnetization along [001] direction. Upon summing the Berry curvature across the entire Brillouin zone, the relation $\Omega_x = \Omega_y = 0$ is applied to proceed [236]. In

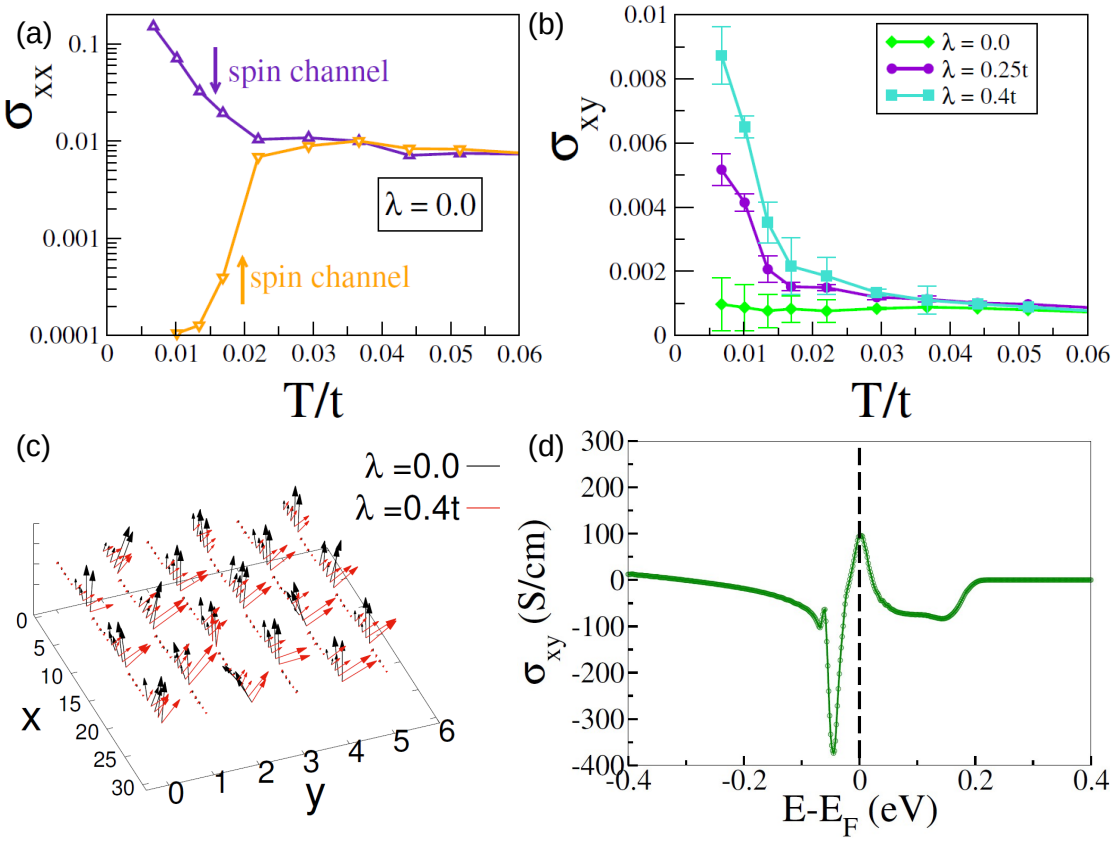

FIGURE 7.7: (a) Resistivity shows insulating and metallic transport for majority and minority spin channels for $T < T_C$. (b) Transverse conductivity increases with increasing SOC (λ) at low temperature. (c) Monte Carlo snapshot of the thermalized spin texture at T/t =0.012 for $\lambda/t = 0$ & 0.4t (d) Energy (E-E_F) dependence of the AHC For BCWO

order to determine the AHC, we integrated the Berry curvature of all the occupied across the entire first BZ. As a result, after the symmetry operation, the AHC's z-component, σ_z^A, is unconstrained, while σ_x^A and σ_y^A likewise disappear. Fig.7.7(d) depicts the fluctuation of AHC with Fermi energy. At the E_F, we calculate the intrinsic AHC (σ_z^A), which is about 100 S/cm.

7.5 Summary

In conclusion, we theoretically study the electronic, magnetic, and anomalous transport properties of double perovskite oxides BCWO using the ab initio DFT, the ED, and the MFMC method. We notice that metals are in Co^{2+} or $3d^7$

and W^{6+} $5d^0$ state and the octahedral symmetry in the system leads to crystal field splitting (CFS) of d-orbitals of Co. Ab initio calculations indicate that only the d-orbitals of Co and W are pertinent, and it is the overlap of t^{2g} orbitals from both atoms that governs transport in the system. We take the full multi-band Hubbard model and show that the interplay of Hund's coupling, Hubbard U, and CFS gap lead to effective spin S=3/2 for Co atom and have three-fold orbital degeneracies in the limit of the MFMC approximation. The presence of unoccupied d-orbitals of W plays a crucial role in ferromagnetic ordering in the system. We also notice the many body gs of this system is complex and lead to various types of dominant configurations such as 7 electrons with S=3/2 spin at Co d-orbital, valance disproportions (6 and electron on neighbouring Co orbitals, and charge transfer of down spin electron to d-orbital of W. We conclude that to achieve the true many-body gs we need to go beyond the Double exchange models. We also note that three symmetry-protected NLs in the first BZ are due to mirror reflection symmetries in the system. The presence of SOC and internal magnetic ordering along the z-direction lead to timer reversal symmetry which introduces finite Berry curvature which leads to interesting AHC. We also investigate the finite temperature effect on the magnetic and transport properties and show our model qualitatively captures the experimentally obtained low T_C value of this material and the onset of half-metallicity at T_C. Lastly, the real-space transverse conductivity finds one to one correspondence with spin canting which provides a mapping with the AHC in momentum space. These new theoretical results help to understand the many body effect and anomalous transport properties of this material.

Bibliography

[1] D. J. Thouless, M. Kohmoto, M. P. Nightingale, and M. den Nijs, Physical review letters **49**, 405 (1982).

[2] E. Tang, J.-W. Mei, and X.-G. Wen, Physical review letters **106**, 236802 (2011).

[3] C. L. Kane and E. J. Mele, Physical review letters **95**, 226801 (2005).

[4] C. L. Kane and E. J. Mele, Physical review letters **95**, 146802 (2005).

[5] B. A. Bernevig, T. L. Hughes, and S.-C. Zhang, science **314**, 1757 (2006).

[6] S.-C. Wu, B. Yan, and C. Felser, Europhysics Letters **107**, 57006 (2014).

[7] J. E. Moore and L. Balents, Physical Review B **75**, 121306 (2007).

[8] R. Roy, Physical Review B **79**, 195322 (2009).

[9] L. Fu, C. L. Kane, and E. J. Mele, Physical review letters **98**, 106803 (2007).

[10] L. Fu and C. L. Kane, Physical Review B **76**, 045302 (2007).

[11] D. Hsieh, D. Qian, L. Wray, Y. Xia, Y. S. Hor, R. J. Cava, and M. Z. Hasan, Nature **452**, 970 (2008).

[12] Y. Hor, P. Roushan, H. Beidenkopf, J. Seo, D. Qu, J. Checkelsky, L. Wray, D. Hsieh, Y. Xia, S.-Y. Xu, *et al.*, Physical Review B **81**, 195203 (2010).

[13] H. Zhang, C.-X. Liu, X.-L. Qi, X. Dai, Z. Fang, and S.-C. Zhang, Nature physics **5**, 438 (2009).

[14] M. Koshino, H. Aoki, and B. I. Halperin, Physical Review B **66**, 081301 (2002).

[15] D. C. Tsui, Reviews of Modern Physics **71**, 891 (1999).

[16] D. C. Tsui, Reviews of Modern Physics **71**, 891 (1999).

[17] L. P. Bouckaert, R. Smoluchowski, and E. Wigner, Physical Review **50**, 58 (1936).

[18] M. Nakahara, *Geometry, topology and physics* (CRC press, 2018).

[19] R. Jackiw and C. Rebbi, Physical Review D **13**, 3398 (1976).

[20] D. Balin *et al.*, JETP lett **42**, 293Ä296 (1985).

[21] E. Fradkin, E. Dagotto, and D. Boyanovsky, Physical review letters **57**, 2967 (1986).

[22] D. B. Kaplan, Physical Review Letters **132**, 141603 (2024).

[23] G. E. Volovik, *The universe in a helium droplet*, Vol. 117 (OUP Oxford, 2003).

[24] M. Berry and M. Tabor, "Proceedings of the royal society of london a: Mathematical, physical and engineering sciences," (1984).

[25] M. Franz and L. Molenkamp, *Topological insulators* (Elsevier, 2013).

[26] S.-Q. SHEN, *Topological Insulators: Dirac Equation in Condensed Matter* (Springer, 2018).

[27] R. Winkler, S. Papadakis, E. De Poortere, and M. Shayegan, *Spin-orbit coupling in two-dimensional electron and hole systems*, Vol. 41 (Springer, 2003).

[28] A. Abragam and B. Bleaney, *Electron paramagnetic resonance of transition ions* (OUP Oxford, 2012).

[29] C. M. Acosta, A. Fazzio, G. M. Dalpian, and A. Zunger, Physical Review B **102**, 144106 (2020).

[30] Y. Tanaka, Z. Ren, T. Sato, K. Nakayama, S. Souma, T. Takahashi, K. Segawa, and Y. Ando, Nature Physics **8**, 800 (2012).

[31] P. Dziawa, B. Kowalski, K. Dybko, R. Buczko, A. Szczerbakow, M. Szot, E. Łusakowska, T. Balasubramanian, B. M. Wojek, M. Berntsen, *et al.*, Nature materials **11**, 1023 (2012).

[32] H. Zhang, C.-X. Liu, X.-L. Qi, X. Dai, Z. Fang, and S.-C. Zhang, Nature physics **5**, 438 (2009).

[33] B. Yan, C.-X. Liu, H.-J. Zhang, C.-Y. Yam, X.-L. Qi, T. Frauenheim, and S.-C. Zhang, Europhysics Letters **90**, 37002 (2010).

[34] T. Zhang, J.-H. Lin, Y.-M. Yu, X.-R. Chen, and W.-M. Liu, Scientific reports **5**, 13927 (2015).

[35] R. Karplus and J. Luttinger, Physical Review **95**, 1154 (1954).

[36] Y. Li and F. Haldane, Physical review letters **120**, 067003 (2018).

[37] S. Onoda, N. Sugimoto, and N. Nagaosa, Physical review B **77**, 165103 (2008).

[38] N. Nagaosa, J. Sinova, S. Onoda, A. H. MacDonald, and N. P. Ong, Reviews of modern physics **82**, 1539 (2010).

[39] M. Onoda, Y. Avishai, and N. Nagaosa, Physical review letters **98**, 076802 (2007).

[40] K. Ahadi, Z. Gui, Z. Porter, J. W. Lynn, Z. Xu, S. D. Wilson, A. Janotti, and S. Stemmer, APL materials **6** (2018).

[41] S. Sangiao, L. Morellon, G. Simon, J. De Teresa, J. Pardo, J. Arbiol, and M. R. Ibarra, Physical Review B **79**, 014431 (2009).

[42] M. Konig, S. Wiedmann, C. Brune, A. Roth, H. Buhmann, L. W. Molenkamp, X.-L. Qi, and S.-C. Zhang, Science **318**, 766 (2007).

[43] S. A. Yang, in *Spin*, Vol. 6 (World Scientific, 2016) p. 1640003.

[44] P. R. Wallace, Physical review **71**, 622 (1947).

[45] N. Armitage, E. Mele, and A. Vishwanath, Reviews of Modern Physics **90**, 015001 (2018).

[46] M. Zahid Hasan, S.-Y. Xu, and M. Neupane, Topological insulators: Fundamentals and perspectives , 55 (2015).

[47] T. Liang, Q. Gibson, M. N. Ali, M. Liu, R. Cava, and N. Ong, Nature materials **14**, 280 (2015).

[48] Y. Zhao, H. Liu, C. Zhang, H. Wang, J. Wang, Z. Lin, Y. Xing, H. Lu, J. Liu, Y. Wang, *et al.*, Physical Review X **5**, 031037 (2015).

[49] H. Wang and J. Wang, Chinese Physics B **27**, 107402 (2018).

[50] S. M. A. Radmanesh, C. Martin, Y. Zhu, X. Yin, H. Xiao, Z. Q. Mao, and L. Spinu, Phys. Rev. B **98**, 241111 (2018).

[51] X. Wan, A. M. Turner, A. Vishwanath, and S. Y. Savrasov, Physical Review B **83**, 205101 (2011).

[52] L. Lu, Z. Wang, D. Ye, L. Ran, L. Fu, J. D. Joannopoulos, and M. Soljačić, Science **349**, 622 (2015).

[53] S.-Y. Xu, I. Belopolski, N. Alidoust, M. Neupane, G. Bian, C. Zhang, R. Sankar, G. Chang, Z. Yuan, C.-C. Lee, *et al.*, Science **349**, 613 (2015).

[54] A. A. Soluyanov, D. Gresch, Z. Wang, Q. Wu, M. Troyer, X. Dai, and B. A. Bernevig, Nature **527**, 495 (2015).

[55] X.-P. Li, K. Deng, B. Fu, Y. Li, D.-S. Ma, J. Han, J. Zhou, S. Zhou, and Y. Yao, Physical Review B **103**, L081402 (2021).

[56] G. Liu, L. Jin, X. Dai, G. Chen, and X. Zhang, Physical Review B **98**, 075157 (2018).

[57] S. Yalameha and Z. Nourbakhsh, Journal of Physics: Condensed Matter **32**, 295502 (2020).

[58] B. Yan and C. Felser, Annual Review of Condensed Matter Physics **8**, 337 (2017).

[59] T. Nguyen, F. Han, N. Andrejevic, R. Pablo-Pedro, A. Apte, Y. Tsurimaki, Z. Ding, K. Zhang, A. Alatas, E. E. Alp, *et al.*, Physical review letters **124**, 236401 (2020).

[60] F. Arnold, C. Shekhar, S.-C. Wu, Y. Sun, R. D. Dos Reis, N. Kumar, M. Naumann, M. O. Ajeesh, M. Schmidt, A. G. Grushin, *et al.*, Nature communications **7**, 11615 (2016).

[61] C. Fang, H. Weng, X. Dai, and Z. Fang, Chinese Physics B **25**, 117106 (2016).

[62] C. Fang, Y. Chen, H.-Y. Kee, and L. Fu, Physical Review B **92**, 081201 (2015).

[63] Y. Shao, Z. Sun, Y. Wang, C. Xu, R. Sankar, A. J. Breindel, C. Cao, M. M. Fogler, A. J. Millis, F. Chou, *et al.*, Proceedings of the National Academy of Sciences **116**, 1168 (2019).

[64] W. Rui, Y. Zhao, and A. P. Schnyder, Physical Review B **97**, 161113 (2018).

[65] A. Burkov and L. Balents, Physical review letters **107**, 127205 (2011).

[66] C. Shekhar, A. K. Nayak, Y. Sun, M. Schmidt, M. Nicklas, I. Leermakers, U. Zeitler, Y. Skourski, J. Wosnitza, Z. Liu, *et al.*, Nature Physics **11**, 645 (2015).

[67] J. Gooth, A. C. Niemann, T. Meng, A. G. Grushin, K. Landsteiner, B. Gotsmann, F. Menges, M. Schmidt, C. Shekhar, V. Süß, *et al.*, Nature **547**, 324 (2017).

[68] N. Morali, R. Batabyal, P. K. Nag, E. Liu, Q. Xu, Y. Sun, B. Yan, C. Felser, N. Avraham, and H. Beidenkopf, Science **365**, 1286 (2019).

[69] M. Hirschberger, S. Kushwaha, Z. Wang, Q. Gibson, S. Liang, C. A. Belvin, B. A. Bernevig, R. J. Cava, and N. P. Ong, Nature materials **15**, 1161 (2016).

[70] W. G. Vandenberghe and M. V. Fischetti, Nature communications **8**, 14184 (2017).

[71] C. M. Acosta and A. Fazzio, Physical Review Letters **122**, 036401 (2019).

[72] J. Liu, T. H. Hsieh, P. Wei, W. Duan, J. Moodera, and L. Fu, Nature materials **13**, 178 (2014).

[73] A. Stern and N. H. Lindner, Science **339**, 1179 (2013).

[74] V. Lahtinen and J. Pachos, SciPost Physics **3**, 021 (2017).

[75] M. Serlin, C. Tschirhart, H. Polshyn, Y. Zhang, J. Zhu, K. Watanabe, T. Taniguchi, L. Balents, and A. Young, Science **367**, 900 (2020).

[76] A. Nozariasbmarz, H. Collins, K. Dsouza, M. H. Polash, M. Hosseini, M. Hyland, J. Liu, A. Malhotra, F. M. Ortiz, F. Mohaddes, *et al.*, Applied Energy **258**, 114069 (2020).

[77] M. M. H. Polash and D. Vashaee, Physical Review Applied **15**, 014011 (2021).

[78] A. Gharleghi, M. M. H. Polash, R. Malekfar, S. A. Yamini, and D. Vashaee, Journal of Alloys and Compounds **845**, 156188 (2020).

[79] M. M. H. Polash and D. Vashaee, Physical Review B **102**, 045202 (2020).

[80] Y. Zheng, T. Lu, M. M. Polash, M. Rasoulianboroujeni, N. Liu, M. E. Manley, Y. Deng, P. Sun, X. Chen, R. P. Hermann, *et al.*, Science advances **5**, eaat9461 (2019).

[81] M. M. H. Polash, F. Mohaddes, M. Rasoulianboroujeni, and D. Vashaee, Journal of Materials Chemistry C **8**, 4049 (2020).

[82] M. M. H. Polash, M. Rasoulianboroujeni, and D. Vashaee, Applied Physics Letters **117** (2020).

[83] N. Xu, Y. Xu, and J. Zhu, npj Quantum Materials **2**, 51 (2017).

[84] O. A. Tretiakov, A. Abanov, and J. Sinova, Applied Physics Letters **99** (2011).

[85] C. Fu, Y. Sun, and C. Felser, APL Materials **8** (2020).

[86] F. Han, N. Andrejevic, T. Nguyen, V. Kozii, Q. T. Nguyen, T. Hogan, Z. Ding, R. Pablo-Pedro, S. Parjan, B. Skinner, *et al.*, Nature communications **11**, 6167 (2020).

[87] M. M. Hasan, M. M. Hossain, and H. K. Chowdhury, Journal of Materials Chemistry A **9**, 3231 (2021).

[88] R. D. Hills, A. Kusmartseva, and F. Kusmartsev, Physical Review B **95**, 214103 (2017).

[89] Y. Wu, C. Li, X. Hu, Y. Ao, Y. Zhao, and Q. Gong, Advanced Optical Materials **5**, 1700357 (2017).

[90] S. A. Hassani Gangaraj, C. Valagiannopoulos, and F. Monticone, Physical Review Research **2**, 023180 (2020).

[91] M. M. H. Polash, M. S. Alam, and S. Biswas, Optical Engineering **57**, 036110 (2018).

[92] M. M. H. Polash, S. Biswas, and M. S. Alam, Applied Physics B **127**, 1 (2021).

[93] L. Šmejkal, Y. Mokrousov, B. Yan, and A. H. MacDonald, Nature physics **14**, 242 (2018).

[94] D. Pesin and A. H. MacDonald, Nature materials **11**, 409 (2012).

[95] M. Sato and Y. Ando, Reports on Progress in Physics **80**, 076501 (2017).

[96] M. Sato, Physics Letters B **575**, 126 (2003).

[97] C. Beenakker, Annu. Rev. Condens. Matter Phys. **4**, 113 (2013).

[98] C. Beenakker, Reviews of Modern Physics **87**, 1037 (2015).

[99] M. Yan, J. Lu, F. Li, W. Deng, X. Huang, J. Ma, and Z. Liu, Nature Materials **17**, 993 (2018).

[100] W. Tian, W. Yu, J. Shi, and Y. Wang, Materials **10**, 814 (2017).

[101] L. Ge, X. Gong, Y. Wang, and S. Xuan, Composites Science and Technology **135**, 92 (2016).

[102] M. Ezawa, Physical review letters **121**, 116801 (2018).

[103] T. M. Chiwewe and G. P. Hancke, IEEE Transactions on Industrial Informatics **8**, 11 (2011).

[104] P. Liu, J. R. Williams, and J. J. Cha, Nature Reviews Materials **4**, 479 (2019).

[105] P. Hohenberg and W. Kohn, Kohn W, Sham LJ (1965) Phys Rev **140**, A1133 (1964).

[106] D. Xiaoying, Mathematica Numerica Sinica **42**, 131 (2020).

[107] W. Kohn, Reviews of Modern Physics **71**, 1253 (1999).

[108] M. Born and R. Oppenheimer, in *Quantum Chemistry: Classic Scientific Papers* (World Scientific, 2000) pp. 1–24.

[109] C. Kittel, (1996).

[110] V. Fock, Zeitschrift für Physik **61**, 126 (1930).

[111] G. Kresse and J. Furthmüller, Physical review B **54**, 11169 (1996).

[112] G. Kresse and J. Furthmüller, Computational materials science **6**, 15 (1996).

[113] L. H. Thomas, in *Mathematical proceedings of the Cambridge philosophical society*, Vol. 23 (Cambridge University Press, 1927) pp. 542–548.

[114] W. Koch and M. C. Holthausen, *A chemist's guide to density functional theory* (John Wiley & Sons, 2015).

[115] P. Hohenberg and W. Kohn, Phys. Rev **136**, B864 (1964).

[116] W. Kohn and L. J. Sham, Physical review **140**, A1133 (1965).

[117] W. Kohn, Reviews of Modern Physics **71**, 1253 (1999).

[118] D. S. Sholl and J. A. Steckel, *Density functional theory: a practical introduction* (John Wiley & Sons, 2022).

[119] E. Wigner, Physical Review **46**, 1002 (1934).

[120] M. Gell-Mann and K. A. Brueckner, Physical Review **106**, 364 (1957).

[121] W. Carr Jr and A. Maradudin, Physical Review **133**, A371 (1964).

[122] S. H. Vosko, L. Wilk, and M. Nusair, Canadian Journal of physics **58**, 1200 (1980).

[123] J. P. Perdew and A. Zunger, Physical review B **23**, 5048 (1981).

[124] L. A. Cole and J. Perdew, Physical Review A **25**, 1265 (1982).

[125] J. P. Perdew and Y. Wang, Physical review B **45**, 13244 (1992).

[126] A. D. Becke, The Journal of chemical physics **96**, 2155 (1992).

[127] J. P. Perdew, K. Burke, and M. Ernzerhof, Physical review letters **77**, 3865 (1996).

[128] K. Kim and K. Jordan, The Journal of Physical Chemistry **98**, 10089 (1994).

[129] F. Bloch, Zeitschrift für physik **52**, 555 (1929).

[130] P. E. Blöchl, Physical review B **50**, 17953 (1994).

[131] O. Andersen and R. Kasowski, Physical Review B **4**, 1064 (1971).

[132] G. H. Wannier, Physical Review **52**, 191 (1937).

[133] N. Marzari and D. Vanderbilt, Physical review B **56**, 12847 (1997).

[134] I. Souza, N. Marzari, and D. Vanderbilt, Physical Review B **65**, 035109 (2001).

[135] T. Graf, C. Felser, and S. S. Parkin, Progress in solid state chemistry **39**, 1 (2011).

[136] P. Canfield, J. Thompson, W. Beyermann, A. Lacerda, M. Hundley, E. Peterson, Z. Fisk, and H. Ott, Journal of applied physics **70**, 5800 (1991).

[137] N. P. Butch, P. Syers, K. Kirshenbaum, A. P. Hope, and J. Paglione, Physical Review B **84**, 220504 (2011).

[138] T. Li, R. Khenata, Z. Cheng, H. Chen, H. Yuan, T. Yang, M. Kuang, S. Bin Omran, and X. Wang, Acta Crystallographica Section B: Structural Science, Crystal Engineering and Materials **74**, 673 (2018).

[139] Y. Nakajima, R. Hu, K. Kirshenbaum, A. Hughes, P. Syers, X. Wang, K. Wang, R. Wang, S. R. Saha, D. Pratt, *et al.*, Science advances **1**, e1500242 (2015).

[140] Z. Fisk, P. Canfield, W. Beyermann, J. Thompson, M. Hundley, H. Ott, E. Felder, M. Maple, M. L. De La Torre, P. Visani, *et al.*, Physical review letters **67**, 3310 (1991).

[141] S. Chadov, X. Qi, J. Kübler, G. H. Fecher, C. Felser, and S. C. Zhang, Nature materials **9**, 541 (2010).

[142] D. Xiao, Y. Yao, W. Feng, J. Wen, W. Zhu, X.-Q. Chen, . f. G. M. Stocks, and Z. Zhang, Physical review letters **105**, 096404 (2010).

[143] H. Lin, L. A. Wray, Y. Xia, S. Xu, S. Jia, R. J. Cava, A. Bansil, and M. Z. Hasan, Nature materials **9**, 546 (2010).

[144] C. Liu, Y. Lee, T. Kondo, E. D. Mun, M. Caudle, B. N. Harmon, S. L. Bud'ko, P. C. Canfield, and A. Kaminski, Physical Review B **83**, 205133 (2011).

[145] W. Wang, Y. Du, G. Xu, X. Zhang, E. Liu, Z. Liu, Y. Shi, J. Chen, G. Wu, and X.-x. Zhang, Scientific reports **3**, 2181 (2013).

[146] C. Shekhar, E. Kampert, T. Förster, B. Yan, A. K. Nayak, M. Nicklas, and C. Felser, arXiv preprint arXiv:1502.00604 (2015).

[147] Z. Liu, L. Yang, S.-C. Wu, C. Shekhar, J. Jiang, H. Yang, Y. Zhang, S.-K. Mo, Z. Hussain, B. Yan, *et al.*, Nature communications **7**, 12924 (2016).

[148] Z. Liu, L. Yang, S.-C. Wu, C. Shekhar, J. Jiang, H. Yang, Y. Zhang, S.-K. Mo, Z. Hussain, B. Yan, *et al.*, Nature communications **7**, 12924 (2016).

[149] R.-L. Chu, W.-Y. Shan, J. Lu, and S.-Q. Shen, Physical Review B **83**, 075110 (2011).

[150] C. Brüne, C. Liu, E. Novik, E. Hankiewicz, H. Buhmann, Y. Chen, X. Qi, Z. Shen, S. Zhang, and L. Molenkamp, Physical Review Letters **106**, 126803 (2011).

[151] S.-C. Wu, B. Yan, and C. Felser, Europhysics Letters **107**, 57006 (2014).

[152] C. Shekhar, N. Kumar, V. Grinenko, S. Singh, R. Sarkar, H. Luetkens, S.-C. Wu, Y. Zhang, A. C. Komarek, E. Kampert, *et al.*, Proceedings of the National Academy of Sciences **115**, 9140 (2018).

[153] M. Hirschberger, S. Kushwaha, Z. Wang, Q. Gibson, S. Liang, C. A. Belvin, B. A. Bernevig, R. J. Cava, and N. P. Ong, Nature materials **15**, 1161 (2016).

[154] Z. Wang, M. Vergniory, S. Kushwaha, M. Hirschberger, E. Chulkov, A. Ernst, N. P. Ong, R. J. Cava, and B. A. Bernevig, Physical review letters **117**, 236401 (2016).

[155] J. Ruan, S.-K. Jian, H. Yao, H. Zhang, S.-C. Zhang, and D. Xing, Nature communications **7**, 11136 (2016).

[156] B. Yan, L. Müchler, and C. Felser, Physical review letters **109**, 116406 (2012).

[157] Z. Wang, A. Alexandradinata, R. J. Cava, and B. A. Bernevig, Nature **532**, 189 (2016).

[158] P. Tang, Q. Zhou, G. Xu, and S.-C. Zhang, Nature Physics **12**, 1100 (2016).

[159] S. Nakatsuji, N. Kiyohara, and T. Higo, Nature **527**, 212 (2015).

[160] A. K. Nayak, J. E. Fischer, Y. Sun, B. Yan, J. Karel, A. C. Komarek, C. Shekhar, N. Kumar, W. Schnelle, J. Kübler, *et al.*, Science advances **2**, e1501870 (2016).

[161] H. Yang, Y. Sun, Y. Zhang, W.-J. Shi, S. S. Parkin, and B. Yan, New Journal of Physics **19**, 015008 (2017).

[162] L. M. Schoop, M. N. Ali, C. Straßer, A. Topp, A. Varykhalov, D. Marchenko, V. Duppel, S. S. Parkin, B. V. Lotsch, and C. R. Ast, Nature communications **7**, 11696 (2016).

[163] S.-Y. Xu, N. Alidoust, G. Chang, H. Lu, B. Singh, I. Belopolski, D. Sanchez, X. Zhang, G. Bian, H. Zheng, *et al.*, arXiv preprint arXiv:1603.07318 (2016).

[164] P. Li, J. Koo, W. Ning, J. Li, L. Miao, L. Min, Y. Zhu, Y. Wang, N. Alem, C.-X. Liu, *et al.*, Nature communications **11**, 3476 (2020).

[165] H. Han, Z. Bai, and K. Yao, Journal of alloys and compounds **576**, 93 (2013).

[166] BL and CHL, Phys Rev B **50**, 17953 (1994).

[167] G. Chang, S.-Y. Xu, H. Zheng, B. Singh, C.-H. Hsu, G. Bian, N. Alidoust, I. Belopolski, D. S. Sanchez, S. Zhang, *et al.*, Scientific reports **6**, 1 (2016).

[168] G. Pizzi, V. Vitale, R. Arita, S. Blügel, F. Freimuth, G. Géranton, M. Gibertini, D. Gresch, C. Johnson, T. Koretsune, J. Ibañez-Azpiroz, H. Lee, J.-M. Lihm, D. Marchand, A. Marrazzo, Y. Mokrousov, J. I. Mustafa, Y. Nohara, Y. Nomura, L. Paulatto, S. Poncé, T. Ponweiser, J. Qiao, F. Thöle, S. S. Tsirkin, M. Wierzbowska, N. Marzari, D. Vanderbilt, I. Souza, A. A. Mostofi, and J. R. Yates, Journal of Physics: Condensed Matter **32**, 165902 (2020).

[169] N. Marzari and D. Vanderbilt, Phys. Rev. B **56**, 12847 (1997).

[170] M. Gradhand, D. V. Fedorov, F. Pientka, P. Zahn, I. Mertig, and B. L. Györffy, Journal of Physics: Condensed Matter **24**, 213202 (2012).

[171] K. Manna, L. Muechler, T.-H. Kao, R. Stinshoff, Y. Zhang, J. Gooth, N. Kumar, G. Kreiner, K. Koepernik, R. Car, *et al.*, Physical Review X **8**, 041045 (2018).

[172] S. Roy, R. Singha, A. Ghosh, A. Pariari, and P. Mandal, Physical Review B **102**, 085147 (2020).

[173] G. K. Shukla, J. Sau, N. Shahi, A. K. Singh, M. Kumar, and S. Singh, Physical Review B **104**, 195108 (2021).

[174] Y. Liu, E. Stavitski, K. Attenkofer, C. Petrovic, *et al.*, Physical Review B **97**, 165415 (2018).

[175] Y. Liu, H. Tan, Z. Hu, B. Yan, C. Petrovic, *et al.*, Physical Review B **103**, 045106 (2021).

[176] S. Chatterjee, J. Sau, S. Samanta, B. Ghosh, N. Kumar, M. Kumar, and K. Mandal, Phys. Rev. B **107**, 125138 (2023).

[177] Z. Zhu, G. W. Winkler, Q. Wu, J. Li, and A. A. Soluyanov, Physical Review X **6**, 031003 (2016).

[178] X. Wan, A. M. Turner, A. Vishwanath, and S. Y. Savrasov, Phys. Rev. B **83**, 205101 (2011).

[179] G. Xu, H. Weng, Z. Wang, X. Dai, and Z. Fang, Phys. Rev. Lett. **107**, 186806 (2011).

[180] N. P. Armitage, E. J. Mele, and A. Vishwanath, Rev. Mod. Phys. **90**, 015001 (2018).

[181] B. Q. Lv, T. Qian, and H. Ding, Rev. Mod. Phys. **93**, 025002 (2021).

[182] S. M. Young, S. Zaheer, J. C. Y. Teo, C. L. Kane, E. J. Mele, and A. M. Rappe, Phys. Rev. Lett. **108**, 140405 (2012).

[183] H. Weng, C. Fang, Z. Fang, and X. Dai, Phys. Rev. B **93**, 241202(R) (2016).

[184] B. Bradlyn, J. Cano, Z. Wang, M. Vergniory, C. Felser, R. J. Cava, and B. A. Bernevig, Science **353**, aaf5037 (2016).

[185] S. Chatterjee, J. Sau, S. Ghosh, S. Samanta, B. Ghosh, M. Kumar, and K. Mandal, Journal of Physics: Condensed Matter **35**, 035601 (2022).

[186] J. Hu, Z. Tang, J. Liu, X. Liu, Y. Zhu, D. Graf, K. Myhro, S. Tran, C. N. Lau, J. Wei, and Z. Mao, Phys. Rev. Lett. **117**, 016602 (2016).

[187] T. Bzdušek, Q. Wu, A. Rüegg, M. Sigrist, and A. A. Soluyanov, Nature **538**, 75 (2016).

[188] Q.-F. Liang, J. Zhou, R. Yu, Z. Wang, and H. Weng, Phys. Rev. B **93**, 085427 (2016).

[189] Z. Wang, H. Weng, Q. Wu, X. Dai, and Z. Fang, Phys. Rev. B **88**, 125427 (2013).

[190] H. Weng, C. Fang, Z. Fang, B. A. Bernevig, and X. Dai, Phys. Rev. X **5**, 011029 (2015).

[191] C. Fang, Y. Chen, H.-Y. Kee, and L. Fu, Phys. Rev. B **92**, 081201(R) (2015).

[192] Z. Yan, R. Bi, H. Shen, L. Lu, S.-C. Zhang, and Z. Wang, Phys. Rev. B **96**, 041103(R) (2017).

[193] K. Manna, L. Muechler, T.-H. Kao, R. Stinshoff, Y. Zhang, J. Gooth, N. Kumar, G. Kreiner, K. Koepernik, R. Car, J. Kübler, G. H. Fecher, C. Shekhar, Y. Sun, and C. Felser, Phys. Rev. X **8**, 041045 (2018).

[194] J. Sau, S. Hassan, N. Kumar, and M. Kumar, Physica Scripta **98**, 125916 (2023).

[195] K. Kim, J. Seo, E. Lee, K.-T. Ko, B. Kim, B. G. Jang, J. M. Ok, J. Lee, Y. J. Jo, W. Kang, *et al.*, Nature materials **17**, 794 (2018).

[196] Y. Li, J. Xia, R. Khenata, and M. Kuang, Materials **13**, 4321 (2020).

[197] Q. Xu, R. Yu, Z. Fang, X. Dai, and H. Weng, Phys. Rev. B **95**, 045136 (2017).

[198] S. Nie, H. Weng, and F. B. Prinz, Phys. Rev. B **99**, 035125 (2019).

[199] L. Berger, Physical Review B **2**, 4559 (1970).

[200] J. Smit, Physica **21**, 877 (1955).

[201] R. Karplus and J. Luttinger, Physical Review **95**, 1154 (1954).

[202] G. Sundaram and Q. Niu, Physical Review B **59**, 14915 (1999).

[203] T. Jungwirth, Q. Niu, and A. MacDonald, Physical review letters **88**, 207208 (2002).

[204] Z. Fang, N. Nagaosa, K. S. Takahashi, A. Asamitsu, R. Mathieu, T. Ogasawara, H. Yamada, M. Kawasaki, Y. Tokura, and K. Terakura, Science **302**, 92 (2003).

[205] Q. Wang, Y. Xu, R. Lou, Z. Liu, M. Li, Y. Huang, D. Shen, H. Weng, S. Wang, and H. Lei, Nature communications **9**, 3681 (2018).

[206] I. Belopolski, K. Manna, D. S. Sanchez, G. Chang, B. Ernst, J. Yin, S. S. Zhang, T. Cochran, N. Shumiya, H. Zheng, *et al.*, Science **365**, 1278 (2019).

[207] J. Noky, Y. Zhang, J. Gooth, C. Felser, and Y. Sun, npj Computational Materials **6**, 77 (2020).

[208] T. P. T. Nguyen and K. Yamauchi, Phys. Rev. B **107**, 155126 (2023).

[209] N. J. Ghimire, A. Botana, J. Jiang, J. Zhang, Y.-S. Chen, and J. Mitchell, Nature communications **9**, 3280 (2018).

[210] Z. Zhao, K. Zhang, Q. Guo, and Y. Jiang, Physica E: Low-dimensional Systems and Nanostructures **138**, 115141 (2022).

[211] K. Manna, L. Muechler, T.-H. Kao, R. Stinshoff, Y. Zhang, J. Gooth, N. Kumar, G. Kreiner, K. Koepernik, R. Car, *et al.*, Physical Review X **8**, 041045 (2018).

[212] P. Li, J. Koo, W. Ning, J. Li, L. Miao, L. Min, Y. Zhu, Y. Wang, N. Alem, C.-X. Liu, *et al.*, Nature communications **11**, 3476 (2020).

[213] A. Sakai, Y. P. Mizuta, A. A. Nugroho, R. Sihombing, T. Koretsune, M.-T. Suzuki, N. Takemori, R. Ishii, D. Nishio-Hamane, R. Arita, *et al.*, Nature Physics **14**, 1119 (2018).

[214] K. Elphick, W. Frost, M. Samiepour, T. Kubota, K. Takanashi, H. Sukegawa, S. Mitani, and A. Hirohata, Science and technology of advanced materials **22**, 235 (2021).

[215] G. K. Shukla, J. Sau, N. Shahi, A. K. Singh, M. Kumar, and S. Singh, Phys. Rev. B **104**, 195108 (2021).

[216] S. Chatterjee, J. Sau, S. Samanta, B. Ghosh, N. Kumar, M. Kumar, and K. Mandal, Phys. Rev. B **107**, 125138 (2023).

[217] J. Noky, Q. Xu, C. Felser, and Y. Sun, Phys. Rev. B **99**, 165117 (2019).

[218] J. Hafner, Journal of computational chemistry **29**, 2044 (2008).

[219] J. P. Perdew and Y. Wang, Phys. Rev. B **45**, 13244 (1992).

[220] K. Nawa and Y. Miura, RSC advances **9**, 30462 (2019).

[221] H. Elmers, S. Wurmehl, G. Fecher, G. Jakob, C. Felser, and G. Schönhense, Journal of magnetism and magnetic materials **272**, 758 (2004).

[222] G. Pizzi, V. Vitale, R. Arita, S. Blügel, F. Freimuth, G. Géranton, M. Gibertini, D. Gresch, C. Johnson, T. Koretsune, *et al.*, Journal of Physics: Condensed Matter **32**, 165902 (2020).

[223] N. Marzari and D. Vanderbilt, Phys. Rev. B **56**, 12847 (1997).

[224] Q. Wu, S. Zhang, H.-F. Song, M. Troyer, and A. A. Soluyanov, Computer Physics Communications **224**, 405 (2018).

[225] D. Bombor, C. G. F. Blum, O. Volkonskiy, S. Rodan, S. Wurmehl, C. Hess, and B. Büchner, Phys. Rev. Lett. **110**, 066601 (2013).

[226] I. Galanakis, P. H. Dederichs, and N. Papanikolaou, Phys. Rev. B **66**, 174429 (2002).

[227] A. P. Malozemoff, A. R. Williams, and V. L. Moruzzi, Phys. Rev. B **29**, 1620 (1984).

[228] I.-M. Imort, P. Thomas, G. Reiss, and A. Thomas, Journal of Applied Physics **111**, 07D313 (2012).

[229] H. Xiao, R. Wang, L. Xu, F. Yang, and C. Yang, Physics Letters A **382**, 224 (2018).

[230] M. Jubair, A. Tanveer Karim, M. Nuruzzaman, M. Roknuzzaman, and M. Zilani, Heliyon **7**, e08585 (2021).

[231] S. Gupta, J. Sau, M. Kumar, and C. Mazumdar, arXiv preprint arXiv:2303.08589 (2023).

[232] J. Zou, Z. He, and G. Xu, npj Computational Materials **5,**, 96 (2019).

[233] S. Cheng, H. Yin, Z. Lu, C. He, P. Wang, and G. Xianlong, Phys. Rev. A **101**, 043620 (2020).

[234] K. Sacha, Phys. Rev. A **91**, 033617 (2015).

[235] B. Dey and T. K. Ghosh, Phys. Rev. B **99**, 205429 (2019).

[236] I. Samathrakis, N. Fortunato, H. K. Singh, C. Shen, and H. Zhang, Journal of Physics: Condensed Matter **51**, 025703 (2022).

[237] A. Sakai, Y. P. Mizuta, A. A. Nugroho, R. Sihombing, T. Koretsune, M.-T. Suzuki, N. Takemori, R. Ishii, D. Nishio-Hamane, R. Arita, *et al.*, Nature Physics **14**, 1119 (2018).

[238] T. Asaba, V. Ivanov, S. Thomas, S. Savrasov, J. Thompson, E. Bauer, and F. Ronning, Science Advances **7**, eabf1467 (2021).

[239] T. Chen, T. Tomita, S. Minami, M. Fu, T. Koretsune, M. Kitatani, I. Muhammad, D. Nishio-Hamane, R. Ishii, F. Ishii, *et al.*, Nature communications **12**, 572 (2021).

[240] Y. Wang, C. Xian, J. Wang, B. Liu, L. Ling, L. Zhang, L. Cao, Z. Qu, and Y. Xiong, Physical Review B **96**, 134428 (2017).

[241] J.-X. Yin, S. S. Zhang, G. Chang, Q. Wang, S. S. Tsirkin, Z. Guguchia, B. Lian, H. Zhou, K. Jiang, I. Belopolski, *et al.*, Nature Physics **15**, 443 (2019).

[242] S. Nakatsuji, N. Kiyohara, and T. Higo, Nature **527**, 212 (2015).

[243] L. Ye, M. Kang, J. Liu, F. Von Cube, C. R. Wicker, T. Suzuki, C. Jozwiak, A. Bostwick, E. Rotenberg, D. C. Bell, *et al.*, Nature **555**, 638 (2018).

[244] M. Kang, S. Fang, L. Ye, H. C. Po, J. Denlinger, C. Jozwiak, A. Bostwick, E. Rotenberg, E. Kaxiras, J. G. Checkelsky, *et al.*, Nature communications **11**, 4004 (2020).

[245] Z. Lin, J.-H. Choi, Q. Zhang, W. Qin, S. Yi, P. Wang, L. Li, Y. Wang, H. Zhang, Z. Sun, *et al.*, Physical review letters **121**, 096401 (2018).

[246] Z. Guguchia, R. Khasanov, and H. Luetkens, npj Quantum Materials **8**, 41 (2023).

[247] Y. Wang, H. Wu, G. T. McCandless, J. Y. Chan, and M. N. Ali, Nature Reviews Physics **5**, 635 (2023).

[248] B. Keimer and J. Moore, Nature Physics **13**, 1045 (2017).

[249] S. Sachdev, Reports on Progress in Physics **82**, 014001 (2018).

[250] M. Z. Hasan, S.-Y. Xu, and G. Bian, Physica Scripta **2015**, 014001 (2015).

[251] K. He, Y. Wang, and Q.-K. Xue, Annual Review of Condensed Matter Physics **9**, 329 (2018).

[252] M. Franz and M. Rozali, Nature Reviews Materials **3**, 491 (2018).

[253] N. Armitage, E. Mele, and A. Vishwanath, Reviews of Modern Physics **90**, 015001 (2018).

[254] J.-X. Yin, W. Ma, T. A. Cochran, X. Xu, S. S. Zhang, H.-J. Tien, N. Shumiya, G. Cheng, K. Jiang, B. Lian, *et al.*, Nature **583**, 533 (2020).

[255] D. J. Thouless, M. Kohmoto, M. P. Nightingale, and M. den Nijs, Physical review letters **49**, 405 (1982).

[256] F. D. M. Haldane, Physical review letters **61**, 2015 (1988).

[257] A. L. Sharpe, E. J. Fox, A. W. Barnard, J. Finney, K. Watanabe, T. Taniguchi, M. Kastner, and D. Goldhaber-Gordon, Science **365**, 605 (2019).

[258] J. Zou, Z. He, and G. Xu, npj Computational Materials **5**, 96 (2019).

[259] E. Tang, J.-W. Mei, and X.-G. Wen, Physical review letters **106**, 236802 (2011).

[260] G. Xu, B. Lian, and S.-C. Zhang, Physical review letters **115**, 186802 (2015).

[261] M. Kang, L. Ye, S. Fang, J.-S. You, A. Levitan, M. Han, J. I. Facio, C. Jozwiak, A. Bostwick, E. Rotenberg, *et al.*, Nature materials **19**, 163 (2020).

[262] I. Mazin, H. O. Jeschke, F. Lechermann, H. Lee, M. Fink, R. Thomale, and R. Valentí, Nature communications **5**, 4261 (2014).

[263] M. Li, Q. Wang, G. Wang, Z. Yuan, W. Song, R. Lou, Z. Liu, Y. Huang, Z. Liu, H. Lei, *et al.*, Nature communications **12**, 3129 (2021).

[264] D. Boyko, A. Saxena, and J. T. Haraldsen, Annalen der Physik **532**, 1900350 (2020).

[265] Y. Hu, X. Wu, B. R. Ortiz, S. Ju, X. Han, J. Ma, N. C. Plumb, M. Radovic, R. Thomale, S. D. Wilson, *et al.*, Nature Communications **13**, 2220 (2022).

[266] H. Tasaki, Physical review letters **69**, 1608 (1992).

[267] A. Mielke, Journal of Physics A: Mathematical and General **24**, 3311 (1991).

[268] S. Peotta and P. Törmä, Nature communications **6**, 8944 (2015).

[269] M. Imada and M. Kohno, Physical Review Letters **84**, 143 (2000).

[270] C. Wu, D. Bergman, L. Balents, and S. D. Sarma, Physical review letters **99**, 070401 (2007).

[271] T. Neupert, L. Santos, C. Chamon, and C. Mudry, Physical review letters **106**, 236804 (2011).

[272] X. Zhu, W. Han, S. Feng, and H. Guo, Phys. Rev. Res. **5**, 023037 (2023).

[273] X. Zhu, W. Han, S. Feng, and H. Guo, Physical Review Research **5**, 023037 (2023).

[274] R. Samajdar, W. W. Ho, H. Pichler, M. D. Lukin, and S. Sachdev, Proceedings of the National Academy of Sciences **118**, e2015785118 (2021).

[275] S. Lee, C. Won, J. Kim, J. Yoo, S. Park, J. Denlinger, C. Jozwiak, A. Bostwick, E. Rotenberg, R. Comin, *et al.*, npj Quantum Materials **9**, 15 (2024).

[276] S. Ghosh, P. O'Brien, C. L. Henley, and M. J. Lawler, Physical Review B **93**, 024401 (2016).

[277] Q. Wang, S. Sun, X. Zhang, F. Pang, H. Lei, *et al.*, Physical Review B **94**, 075135 (2016).

[278] J.-X. Yin, S. S. Zhang, H. Li, K. Jiang, G. Chang, B. Zhang, B. Lian, C. Xiang, I. Belopolski, H. Zheng, *et al.*, Nature **562**, 91 (2018).

[279] E. Liu, Y. Sun, N. Kumar, L. Muechler, A. Sun, L. Jiao, S.-Y. Yang, D. Liu, A. Liang, Q. Xu, *et al.*, Nature physics **14**, 1125 (2018).

[280] Q. Wang, Y. Xu, R. Lou, Z. Liu, M. Li, Y. Huang, D. Shen, H. Weng, S. Wang, and H. Lei, Nature communications **9**, 3681 (2018).

[281] J.-X. Yin, S. S. Zhang, G. Chang, Q. Wang, S. S. Tsirkin, Z. Guguchia, B. Lian, H. Zhou, K. Jiang, I. Belopolski, *et al.*, Nature Physics **15**, 443 (2019).

[282] A. K. Nayak, J. E. Fischer, Y. Sun, B. Yan, J. Karel, A. C. Komarek, C. Shekhar, N. Kumar, W. Schnelle, J. Kübler, *et al.*, Science advances **2**, e1501870 (2016).

[283] N. Kiyohara, T. Tomita, and S. Nakatsuji, Phys. Rev. Appl. **5**, 064009 (2016).

[284] D. Chen, C. Le, C. Fu, H. Lin, W. Schnelle, Y. Sun, and C. Felser, Physical Review B **103**, 144410 (2021).

[285] Q. Wang, K. J. Neubauer, C. Duan, Q. Yin, S. Fujitsu, H. Hosono, F. Ye, R. Zhang, S. Chi, K. Krycka, *et al.*, Physical Review B **103**, 014416 (2021).

[286] W. Ma, X. Xu, J.-X. Yin, H. Yang, H. Zhou, Z.-J. Cheng, Y. Huang, Z. Qu, F. Wang, M. Z. Hasan, *et al.*, Physical review letters **126**, 246602 (2021).

[287] Y. Lee, R. Skomski, X. Wang, P. Orth, Y. Ren, B. Kang, A. Pathak, A. Kutepov, B. Harmon, R. McQueeney, *et al.*, Physical Review B **108**, 045132 (2023).

[288] A. Smiri, S. Jaziri, S. Lounis, and I. C. Gerber, Physical Review Materials **5**, 054001 (2021).

[289] P. Blaha, K. Schwarz, F. Tran, R. Laskowski, G. K. H. Madsen, and L. D. Marks, The Journal of Chemical Physics **152**, 074101 (2020), https://doi.org/10.1063/1.5143061 .

[290] M. Aichhorn, L. Pourovskii, V. Vildosola, M. Ferrero, O. Parcollet, T. Miyake, A. Georges, and S. Biermann, Phys. Rev. B **80**, 085101 (2009).

[291] M. Aichhorn, L. Pourovskii, and A. Georges, Phys. Rev. B **84**, 054529 (2011).

[292] M. Aichhorn, L. Pourovskii, P. Seth, V. Vildosola, M. Zingl, O. E. Peil, X. Deng, J. Mravlje, G. J. Kraberger, C. Martins, M. Ferrero, and O. Parcollet, Computer Physics Communications **204**, 200 (2016).

[293] O. Parcollet, M. Ferrero, T. Ayral, H. Hafermann, I. Krivenko, L. Messio, and P. Seth, Computer Physics Communications **196**, 398 (2015).

[294] P. Werner and A. J. Millis, Phys. Rev. B **74**, 155107 (2006).

[295] P. Seth, I. Krivenko, M. Ferrero, and O. Parcollet, Computer Physics Communications **200**, 274 (2016).

[296] K. Held, Advances in Physics **56**, 829 (2007).

[297] P. Wissgott, A. Toschi, H. Usui, K. Kuroki, and K. Held, Phys. Rev. B **82**, 201106 (2010).

[298] H. Banerjee, C. P. Grey, and A. J. Morris, Phys. Rev. B **108**, 165124 (2023).

[299] H. Banerjee and M. Aichhorn, Phys. Rev. B **101**, 241112 (2020).

[300] G. J. Kraberger, R. Triebl, M. Zingl, and M. Aichhorn, Phys. Rev. B **96**, 155128 (2017).

[301] C. Chen, J. Zheng, R. Yu, S. Sankar, K. T. Law, H. C. Po, and B. Jäck, Physical Review Research **5**, 043269 (2023).

[302] H. Banerjee, H. Schnait, M. Aichhorn, and T. Saha-Dasgupta, Phys. Rev. B **105**, 235106 (2022).

[303] T. Mazet, G. Venturini, R. Welter, and B. Malaman, Journal of alloys and compounds **264**, 71 (1998).

[304] S. Youn, B. Min, and A. J. Freeman, physica status solidi (b) **241**, 1411 (2004).

[305] L. Fu and C. L. Kane, Physical Review B **76**, 045302 (2007).

[306] G. Guo, Y. Yao, and Q. Niu, Physical review letters **94**, 226601 (2005).

[307] G.-Y. Guo, S. Murakami, T.-W. Chen, and N. Nagaosa, Physical review letters **100**, 096401 (2008).

[308] X.-L. Qi and S.-C. Zhang, Rev. Mod. Phys. **83**, 1057 (2011).

[309] A. Kitaev, in *AIP conference proceedings*, Vol. 1134 (American Institute of Physics, 2009) pp. 22–30.

[310] S. Ryu, A. P. Schnyder, A. Furusaki, and A. W. Ludwig, New Journal of Physics **12**, 065010 (2010).

[311] M. Koshino, T. Morimoto, and M. Sato, Physical Review B **90**, 115207 (2014).

[312] P. Hořava, Physical review letters **95**, 016405 (2005).

[313] G. E. Volovik, in *Analogue Gravity Phenomenology* (Springer, 2013) pp. 343–383.

[314] A. Lau and C. Timm, Physical Review B **88**, 165402 (2013).

[315] Y. Ran, F. Wang, H. Zhai, A. Vishwanath, and D.-H. Lee, Physical Review B **79**, 014505 (2009).

[316] J.-M. Hou, Physical Review Letters **111**, 130403 (2013).

[317] K.-I. Kobayashi, T. Kimura, Y. Tomioka, H. Sawada, K. Terakura, and Y. Tokura, Phys. Rev. B **59**, 11159 (1999).

[318] A. A. Burkov, M. D. Hook, and L. Balents, Phys. Rev. B **84**, 235126 (2011).

[319] C.-K. Chiu and A. P. Schnyder, Phys. Rev. B **90**, 205136 (2014).

[320] H. Weng, C. Fang, Z. Fang, B. A. Bernevig, and X. Dai, Phys. Rev. X **5**, 011029 (2015).

[321] S.-M. Huang, S.-Y. Xu, I. Belopolski, C.-C. Lee, G. Chang, B. Wang, N. Alidoust, G. Bian, M. Neupane, C. Zhang, *et al.*, Nature communications **6**, 1 (2015).

[322] J.-M. Carter, V. V. Shankar, M. A. Zeb, and H.-Y. Kee, Phys. Rev. B **85**, 115105 (2012).

[323] C. Fang, H. Weng, X. Dai, and Z. Fang, Chinese Physics B **25**, 117106 (2016).

[324] D. Xiao, Y. Yao, Z. Fang, and Q. Niu, Phys. Rev. Lett. **97**, 026603 (2006).

[325] G. K. Shukla, J. Sau, V. Kumar, M. Kumar, and S. Singh, Phys. Rev. B **106**, 045131 (2022).

[326] H. Chen, H. Yang, B. Hu, Z. Zhao, J. Yuan, Y. Xing, G. Qian, Z. Huang, G. Li, Y. Ye, *et al.*, Nature **599**, 222 (2021).

[327] J. Seo, D. Y. Kim, E. S. An, K. Kim, G.-Y. Kim, S.-Y. Hwang, D. W. Kim, B. G. Jang, H. Kim, G. Eom, *et al.*, Science advances **6**, eaay8912 (2020).

[328] A. F. May, D. Ovchinnikov, Q. Zheng, R. Hermann, S. Calder, B. Huang, Z. Fei, Y. Liu, X. Xu, and M. A. McGuire, ACS nano **13**, 4436 (2019).

[329] Y. Deng, Y. Yu, M. Z. Shi, Z. Guo, Z. Xu, J. Wang, X. H. Chen, and Y. Zhang, Science **367**, 895 (2020).

[330] S. Mondal, N. Khan, S. M. Mishra, B. Satpati, and P. Mandal, Phys. Rev. B **104**, 094405 (2021).

[331] M. Ribeiro, G. Gentile, A. Marty, D. Dosenovic, H. Okuno, C. Vergnaud, J.-F. Jacquot, D. Jalabert, D. Longo, P. Ohresser, *et al.*, npj 2D Materials and Applications **6**, 1 (2022).

[332] B. Liu, S. Liu, L. Yang, Z. Chen, E. Zhang, Z. Li, J. Wu, X. Ruan, F. Xiu, W. Liu, L. He, R. Zhang, and Y. Xu, Phys. Rev. Lett. **125**, 267205 (2020).

[333] Y. Zhang, H. Lu, X. Zhu, S. Tan, W. Feng, Q. Liu, W. Zhang, Q. Chen, Y. Liu, X. Luo, *et al.*, Science advances **4**, eaao6791 (2018).

[334] D. Kim, C. Lee, B. G. Jang, K. Kim, and J. H. Shim, Scientific Reports **11**, 1 (2021).

[335] Y. Yao, L. Kleinman, A. H. MacDonald, J. Sinova, T. Jungwirth, D.-s. Wang, E. Wang, and Q. Niu, Phys. Rev. Lett. **92**, 037204 (2004).

[336] M. N. Ali, L. M. Schoop, C. Garg, J. M. Lippmann, E. Lara, B. Lotsch, and S. S. Parkin, Science advances **2**, e1601742 (2016).

[337] C. Gong and X. Zhang, Science **363**, eaav4450 (2019).

[338] K. S. Burch, D. Mandrus, and J.-G. Park, Nature **563**, 47 (2018).

[339] T. Song, M. W.-Y. Tu, C. Carnahan, X. Cai, T. Taniguchi, K. Watanabe, M. A. McGuire, D. H. Cobden, D. Xiao, W. Yao, *et al.*, Nano Letters **19**, 915 (2019).

[340] P. Blöchl, Phys. Rev. B **50**, 17953 (1994).

[341] J. P. Perdew, K. Burke, and M. Ernzerhof, Phys. Rev. Lett. **77**, 3865 (1996).

[342] Z. Li, W. Xia, H. Su, Z. Yu, Y. Fu, L. Chen, X. Wang, N. Yu, Z. Zou, and Y. Guo, Scientific reports **10**, 1 (2020).

[343] H. Watanabe, H. C. Po, and A. Vishwanath, Science advances **4**, eaat8685 (2018).

[344] J. Xu, W. A. Phelan, and C.-L. Chien, Nano Letters **19**, 8250 (2019).

[345] C. Nayak, S. H. Simon, A. Stern, M. Freedman, and S. Das Sarma, Rev. Mod. Phys. **80**, 1083 (2008).

[346] A. Stern and N. H. Lindner, Science **339**, 1179 (2013), https://www.science.org/doi/pdf/10.1126/science.1231473 .

[347] S. Murakami, N. Nagaosa, and S.-C. Zhang, Phys. Rev. Lett. **93**, 156804 (2004).

[348] C. L. Kane and E. J. Mele, Phys. Rev. Lett. **95**, 226801 (2005).

[349] X.-L. Qi, Y.-S. Wu, and S.-C. Zhang, Phys. Rev. B **74**, 085308 (2006).

[350] B. A. Bernevig, T. L. Hughes, and S.-C. Zhang, Science **314**, 1757 (2006), https://www.science.org/doi/pdf/10.1126/science.1133734 .

[351] C. Kallin, Reports on Progress in Physics **75**, 042501 (2012).

[352] C. Kallin and A. Berlinsky, Journal of Physics: Condensed Matter **21**, 164210 (2009).

[353] Y. S. Hor, A. J. Williams, J. G. Checkelsky, P. Roushan, J. Seo, Q. Xu, H. W. Zandbergen, A. Yazdani, N. P. Ong, and R. J. Cava, Physical review letters **104**, 057001 (2010).

[354] L. Fu and E. Berg, Physical review letters **105**, 097001 (2010).

[355] C. Fang, H. Weng, X. Dai, and Z. Fang, Chinese Physics B **25**, 117106 (2016).

[356] C. Fang, Y. Chen, H.-Y. Kee, and L. Fu, Physical Review B **92**, 081201 (2015).

[357] Q. Xu, R. Yu, Z. Fang, X. Dai, and H. Weng, Physical Review B **95**, 045136 (2017).

[358] R.-W. Zhang, D.-S. Ma, J.-M. Zhang, and Y. Yao, Phys. Rev. B **103**, 195115 (2021).

[359] T. He, X. Zhang, L. Wang, Y. Liu, X. Dai, L. Wang, and G. Liu, Materials Today Physics **17**, 100360 (2021).

[360] G. Chang, S.-Y. Xu, H. Zheng, B. Singh, C.-H. Hsu, G. Bian, N. Alidoust, I. Belopolski, D. S. Sanchez, S. Zhang, *et al.*, Scientific reports **6**, 38839 (2016).

[361] J. B. Philipp, P. Majewski, L. Alff, A. Erb, R. Gross, T. Graf, M. S. Brandt, J. Simon, T. Walther, W. Mader, D. Topwal, and D. D. Sarma, Phys. Rev. B **68**, 144431 (2003).

[362] A. Halder, S. Das, P. Sanyal, and T. Saha-Dasgupta, Scientific reports **11**, 21764 (2021).

[363] S. Ghorui, J. Kangsabanik, M. Aslam, and A. Alam, Phys. Rev. Appl. **21**, 024036 (2024).

[364] R. Parida, D. Pattanayak, B. Mohanty, and B. Parida, Journal of Molecular Structure **1205**, 127607 (2020).

[365] S. Chanda, S. Saha, A. Dutta, and T. Sinha, Materials Research Bulletin **62**, 153 (2015).

[366] K. Yamamura, M. Wakeshima, and Y. Hinatsu, Journal of solid state chemistry **179**, 605 (2006).

[367] K. Yoshimatsu, K. Nogami, K. Watarai, K. Horiba, H. Kumigashira, O. Sakata, T. Oshima, and A. Ohtomo, Physical Review B **91**, 054421 (2015).

[368] A. Nid-Bahami, A. El Kenz, A. Benyoussef, L. Bahmad, M. Hamedoun, and H. El Moussaoui, Journal of Magnetism and Magnetic Materials **417**, 258 (2016).

[369] D. Pattanayak, R. Parida, N. C. Nayak, A. Panda, and B. Parida, Journal of Materials Science: Materials in Electronics **29**, 6215 (2018).

[370] L. Boudad, M. Taibi, A. Belayachi, and M. Abd-Lefdil, RSC advances **11**, 40205 (2021).

[371] L. Schade, A. D. Wright, R. D. Johnson, M. Dollmann, B. Wenger, P. K. Nayak, D. Prabhakaran, L. M. Herz, R. Nicholas, H. J. Snaith, *et al.*, ACS Energy Letters **4**, 299 (2018).

[372] X. Zhao, P.-j. Guo, F. Ma, and Z.-Y. Lu, Physical Review B **103**, 085138 (2021).

[373] K. Samanta, J. Noky, I. Robredo, J. Kuebler, M. G. Vergniory, and C. Felser, npj Computational Materials **9**, 167 (2023).

[374] T. Chakraborty, K. Samanta, S. N. Guin, J. Noky, I. n. Robredo, S. Prasad, J. Kuebler, C. Shekhar, M. G. Vergniory, and C. Felser, Phys. Rev. B **106**, 155141 (2022).

[375] D. D. Sarma, P. Mahadevan, T. Saha-Dasgupta, S. Ray, and A. Kumar, Phys. Rev. Lett. **85**, 2549 (2000).

[376] O. Erten, O. N. Meetei, A. Mukherjee, M. Randeria, N. Trivedi, and P. Woodward, Phys. Rev. Lett. **107**, 257201 (2011).

[377] S. K. Pandey, A. K. Nandy, P. Kumari, and P. Mahadevan, Phys. Rev. B **105**, 214422 (2022).

[378] S. Di Matteo, G. Jackeli, and N. B. Perkins, Phys. Rev. B **67**, 184427 (2003).

[379] R. Ray, A. Himanshu, K. Brajesh, B. Choudhary, S. Bandyopadhyay, P. Sen, U. Kumar, and T. Sinha, in *AIP Conference Proceedings*, Vol. 1591 (American Institute of Physics, 2014) pp. 1155–1157.

[380] S. Chatterjee, J. Sau, S. Ghosh, S. Samanta, B. Ghosh, M. Kumar, and K. Mandal, Journal of Physics: Condensed Matter **35**, 035601 (2022).

[381] Supplemental Material: We here provide supplemental explanations and data on the following topics in relation to the main text: (I) Hopping Matrix (II) Orbital Degeneracy in Co atom (III) Ground state wave function with associated spin and charge densities (IV) Materials characterization and crystal structures (V)Methods (Vi)Matrix elements of spin-orbit coupling in crystal field (Vii) Characteristics of the nodal line (NL) in the presence and absence of spin-orbit coupling (SOC) (viii) Brief description of conductivity calculation.

[382] A. Mukherjee, N. D. Patel, S. Dong, S. Johnston, A. Moreo, and E. Dagotto, Phys. Rev. B **90**, 205133 (2014).

[383] A. Mukherjee, N. D. Patel, A. Moreo, and E. Dagotto, Phys. Rev. B **93**, 085144 (2016).

[384] G. Chang, S.-Y. Xu, H. Zheng, B. Singh, C.-H. Hsu, G. Bian, N. Alidoust, I. Belopolski, D. S. Sanchez, S. Zhang, *et al.*, Scientific reports **6**, 38839 (2016).

[385] G. L. Stamokostas and G. A. Fiete, Physical Review B **97**, 085150 (2018).

[386] I. Žutić, J. Fabian, and S. Das Sarma, Rev. Mod. Phys. **76**, 323 (2004).

[387] R. A. de Groot, F. M. Mueller, P. G. v. Engen, and K. H. J. Buschow, Phys. Rev. Lett. **50**, 2024 (1983).

[388] S. Wolf, D. Awschalom, R. Buhrman, J. Daughton, v. S. von Molnár, M. Roukes, A. Y. Chtchelkanova, and D. Treger, science **294**, 1488 (2001).